Beam profile measurements using the straw tracking detectors at the Fermilab muon $g-2$ experiment, and a study of their sensitivity to a muon electric dipole moment

Thesis submitted in accordance with the requirements of
the University of Liverpool for the degree of Doctor in Philosophy
by

Saskia Charity

September 2018

Abstract

The Fermilab muon $g-2$ experiment aims to measure the anomalous magnetic dipole moment of the muon, a_μ, to a precision of 140 ppb. The current value of a_μ was measured at the Brookhaven $g-2$ experiment, whose final result was published in 2006 with an uncertainty of 0.54 ppm [1]. The deviated from the Standard Model (SM) prediction by up to 3.6 σ, causing international intrigue that motivated the repetition of the experiment with increased statistics. The experiment's storage ring (SR) magnet was transported to Fermilab in 2013 to make use of its high-intensity muon beam. This will facilitate a 21-fold increase in statistics that will contribute most of the improved precision in the a_μ measurement. In addition, improvements to the experimental hardware are intended to reduce the systematic uncertainty. A major improvement is a new straw tracking detector system, which will measure the beam profile continuously throughout the experiment, in order to mitigate sources of systematic error associated with the beam position and motion. The straw trackers will also be used to perform a muon electric dipole moment (EDM) search. The current world's best limit on the muon EDM was placed by the Brookhaven $g-2$ experiment [2]. The signal for a muon EDM in the $g-2$ experiment can be directly measured with the straw tracking detectors, so the upgraded tracking system is expected to enable a reduction in the current limit by a factor of 100.

This thesis will describe the design and construction of the straw tracking detectors that took place at the University of Liverpool. The development and optimisation of a track extrapolation algorithm for propagating the track parameters of the decay positrons back to the muon decay position will be presented. The use of this algorithm in measuring the beam profile during the commissioning phase of the experiment will be discussed, and finally, the development of a muon EDM simulation and a preliminary sensitivity study using the track extrapolation algorithm will be presented.

Dedication & Acknowledgements

This thesis is dedicated to my fantastic, supportive and hilarious supervisor, Dr. Barry King. Shortly after I passed my viva, Barry tragically passed away suddenly on January 3rd 2019. Barry was the best supervisor I could ever have wished for; his enthusiasm for the experiment inspired me from day one. Travelling to Fermilab with Barry and the rest of the UK group was always immense fun, and there are stories that I will be laughing about for years to come. As well as motivating me to work hard in order to maximise my enjoyment of Physics, Barry taught me the even more valuable lesson of enjoying life outside of work. His sheer joy and love for his family was always hugely evident and was a constant reminder to me to focus on the truly important things in life. At collaboration meetings, Barry was always the life and soul, and he helped me to make so many great friends at Fermilab that I knew I wanted to stay here for my post doc. Quite simply, my life now would not be what it is if Barry had not been my supervisor, and I am grateful every day for the direction in which he led me. Here's to you, Barry – thanks for everything.

There are a number of people I wish to thank without whom the work presented in this thesis would have been impossible. Firstly, my supervisors Barry King, Themis Bowcock and, in the beginning, Steve Maxfield for giving me the opportunity to work on this fascinating experiment and guiding me along the way. Immeasurable thanks to Joe Price, who taught me everything from c++ to how to swing a 9-iron. This thesis would not be what it is without Joe, and neither would my knowledge of snooker rules (even though I don't recall asking to be taught that). Thanks also to everyone else in the Liverpool team for all the fun we had while building the detectors, including but not limited to: Will Turner, Dave Sim, Kayleigh Thompson, Mike Wormald, Mark Whiteley, John Carroll, Alex Keshavarzi, Tabitha Halewood-Leagas and Talal Albahri. I'll never forget the clean room days, so thanks to all of you for making it so enjoyable.

As well as my Liverpool friends, huge thanks go to the rest of the tracker team, including but not limited to: James Mott, Mark Lancaster, Becky Chislett, Tom Stuttard, Brendan Casey, Nick Kinnaird, Lee Roberts, Rob Carey, Tammy Walton, Gleb Lukicov, Nam Tran, Mike Eads, Farrukh Azfar and many others who helped along the way. I learnt so much from all of you and will be forever grateful for how much fun we had making these detectors work.

There are a huge number of friends I met at Fermilab who I must thank for making this experience so enjoyable that I chose to stay for a few more years. Thanks to Rachel Osofsky, Matthias Smith and Erik Swanson for being great friends when I first stayed at Fermilab without my British colleagues for a few weeks. Thanks to Mandy Rominsky, Brendan Kiburg, Jarek Kaspar, Karie Badgley, Midhat Farooq, Joe Grange, Antoine Chapelain, Leah Welty-Rieger, Renee Fatemi, Sudeshna Ganguly, Meghna Bhattacharya, Jason Crnkovic, Hogan Nguyen, Chris Polly, David Flay, Aaron Fienberg, Laura Kelton, Jason Hempstead, Nathan Froemming, Adam Lyon, David Sweigart, Marco Incagli and many more $g-2$ colleagues for the friendship, help and advice you have all offered me during my time at Fermilab. I am excited to continue working with you all. Thanks also to Jason Bono and Dan Ambrose from mu2e for their huge help with setting up the leak tests.

My friends and family in the UK have supported me so much throughout this journey that I cannot begin to express the thanks to all of them for putting up at various stages of this. My middle-B friends – Rachel, Ali, Louis, James, Beth, Kat, Laura and Henry – have been there for me since I started my degree in York in 2010 and you are all the greatest. Thank you for everything. Thanks to the Lavy girls, Kate, Byard, Maddie and Caz for never failing to make me laugh when I come back to the Shire.

Thanks to my amazing Mum for always making me believe I could do anything. Thanks to my wonderful Dad for helping me realise that 'anything' meant Physics. Thanks to my brother Danny for being my best friend and being there for me through everything. Thanks to Nanny and Granny, who I miss so much and I know would love to read this. I think of you every day. Thanks to Andy, Jenny, Robbie and Grainne, and everyone in my family for all the help and support; I couldn't have got here without any of you. Thank you.

To the various teachers I have had who started me on this journey – thank you. In particular, Mr Ford who first made me realise I could do Maths and Mr Bunney for being such a great A-level teacher that I decided to study Physics at university. To my lecturers at York who helped me enjoy Physics enough to want to do a Ph.D. – especially Martin Smalley and Mike Bentley – thanks.

Finally, honourable mentions to Quigley's for showing the Premier League and the jukebox in Peanuts for its continued service throughout my time living in Naperville.

Contents

Chapter 1

Introduction

Precision measurements of subatomic particles have long been used to test the Standard Model of Particle Physics (SM). Early measurements of the electron magnetic moment [3] were crucial to the development of Quantum Electrodynamics (QED), and since that measurement, the drive to measure the magnetic moments of other particles has continued. The concept of making high-precision measurements and comparing them to SM predictions is an appealingly simple one; making predictions and testing them with experiments is perhaps the most basic scientific principle.

Since the discovery of the muon in 1936 [4, 5], efforts to understand its properties have been a major focus of the Physics community. Although we are familiar with it now, the idea that there could be a second generation of electron that differed only in mass ($m_\mu = 207\ m_e$) was initially baffling to the community. The question of whether or not the muon really was just a 'heavy electron' sparked attempts to understand the processes that could explain its increased mass, and study how this affected its behaviour. It turned out that the answer might lie in their respective magnetic moments; specifically, in their *anomalous* magnetic moments, where 'anomalous' refers to any terms that cause the value to deviate from the expectation of g≡2 from Dirac theory.

Today, the measurement of the electron's anomalous magnetic moment agrees with the SM prediction at the ppt level, and is the most precise test of the SM ever performed [6]. Measuring the anomalous magnetic moments of the heavier leptons allows different parts of the SM to be tested in a similar way, since the lightweight electron is only really sensitive to QED interactions. It was first suggested by Schwinger [7] that the muon's anomalous magnetic moment would contain a term that the electron's did not due to its larger mass. The first muon magnetic moment experiments were intended as tests of QED; today, the measurements are so precise that they are used to search for evidence of interactions not accounted for by the SM. We now know that the sensitivity to beyond the SM (BSM) contributions to the lepton magnetic moments scales as $m_\ell^2,\ \ell = (e, \mu, \tau)$. It is almost impossible to make such precision measurements of the very heavy τ leptons due to their very short lifetime (2.9×10^{-13} s). The muon is the perfect compromise; it is heavy enough to be sensitive to a much wider range of interactions than the electron, but its

relatively long lifetime (2.2 μs) makes it possible to 'store' relativistic muons in a magnetic field for long enough to study its behaviour in detail.

The prediction [8] and subsequent observation [9] of parity violation in weak decays heralded the possibility of designing an experiment to measure the anomalous magnetic moment of the unstable muon. Parity violation enables the production of a polarised beam of muons (with their spins aligned with their momenta), and furthermore, enables the polarization of the muons to be probed directly via the emission angle of the decay electrons [10]. These two principles have underpinned all $g-2$ experiments since the first experiment at CERN in 1965 [11], including the Fermilab experiment that is the focus of this thesis. An in-depth discussion of these principles is presented in chapter 3.

The first CERN $g-2$ experiment was also the first to search for an electric dipole moment (EDM) of the muon. EDMs of fundamental particles, such as muons, exist only at energy scales far beyond the sensitivity of current experiments. Furthermore, Purcell and Ramsey [12] showed that the existence of a permanent EDM of a fundamental particle would violate CP-symmetry. However, the SM is known to be significantly deficient in sources of CP-violation, since it cannot account for the observed abundance of matter over antimatter in the universe, so searches for observations of CP-violating processes in nature remain of great interest. Like the CERN-I experiment, $g-2$ experiments since have been used to place limits on a muon EDM, with the current world's best limit being that placed by the Brookhaven $g-2$ experiment [2], and the new experiment at Fermilab aiming to reduce this limit by a factor of 100 [13].

The CERN-I experiment obtained the first ever measurement of the muon's anomalous magnetic moment, with an accuracy of ±2% that was eventually improved to ±0.4% [10]. At this level, the measurement was in full agreement with the current theory, implying (surprisingly) that the muon was exactly like a heavy electron. However, after several measurements of other properties of the muon in the following years, measuring the muon's anomalous magnetic moment appeared the best way to test QED and new, more accurate experimental techniques were required [14]. This led to the invention by Farley of the magnetic storage ring (SR) technique that has been used by $g-2$ experiments ever since – including the current experiment at Fermilab. A detailed explanation of the technique is presented in chapter 3.

After the CERN-II and CERN-III experiments, it was evident from advances in the theory community that electroweak contributions to the muon anomalous magnetic moment were the only known experimentally accessible quantities involving Z and W bosons. This motivated an experiment to improve the precision on the muon anomalous magnetic moment even further. A 400-fold increase in statistics on the CERN-II result was required, so the decision was made to do the experiment at Brookhaven National Laboratory (BNL) to make use of the available intensity from its Alternative Gradient Synchotron (AGS). There were several changes to the experimental design, the most notable of which was the development of a single magnet to provide a 1.45 T magnetic field uniform to 1ppm averaged around the entire azimuth. This was the largest and most precise superconducting magnet in the world.

The BNL experiment published its final result in 2006, achieving a precision of 0.54 ppm [1]. This remains one of the most precise measurements made in the field. The result caused an international storm, becoming the second-most cited result in the history of particle physics; it deviated from the current theoretical prediction by a factor of $3.3 - 3.6\sigma$ (depending on the particular theoretical treatment used). The result prompted a large number of theoretical proposals for the possible extensions to the SM that could cause such a discrepancy, and motivated the effort to reduce the uncertainty both on the experimental value and also the theoretical prediction. Today, the theoretical community has already improved its treatment of the difficult hadronic part of the calculation substantially, and further improvement is expected soon. The discrepancy shows no sign of going away based on this effort; in fact, some new theoretical predictions have seen the size of the discrepancy increase up to 4.1σ, and in no model is the value less than 3σ. Details of the SM prediction are presented in chapter 2.

The improvements on the experimental side are anticipated to come largely from an increase in statistics; the superconducting magnetic SR was transported from Brookhaven to Fermilab in order to repeat the experiment with the higher intensity and purity muon beam from the Fermilab accelerator complex. The aim is a four-fold reduction in the uncertainty, with equal systematic and statistical errors amounting to a total uncertainty of 0.14 ppm. Should the experimental value remain the same as the mean value recorded at BNL, the $> 3\sigma$ discrepancy could be as large as 7σ, becoming the first ever experimental observation of a non-SM process above the 5σ discovery level.

A number of improvements have been made to the experiment in order to reduce the systematic error as well as the statistical. The detector systems are either brand new or have been significantly upgraded. One brand new system is a suite of three straw tracking detectors, which will measure the trajectories of the decay positrons from the circulating muons in order to reconstruct the beam profile as a function of time throughout the experiment. These measurements will be used to quantify time-dependent properties of the beam that can affect the measurement of the muon anomalous magnetic moment, in order to improve the accuracy of the measurement. The tracking detectors are also the reason why the expected sensitivity to a muon EDM is so much greater than the previous experiment. The presence of a non-zero muon EDM affects the emission angles of the decay e^+ in a time-dependent way that can be directly measured by the tracking detectors. Such a sensitive direct analysis was not possible in the BNL experiment.

The Fermilab $g-2$ experiment took its first data with all systems installed during a commissioning run in May-July 2017. Only one station of tracking detectors was installed at this time, and the purpose of the run was to test the performance of all systems working together. The beam was largely contaminated by protons from the upstream accelerator, but the trackers were able to monitor the beam profile in order to provide real-time feedback to the teams responsible for beam injection and storage, and proved a useful tool during this commissioning phase. The first official Physics run began in November 2017, but the first few months of this time were spent tuning the beam injection and storage. The trackers were crucial during this phase. Now, the experiment is running at close to its target rate, and a dataset approximately the size of the Brookhaven dataset has been collected. This run will continue until the scheduled accelerator shutdown in July 2018. A longer run will begin again in October 2018, and will continue until the required amount of data to reach the target precision – 21 times more data than the BNL experiment – has been taken.

The construction, testing and operation of the straw tracking detectors forms the first part of the work presented in this thesis. The mechanical parts of the straw trackers were built at the University of Liverpool, with electronics provided by teams at UCL and Boston University. The author was heavily involved in many aspects of building and testing the detectors. The detectors are located in vacuum to reduce multiple scattering of the tracks passing through them; as such it was important to ensure the detectors, whose straws have a wall thickness of just 15 µm, and

are known to be permeable to certain gases, would conform to the strict vacuum requirement of the experiment. The author commissioned a straw leak testing procedure to be performed on all straws used in the detectors to ensure that these requirements were met.

Another major contribution to the experiment presented in this thesis is the development of the Runge-Kutta extrapolation software, which is used to propagate the parameters of the fitted tracks back to the muon decay position (and also forwards to the calorimeters). There are several unique challenges for the track extrapolation in this experiment: the detectors are in a varying magnetic field region, there is no fixed interaction point as a target for the extrapolation and there are a number of materials from which tracks can scatter, disrupting their trajectories. The author developed a robust algorithm that deals with all of these complications, and implemented it into the main experimental software. It is currently being used as an online data quality monitoring tool to give feedback to the beam tuning teams about the real-time beam position and motion. The development of the algorithm is presented in chapter 7, and measurements of the beam during the commissioning stages of the experiment are presented in chapter 8.

Another significant contribution was made to the Monte-Carlo (MC) simulation aspect of the experiment. The author added the capability to simulate a muon EDM of any size into the official experimental simulation. This has been used to generate events with large EDM values in order to test the sensitivity of the tracking detectors to a muon EDM signal. The track extrapolation is crucial to search for this signal, and has been used to extrapolate tracks from MC datasets with large EDM values, in order to test the sensitivity of the direct analysis method to a muon EDM.

Chapter 2

Theory of lepton dipole moments

2.1 Magnetic and Electric Dipole Moments

A charged particle in an external magnetic field will experience a torque, causing it to circulate about the direction of the field. The macroscopic understanding of this behaviour is familiar in everyday life; the magnetic field of the Earth exerts a torque on the needle of a compass, causing it to align with the field direction in order to minimise potential energy.

The quantum mechanical understanding of charged particles allows them to be considered just like the compass needle when treated as a statistical ensemble [15]. Fermions such as muons have an intrinsic angular momentum, or spin, meaning they also have an intrinsic magnetic moment, μ. On average, the magnetic moments of a large collection of quantum mechanical particles behave just like the needle of a compass. Their average spin directions will align with the direction of any external magnetic field, in order to minimise potential energy:

$$\mathcal{H} = -\boldsymbol{\mu} \cdot \boldsymbol{B} \, . \tag{2.1}$$

The compass needle in our macroscopic example will only remain aligned with the magnetic field if it is free from the influence of other external forces that could induce motion. If the needle in the field is caused to spin about its axis, it will *precess* about the magnetic field direction just like a spinning top or classical gyroscope. Since our quantum mechanical fermions have an intrinsic angular momentum, their magnetic moments (on average) will precess about the external magnetic field in exactly the same way. Both classically and quantum mechanically, the torque that gives rise to this behaviour is given by:

$$\boldsymbol{\tau} = -\boldsymbol{\mu} \times \boldsymbol{B} \, . \tag{2.2}$$

It is conceivable that the same behaviour might occur between the particle and an external electric field, and indeed there is room for such an interaction in Dirac theory. The full Hamiltonian describing the interaction of the particle's dipole moments and external magnetic and electric

	P	T	CP
$\boldsymbol{\mu}$	✗	✓	✓
$\boldsymbol{d}$	✗	✓	✓
$\boldsymbol{B}$	✗	✓	✓
$\boldsymbol{E}$	✓	✗	✗
$\boldsymbol{\mu} \cdot \boldsymbol{B}$	✗	✓	✓
$\boldsymbol{d} \cdot \boldsymbol{E}$	✓	✗	✗

Table 1: The transformation properties of the magnetic and electric dipole moments, and their respective terms in the interaction Hamiltonian in equation 2.3.

fields $\boldsymbol{B}$ and $\boldsymbol{E}$ is given by:

$$\mathcal{H} = -\boldsymbol{\mu} \cdot \boldsymbol{B} - \boldsymbol{d} \cdot \boldsymbol{E} \,, \tag{2.3}$$

where $\boldsymbol{\mu}$ and $\boldsymbol{d}$ define the magnetic and electric dipole moments of the particle respectively. The relationship between the magnetic dipole moment and the spin, $\boldsymbol{s}$, of the particle is dependent on its mass, m, its charge, q, and a dimensionless parameterisation constant called g - the gyromagnetic ratio:

$$\boldsymbol{\mu} = g\frac{q}{2m}\boldsymbol{s} \,, \tag{2.4}$$

where q is in units of the electron charge. It is clear from this expression that $\boldsymbol{\mu}$ is always aligned with the spin vector $\boldsymbol{s}$, since this is the only quantity in the expression that carries any directional information.

The particle's electric dipole moment also depends on a dimensionless constant, η:

$$\boldsymbol{d} = \eta\frac{e\hbar}{4mc}\boldsymbol{s} \,. \tag{2.5}$$

Consideration of the transformation properties of $\boldsymbol{d}$ and $\boldsymbol{\mu}$ highlight clear differences between the two moments. Both $\boldsymbol{\mu}$ and $\boldsymbol{d}$ change sign under time reversal (T) transformations, since they are both proportional to the spin vector $\boldsymbol{s}$ which is an axial vector. The magnetic field $\boldsymbol{B}$ is also an axial vector and so changes sign under T as well. However, the electric field $\boldsymbol{E}$ is a polar vector and does not change sign under T. Considering the interaction Hamiltonian in equation 2.3, T is conserved by the term $\boldsymbol{\mu} \cdot \boldsymbol{B}$, but violated by the term $\boldsymbol{d} \cdot \boldsymbol{E}$. If CPT is considered an invariant symmetry, then violation of time-reversal symmetry implies violation of CP symmetry. This means that $\boldsymbol{d} = 0$ under all CP-conserving theories. The transformation properties are summarised in table 1.

The only observations of CP-violating interactions to date have been in the quark sector, with the first observation in the $K_2^0 \rightarrow \pi^+\pi^-$ channel in 1964 [16], and several more recent observations in B decays [17]. EDMs of charged leptons only enter the SM at the multi-loop level, orders of magnitude beyond the reach of current experiments; as such, any observation of a non-zero EDM in a charged lepton would be a direct sign of a BSM interaction. Sources of CP violation are keenly sought since this is the only plausible explanation for the observed baryon asymmetry in the universe. A further motivation to study the muon EDM specifically is that this is the only current search for an EDM of a second-generation particle. This is particularly interesting since some speculative BSM models that account for large fundamental EDMs (described later in this chapter) postulate a dependence on particle generation [18–20].

2.2 History of spin and the gyromagnetic ratio

Since the discovery of spin by Compton [21], and independently Uhlenbeck and Goldschmidt [22], in 1925, the understanding of its behaviour in different contexts has been an enormous focus of effort throughout the scientific community. Crucial to this quest have been attempts to quantify g for different particles, and to make predictions of its size that agree with experimental observation.

Shortly after the concept of spin was introduced, Dirac predicted that the value of g should be exactly 2 for spin-$\frac{1}{2}$ particles like electrons, muons and protons [23]. This prediction accounted for the observations made in the Stern-Gerlach [24] and Phipps-Taylor [25] experiments, and for a few years the case was considered closed; $g = 2$ for fermions. However, in 1933 Frisch, Stern and Estermann measured $g_{\text{proton}} = 5.5$ [26, 27]. Even more surprising were the measurements by Stern and Estermann, and Rabi *et. al.*, the following year of a non-zero magnetic moment of the neutron [28, 29]. The neutron had been assumed not to have a magnetic moment since it has no charge. These measurements were the first experimental evidence that the nucleons were not fundamental particles; with the benefit of hindsight we now understand that the net magnetic moments of baryons are due to their internal substructure of quarks and gluons [15].

The Dirac prediction that $g_e = 2$ for electrons agreed (within experimental uncertainty) with contemporary measurements, until Kusch and Foley measured a (0.119 ± 0.0005 %) discrepancy in 1947 [3]. In the same year, measurements of the hyperfine structure of hydrogen [30–32]

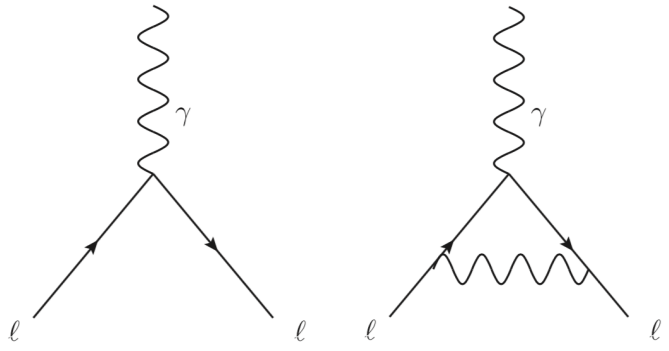

(a) **(b)**

Figure 1: Diagrams of the (a) tree-level (Dirac) and (b) one-loop (Schwinger) contributions to g.

also showed signs of disagreement with Dirac theory. In 1948, Schwinger utilised the rapidly developing understanding of Quantum Electrodynamics (QED) to suggest that a small radiative correction to the lowest-order Dirac moment might give rise to a 'small additional electron spin magnetic moment' that would account for these discrepancies [33]. The presence of a correction to the gyromagnetic ratio makes it convenient to express g in terms of a 'Dirac' term and an 'anomalous' term:

$$\mu = \big(1 + a\big)\frac{q\hbar}{2m} \qquad \text{where} \qquad a = \frac{g-2}{2}\,. \tag{2.6}$$

The quantity a is referred to as the anomalous magnetic moment, or simply 'the anomaly', and will be used in the following discussion instead of g. The Feynman diagram of Schwinger's radiative correction is shown in figure 1, and illustrates the interaction of the lepton with a short-lived virtual loop photon. Schwinger calculated the value of this purely QED radiative correction to be $a = \frac{\alpha}{2\pi} \approx 0.00116$, where α is the fine-structure constant. This was in excellent agreement with Kusch and Foley's measurement of a_e, and was one of the first ever precision tests of QED. The correction is the same for all leptons.

Since Schwinger's pioneering calculation of the LO correction to a_ℓ, the understanding of virtual-loop interactions and vacuum polarization effects has advanced significantly. In the SM, leptons are understood to undergo myriad virtual interactions that can perturb their magnetic dipole moments and hence alter the value of g. The variety of virtual particles and interactions to which measurements of a_ℓ are sensitive makes them excellent targets for precision tests of the SM. It is also possible that BSM virtual-loop interactions could occur. Comparison between precision

measurements of a_ℓ and the SM predictions could hence highlight discrepancies from the SM indicative of the existence of BSM processes, or else place limits on particular speculative BSM models.

Conventionally, the contributions to a_ℓ^{SM} from the wide range of possible virtual-loop interactions are separated into three different categories:

$$a_\ell = a_\ell^{\mathrm{QED}} + a_\ell^{\mathrm{had}} + a_\ell^{\mathrm{EW}} \ . \tag{2.7}$$

a_ℓ^{QED} includes the Schwinger term and contains QED contributions from virtual leptons and photons only. a_ℓ^{had} describes all interactions with hadrons, including the hadronic vacuum polarization corrections to the Schwinger term as well as hadronic light-by-light contributions. Finally, any virtual-loop contributions from the W, Z and Higgs bosons comprise the electroweak term, a_ℓ^{EW}. Some terms, such as the Schwinger term, are identical for all three charged leptons; others are heavily mass-dependent and the significance of their contributions is different for each lepton. This means that the muon's anomalous magnetic moment is slightly larger than that of the electron, and the tau's even larger than the muon's. The heavier leptons are much more sensitive to higher-order terms than the electron.

To perform a precision test of the SM, it is desirable to have equal experimental and theoretical uncertainties. The measurement of g_e by Hanneke *et. al.* [6] to a precision of 0.28 ppt is the most stringent test of the SM ever performed. However, the uncertainty on the SM prediction of g_e is approximately 20 times larger than the experimental uncertainty. g_e is sensitive to QED interactions only, and all QED terms depend at some level on the fine structure constant, α. α is not a theoretical quantity and must be determined experimentally. The measurement of g_e itself can be used to determine α - at present, the highest precision of α is determined in this way [6]. However, an independent measurement of α must be used for the prediction, and this limits the precision of g_e^{SM}. Future experiments [34] aim to reduce this uncertainty to enable an even more precise evaluation of g_e^{SM}.

The current precision on the experimental measurement of a_μ is 0.54 ppm, measured in the Brookhaven experiment [1]. While this is far less precise than the measurement of a_e, a_μ is sensitive to much higher mass scales than a_e. Since a_e is almost exclusively sensitive to QED terms,

a_μ can probe a much wider range of interactions and potential BSM models. It is also possible to achieve equal experimental and theoretical uncertainties for a_μ since the precision is not limited by the precision on α, as is the case for a_e. The Fermilab $g-2$ experiment aims for experimental uncertainty of $\delta a_\mu^{\text{exp}} = 0.14\text{ppm}$; it is hoped that with advancements in calculating some of the less straightforwardly tractable elements of the SM prediction, δa_μ^{SM} will be comparably reduced on a similar timescale. The current status of the SM prediction, a_μ^{SM}, is presented in the following section.

2.3 The Standard Model prediction of a_μ

A summary of the different contributions to the SM prediction of a_μ is illustrated in figure 5. The QED contribution dominates the value at over 99%, but is known to the highest precision. The uncertainty on the prediction, δa_μ^{SM}, is dominated by the uncertainty on a_μ^{had}. In this section, the component parts of the prediction will be discussed in turn.

2.3.1 QED contributions to a_μ^{SM}

All of the QED interactions contributing to a_μ^{SM} are radiative correction interactions, of which the Schwinger term in figure 1 is an example. The QED terms comprise all interactions that are due to leptons and photons alone. The Schwinger term is referred to as a first-order term in α, and the successive terms can be calculated perturbatively by expanding a power series in $\frac{\alpha}{2\pi}$:

$$a^{\text{QED}} = \sum_n^\infty A_n \left(\frac{\alpha}{\pi}\right)^n a^{(2n)} \,, \tag{2.8}$$

where the first order term is the Schwinger term, which dominates the value of a_ℓ^{QED} in all cases.

In an extraordinary effort by Kinoshita *et.al.* [35, 36], terms of up to fifth-order in α have been calculated. The diagrams include interactions involving the emission and reabsorption of one or more photons (radiative correction terms, such as the Schwinger term), and diagrams involving the pair production and subsequent annihilation of an off-shell photon ('vacuum polarization' terms). Each interaction type is depicted in figure 2. Over 12,000 Feynman diagrams, containing up to 5 loops, were computed in order to obtain the following value for a_μ^{QED}:

$$a_\mu^{\text{QED}} = (11658471.8971 \pm 0.007) \times 10^{-10} \,. \tag{2.9}$$

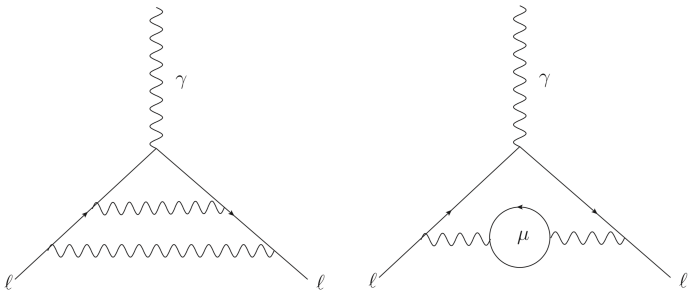

(a) **(b)**

Figure 2: Examples of Feynman diagrams contributing to a_μ^{QED}. Figure (a) is a Schwinger-like radiative correction term, and (b) is an example of a vacuum polarization term, where the off-shell photon undergoes pair production to form some lepton and another photon, which is reabsorbed.

The precision on this value is far below both the precision of the Brookhaven measurement and the expected precision on a_μ^{exp} from the Fermilab experiment. Although the prediction of a_μ^{QED} relies heavily on the use of numerical integration techniques to compute the 5-loop calculations, the work of Kinoshita $et.al.$ has been corroborated by independent analyses [37–42], and a_μ^{QED} is safely considered to be well-understood, and does not contribute significantly to $\delta a_\mu^{\mathrm{SM}}$.

2.3.2 Electroweak contributions to a_μ^{SM}

The EW terms contribute the smallest fraction to the value of a_μ^{SM}; the large mass of the W and Z bosons leads to the suppression of these terms. Feynman diagrams describing the leading EW processes are shown in figure 3. The first diagram represents the LO EW interaction. It is identical to the Schwinger term, except the photon has been substituted for a Z or Higgs boson. The second diagram illustrates the largest contribution to a_μ^{EW}. It involves the conversion of the muon to an appropriately charged W boson, with the emission and subsequent recapture of a muon neutrino. The contribution is well understood, having been calculated to the two-loop level [43], and the uncertainty is negligible compared to that of the hadronic contributions. The value used in the total prediction for a_μ^{SM} is:

$$a_\mu^{\mathrm{EW}} = (153.6 \pm 1.0) \times 10^{-11} \ . \tag{2.10}$$

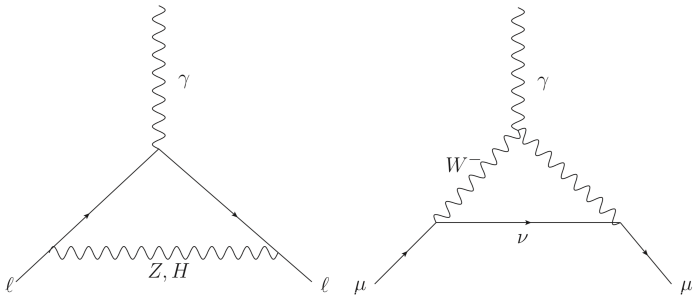

Figure 3: Feynman diagrams illustrating (a) the LO (b) the largest terms in a_μ^{EW}.

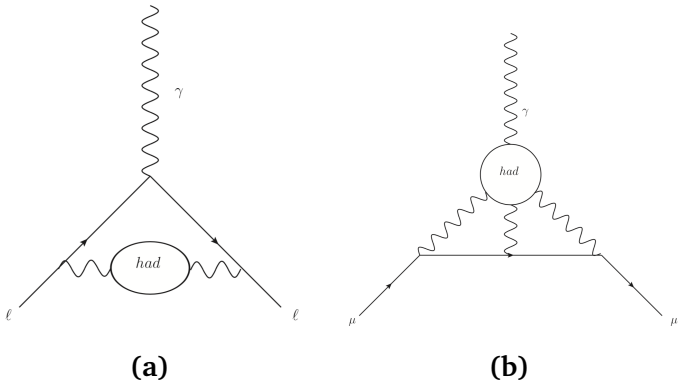

Figure 4: Feynman diagrams illustrating (a) the LO HVP interaction and (b) the LO HLbL interaction.

2.3.3 Hadronic contributions to a_μ^{SM}

The collection of terms involving a particle sensitive to quantum chromodynamics (QCD) interactions, such as quarks, is referred to as a_μ^{had}. While contributing less than 1% of the value of a_μ^{SM}, the hadronic contribution term completely dominates the uncertainty. Unlike the QED and electroweak contributions, a_μ^{had} cannot be calculated perturbatively at the energy scales relevant to the dominant terms. The hadronic contribution can be broken into two parts: a hadronic vacuum polarisation (HVP) term and a hadronic light-by-light (HLbL) term:

$$a_\mu^{\mathrm{had}} = a_\mu^{\mathrm{HVP}} + a_\mu^{\mathrm{HLbL}} \,. \tag{2.11}$$

Each of these interactions will now be described in turn.

Hadronic vacuum polarization (HVP) contributions

The simplest (LO) HVP diagram is shown in figure 4a. The interaction is similar to the leptonic vacuum polarisation interaction described previously, but the pair-production in the internal photon line involves hadronic, rather than leptonic, matter. HVP terms have the largest contribution to the value of a_μ^{SM} after QED terms, and traditionally have the largest contribution to the uncertainty of a_μ^{SM}.

Calculation of a_μ^{had} relies on data-driven methods; specifically, a *dispersion relation* is used to obtain a_μ^{had} from the experimentally measured cross-section of the process $e^+\,e^- \rightarrow hadrons$. Data from a range of experiments including KLOE, BaBar, BELLE, VEPP and BES is used to obtain the cross-sections for all LO and NLO final states [44]. Recently, the NNLO contribution has also been measured [45]. The greatest contribution to both the value and the uncertainty of a_μ^{HVP} comes from the cross-section of the $\pi^+\pi^-$ channel; recent measurements from the KLOE [46] and BESIII [47] collaborations have enabled significant improvement in the evaluation of this particular contribution to a_μ^{HVP}.

The reduction of the uncertainty on the hadronic cross-section has been the focus of several recent major works, including the KNT18 [44], DHMZ17 [48] and FJ17 [49] analyses. The KNT18 and DHMZ17 approaches use the same experimental datasets but exploit markedly different data combination techniques, leading to different parts of the data being given a stronger weighting in each analysis. While slight tensions exist between the calculations for the individual channels, the overall predictions are in very good agreement. The FJ17 analysis produces a value consistent with KNT18 and DHMZ17 within the uncertainties, but a channel-by-channel comparison is not possible here. The values from the different analysis groups are given in equation 2.12:

$$\begin{aligned} a_\mu^{\mathrm{HVP,\ KNT18}} &= (693.3 \pm 2.5) \times 10^{-10}\ , \\ a_\mu^{\mathrm{HVP,\ DHMZ17}} &= (693.1 \pm 3.4) \times 10^{-10}\ , \\ a_\mu^{\mathrm{HVP,\ FJ17}} &= (688.1 \pm 4.1) \times 10^{-10}\ . \end{aligned} \tag{2.12}$$

For an in-depth discussion of the differences between the data combination techniques used in the different cross-section analyses, see [44].

While the dispersive treatment of a_μ^{HVP} will continue to improve with increasing availability

of experimental data, novel ways to calculate the HVP terms are sought. Independent, competitive evaluations can provide a valuable cross-check of the dispersive approach, potentially arbitrating between conflicting dispersive predictions, and may increase the precision of the prediction. Calculations based on lattice QCD are rapidly improving, and a recent prediction using this method [50] is in good agreement with the dispersive predictions. Another entirely different method to measure the LO term in a_μ^{had} experimentally, using muon-electron elastic scattering, has recently been proposed [51].

Hadronic Light-by-Light (HLbL) contributions

The Feynman diagram for the simplest hadronic light-by-light process is shown in figure 4b. The basic mechanism involves the interaction of the propagating muon with three photons. These photons interact with some hadronic matter which in turn interacts with a photon in the external field. This HO interaction type enters a_μ^{SM} at third-order in α. Like the HVP terms, HLbL terms cannot be calculated perturbatively, and the calculation is complicated further still since data-driven methods cannot be employed in this case. As such they have a large relative uncertainty compared to the size of the value. The HLbL terms contribute a smaller amount of the value of a_μ^{had} than the HVP terms - around 2% - but a large fraction of the uncertainty. In previous analyses, the uncertainty has accounted for approximately 40% of $\delta a_\mu^{\text{had}}$. However, with the significant gains in the precision of a_μ^{HVP} discussed in the previous section, the uncertainty contributions are now comparable with – or in the case of KNT18, greater than – those from HVP terms. This motivates efforts to increase the precision of the a_μ^{HLbL} calculation.

The currently accepted value for a_μ^{HLbL} was agreed upon by an international collaboration of theorists and is referred to as the 'Glasgow consensus' [52]. The traditional method for the calculation relies on model-dependent approaches, but several alternative approaches have been attempted, which differ slightly in their treatment of sub-leading effects [44]. The original Glasgow consensus value for a_μ^{HLbL}, in [52], has been adjusted since its publication after it was noticed [53] that the contribution from axial exchanges had been overestimated due to an inaccurate assumption about the symmetry of their form factors. An in-depth discussion of this adjustment is presented in [44] and [53]. The value used to obtain the values for a_μ^{SM} in figure 6 is taken from [54]:

$$a_\mu^{\text{HLbL}} = (9.8 \pm 2.6) \times 10^{-10} \ . \tag{2.13}$$

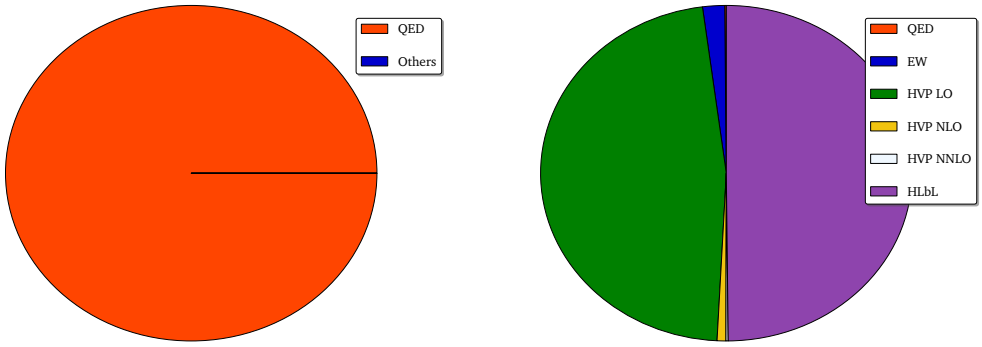

(a) **(b)**

Figure 5: Pie charts illustrating the size of the contribution of the various components to $a_\mu^{\rm SM}$ and $\delta a_\mu^{\rm SM}$. Contributions from QED terms [36], EW terms [43], LO, NLO [44] and NNLO [45] HVP terms, and HLbL terms [54] are shown.

2.3.4 The discrepancy between $a_\mu^{\rm SM}$ and $a_\mu^{\rm exp}$

The theoretical predictions for the different contributions can be combined to obtain an overall prediction for the value and uncertainty of $a_\mu^{\rm SM}$. Using the KNT18 prediction for $a_\mu^{\rm HVP}$, the following prediction for $a_\mu^{\rm SM}$ is obtained:

$$\begin{aligned} a_\mu^{\rm SM} &= a_\mu^{\rm QED} + a_\mu^{\rm EW} + a_\mu^{\rm HVP} + a_\mu^{\rm HLbL} \\ &= (11658471.8971 \pm 0.007) + (15.36 \pm 0.1) + (693.3 \pm 2.5) + (9.8 \pm 2.6) \times 10^{-10} \\ &= 11659182.05 \pm 3.56 \times 10^{-10} \ . \end{aligned} \tag{2.14}$$

This prediction has a precision of 0.3 ppm. The target precision of the Fermilab $g-2$ experiment is 0.14 ppm. The new techniques used to compute the $a_\mu^{\rm HVP}$ term have resulted in a much improved precision on this part of the prediction. However, there is an ongoing international effort ('The Muon $g-2$ Theory Initiative') to improve the overall prediction even further to bring $\delta a_\mu^{\rm SM}$ in line with the anticipated experimental precision. New experimental data, as well as the improvements on the lattice calculation, is expected to improve the dispersively calculated HVP calculation. For the first time, a value of $a_\mu^{\rm HVP}$ with an uncertainty less than that of $a_\mu^{\rm HLbL}$ has been obtained by the KNT18 analysis group [44]. HLbL also has the largest relative error bar to the size of the value of

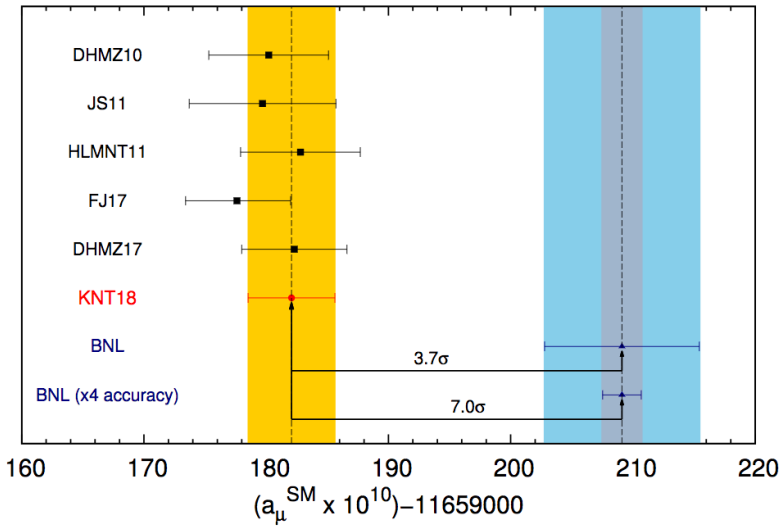

Figure 6: The most recent values for a_μ^{SM} compared to the value of a_μ^{exp} from the BNL experiment with both the uncertainty from the BNL experiment as well as the anticipated four-fold reduction in the uncertainty from the Fermilab experiment. [44]

all the contributions. As such, efforts to improve this part of the prediction are quickly becoming a priority. Efforts are ongoing to compute the contribution in novel ways; a very recent paper [55] presents the first attempt to calculate a_μ^{HLbL} dispersively. It is hoped that with this effort, δa_μ^{HLbL} can be reduced significantly.

The discrepancy $a_\mu^{\text{exp}} - a_\mu^{\text{SM}}$ from the different analysis groups is shown in figure 6. The values differ slightly where different values for the hadronic parts of the calculation have been used. Nonetheless, there is no treatment in which the discrepancy is less than 3σ, and there is no sign of the discrepancy going away based on theoretical efforts alone.

2.4 Lepton dipole moments and New Physics

2.4.1 New Physics and the a_μ discrepancy

The deviation between a_μ^{SM} and a_μ^{exp} is greater than 3σ in every theoretical treatment, and is as large as 4.1σ in one particular model. While further reduction in the experimental uncertainty is required to confirm or eliminate the discrepancy at the 5σ level, there has been much discussion in the theoretical community about the possible New Physics (NP) models that could account for such a discrepancy since it first appeared.

The BSM sensitivity of a_ℓ is related to the energy scale of NP, Λ, in the following way:

$$\delta a_\ell^{\mathrm{NP}} \propto \left(\frac{\alpha}{\pi}^{\mathrm{NP}}\right) \times \left(\frac{m_\ell}{\Lambda}\right)^2 \times C^{\mathrm{NP}}\,, \tag{2.15}$$

where m_ℓ is the lepton mass and $C^{\mathrm{NP}} = \delta m_\ell^{NP}/m_\ell$ is a model-dependent mass-suppression term that paramaterises the NP contributions. The term arises due to the requirement for lepton chirality flips at this scale. The muon is approximately 205 times heavier than the electron, and so using the above relationship, is around 43000 times more sensitive to BSM contributions than the electron. In general, Λ is assumed to be at or less than the TeV scale for a_μ [56].

One appealing possibility for a BSM contribution that could account for the size of the a_μ discrepancy is the virtual-loop interaction of the muon with supersymmetric (SUSY) particles. Specifically, a_μ^{NP} could contain smuon-neutralino and sneutrino-chargino loops [56], and potentially slepton mixing. The leading effect is thought to come from models with a large value of $\tan\beta$ [1] ($\sim 40°$), and in general, the smaller SUSY masses will have a greater contribution to a_μ^{NP}. For a discrepancy of $\Delta a_\mu = 25 \times 10^{-10}$, the most likely mass scale for a SUSY effect of this size is $\Lambda \sim 500$ GeV/c^2. For a detailed discussion of the SUSY contributions to a_μ^{NP}, see [56] and [57].

Another possible way that NP could affect a_μ is via radiative corrections to the muon mass m_μ. The lepton masses are often thought to be 'unnaturally' light compared to the masses of the lightest bosons [56]. Some models have been proposed in which the 'bare' mass of the muon is 0, and all of its mass comes from radiative interactions with as yet undiscovered virtual particles. In such a model, the constant $C^{\mathrm{NP}} = \mathcal{O}1$.

There exist several other possible exotic explanations for Δa_μ. Effects in the EW sector, such as the existence of a W' or Z' boson or the anomalous behaviour of the W boson like an anomalous magnetic moment or electric quadrupole, have been proposed [56]. Alternative Higgs models have been proposed [58, 59], as well as phenomena in the dark sector such as dark photons [60] or even a dark boson [61, 62]. Much of the phase-space probed by such models has been ruled out by measurements at other experiments, for example at BaBar [63]. However, there is still a significant region of mass-space that cannot be explored by the LHC experiments. In any case, the

[1] $\tan\beta$ is the ratio of the vacuum expectation values, v_1 and v_2, for the supersymmetric and SM Higgs doublets.

number of potential explanations for the a_μ discrepancy makes it a fascinating candidate for the 'harbinger of New Physics' [56].

2.4.2 New Physics and the muon EDM

It was introduced previously in this section that the existence of a non-zero muon EDM, d_μ, is highly suppressed in the SM, since the EDM of a fundamental particle entails a CP-violating phase orders of magnitude beyond that expected in the SM. Several BSM extensions accommodate a large d_μ however, and some notable examples will now be discussed.

Any BSM extension that includes a large d_μ must predict that the size of d_μ is mass-independent. There are several such scenarios, the most likely of which is the Higgs doublet scenario [18, 19]. The two-Higgs doublet model (THDM) contains two Higgs doublets, resulting in five physical Higgs bosons after spontaneous symmetry breaking. It provides two sources of CP-violation generated by the mixing of the different bosons. Lepton EDMs are generated in this model via two-loop diagrams containing a top quark, a gauge boson and a charged Higgs boson; the CP-violation enters in the interaction with the charged Higgs boson. The size of d_e and d_μ scale with tanβ, the ratio of the lighest neutral Higgs bosons in the model, rather than the lepton mass. Figure 7 shows that for large tan β, d_μ can approach $\mathcal{O}10^{-23}$ $e \cdot$ cm. This is just two orders of magnitude beyond the currently anticipated limit on d_μ from the Fermilab $g-2$ experiment.

Another BSM model that can accommodate a large d_μ include Randall-Sundrum extra dimensions scenarios [20], in which the proposed extra-dimensions interact with the different generations of leptons differently. This particular extension proposes magnitudes of d_μ as high as $\mathcal{O}10^{-20}$e $\cdot$ cm - just 1 order of magnitude beyond the current limit.

A key feature of both of these extensions is a scaling with lepton generation rather than lepton mass. This is particularly relevant, since searches for a muon EDM provide a unique opportunity to search for EDMs in a second generation particle.

2.5 Summary

The pursuit of precision measurements of the lepton dipole moments is strongly motivated by the theory behind them. The theoretical explanation for the size of the muon anomalous magnetic

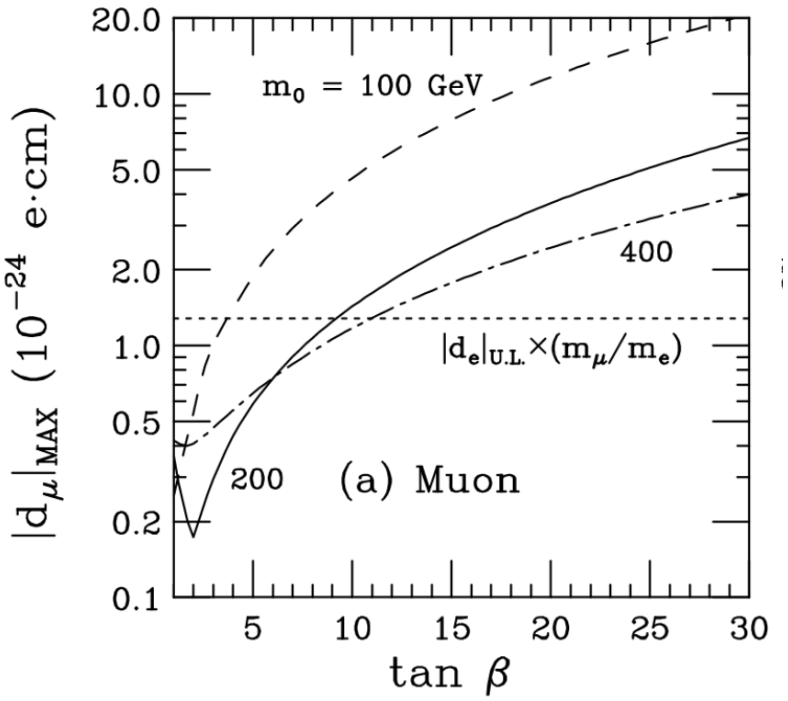

Figure 7: The maximal muon EDM allowed by unitarity in the THDM, from [18].

moment contains almost all of SM physics, with every known particle entering the prediction at some level. Comparison between the experimentally measured and theoretically predicted values of a_μ is an excellent way to test not just QED, but a huge range of other SM interactions including QCD and EW processes. The current tension between a_μ^{exp} and a_μ^{SM} is greater than 3σ in all theoretical treatments, and possible BSM explanations for the discrepancy have been presented in this section. The vast number of higher-order processes to which a_μ is sensitive makes it plausible, or at least possible, that some BSM process might also affect this quantity.

Conversely to a_μ, d_μ contains almost no SM physics at all, with the SM prediction for the CP-violating muon EDM lying many orders of magnitude beyond current experimental sensitivity. However, the amount of CP violation in the universe must be much greater than that accounted for in the SM, which motivates searches for BSM CP-violating interactions. By placing increasingly strict limits on CP-violating EDMs of fundamental particles, the possible physical explanations for them become more tightly contrained, and we can begin to eliminate BSM models that include large EDM values.

The following two chapters of this thesis will present a detailed explanation of the physical principles behind the measurement of a_μ in the Fermilab $g-2$ experiment. An explanation of the features of the experiment that are expected to enable a reduction of two orders of magnitude in the current world's best limit on d_μ will also be presented.

Chapter 3

The Physics of the $g-2$ experiment

Before describing the procedure and hardware of the $g-2$ experiment, this chapter will provide a detailed explanation of the physical principles that underpin the experiment. Techniques that will enhance the statistical sensitivity to a_μ will be presented.

3.1 Overview

The Fermilab experiment aims for an overall improvement of a factor of 4 in the precision on a_μ^{exp} compared to the BNL measurement, which had a total error of ±540 ppb. This was heavily dominated by the statistical error; the new experiment uses Fermilab's muon beam with the aim to achieve a factor of 21 increase in statistics. This is the leading contribution to the improvement in the overall precision. However, by improving control of the systematics there is an anticipated reduction in this contribution to the total error by a factor of 2.5 – 3. The target is to achieve equal statistical and systematic errors, resulting in a total experimental uncertainty of ± 140 ppb. If this goal is achieved, and the central value of a_μ is unchanged from the BNL value, then the 3.6σ discrepancy from the SM becomes greater than 5σ, and the world's first observation of BSM physics is made. In the case that the measured central value is consistent with the SM, then BSM models with contributions from a non-SM value of a_μ can be confidently eliminated.

The $g-2$ experiment uses the storage ring (SR) measurement technique that has been used to measure a_μ since its invention at CERN in 1963 [10]. The experimental hardware will be described in detail in chapter 4. In the experiment, a beam of polarized muons[2]. is injected into a toroidal magnet with a vertically aligned magnetic field, where the muons circulate – or are 'stored' – until they decay to positrons. The basic principle of the measurement relies on the fact that the spin vector of a fermion in an external magnetic field will precess about the field vector at a frequency proportional to g. The rate of the spin precession cannot be directly measured, since spin direction is not an observable quantity. The experiment is instead designed to measure the precession of the average direction of decay positrons emitted from the precessing muons. The

[2]The $g-2$ experiment will use μ^+ rather than μ^-. The term muon will be used throughout this thesis to refer to muons and antimuons interchangeably, unless otherwise indicated.

rate of this precession is directly correlated with the rate of the muon spin precession itself. The reasons for this correlation will be explained in the following sections.

This chapter will also describe some of the major sources of systematic error on the a_μ measurement. The systematics which can be characterized using measurements of the straw tracking detector system will be explained in particular detail, since an analysis of the capability of the tracking detectors to provide information about the beam that can reduce these sources of uncertainty form is presented in chapter 8.

In addition to improving the precision of the a_μ measurement, the Fermilab experiment also aims to place a reduced limit on the magnitude of the muon's electric dipole moment (EDM). The experimental design enables an EDM search to be performed without disruption to the primary goal of measuring a_μ. The current upper limit on muon EDM magnitude was placed by the Brookhaven experiment [2]:

$$|d_\mu| < 1.9 \times 10^{-19} e \cdot \text{cm} \, . \tag{3.16}$$

The Fermilab experiment aims to reduce this limit by two orders of magnitude, via a combination of increased statistics and the introduction of upgraded features to enable significant reduction in the major systematics on the BNL limit. The final part of this chapter will introduce the analysis techniques that can be used to search for an EDM, and explain the reasons for the expected increase in sensitivity.

3.2 Principles of the $g-2$ measurement

3.2.1 Larmor precession

The magnetic dipole moment (MDM) of a fermion is related to its spin by the equation:

$$\boldsymbol{\mu} = g\frac{q}{2m}\boldsymbol{s} \, , \tag{3.17}$$

where q is the charge of the fermion in units of the electron charge, m is the mass of the particle and g is the gyromagnetic ratio. A particle with a non-zero magnetic moment in the presence of a magnetic field will experience a torque, causing its spin axis to precess about the magnetic field vector in a process known as Larmor precession. For non-relativistic particles, the rate of this

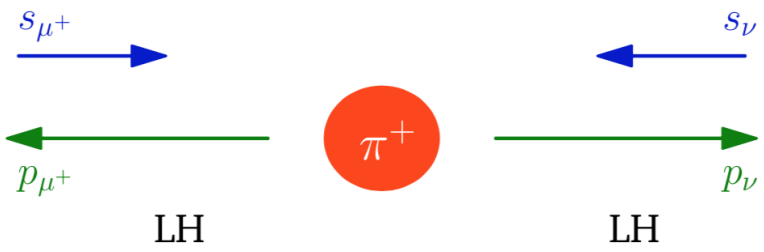

Figure 8: Schematic diagram of the parity violating pion decay.

precession is given by the Larmor or 'spin' frequency:

$$\boldsymbol{\omega}_s = g\frac{e\boldsymbol{B}}{2m}\,, \tag{3.18}$$

where all symbols have their previously stated definitions. The direction of the spin vector is not an observable quantity, so g cannot be determined from an experimental measurement of $\boldsymbol{\omega}_s$. There is, however, a measurable quantity from which $\boldsymbol{\omega}_s$ can be extracted; the precession of the average direction of the decay e^+ emitted from the precessing μ^+. The reasons for this are explained in the following sections, and the experimental method for measuring the average e^+ decay angle oscillation is described.

3.2.2 Pion decay

The μ^+ for the g-2 experiment are created from a beam of pions generated according the procedure detailed in sect 4.1. μ^+ are produced in the weak pion decay:

$$\pi^+ \rightarrow \mu^+ + \nu_\mu\,. \tag{3.19}$$

The parity-violating nature of the weak decay [8, 64] means this process can be exploited to produce a beam of polarized muons, with their spins perpendicular to the vertically aligned magnetic field. This is necessary in order to observe the spin precession that is required to determine a_μ.

In the SM, ν_μ are emitted with antiparallel spin and momentum vectors; this is a 'left-handed'

(LH) helicity configuration. The opposite is true for $\bar{\nu}_\mu$, which are right-handed (RH) and have parallel spin and momentum vectors. Pions are spin-0, meaning that the μ^+ produced in the decay must also have LH helicity in order to conserve angular momentum. This feature of the decay enables the production of a polarized muon beam from the pion beam. Figure 8 illustrates the pion decay and the helicity constraints. In the center-of-mass frame of the π^+, the μ^+ is emitted with antiparallel spin and momentum vectors; in the lab frame, this corresponds to a correlation between the spin and momentum directions of the μ^+. A highly polarised beam of μ^+ can be obtained by selecting only the highest momentum μ^+, with antiparallel spin and momentum vectors. Such decays are termed 'backwards' decays since the μ^+ are emitted in the opposite direction of the ν_μ in the pion rest frame. In the case of π^-, the highest momentum μ^- are the forwards decays with parallel spin and momentum vectors.

3.2.3 Muon decay

The dominant decay of the μ^+ is via the following process:

$$\mu^+ \rightarrow e^+ + \nu_e + \bar{\nu}_\mu \ . \tag{3.20}$$

This is also a weak interaction, and the parity-violating nature of the process can be exploited once again. The decay is referred to as a 'self-analyzing' process, since the spin states of the decay positrons can almost always be determined from their emission angles. The (effectively) massless ν_e and $\bar{\nu}_\mu$ are solely produced with LH and RH helicity, respectively. In addition to these helicity constraints, the spin of the μ^+ must be conserved in this decay. Conservation of momentum arguments constrain the highest energy positrons to come from decays where the ν_e and $\bar{\nu}_\mu$ are emitted at 180° to the e^+. This configuration also satisfies the helicity and spin arguments, since it can be seen in figure 9 that in this scenario the spins of the ν_e and $\bar{\nu}_\mu$ cancel, meaning that the spin of the e^+ is always parallel to the spin of the μ^+. Thus the highest energy positrons exhibit the highest correlation between their spin and momentum vectors. Since the direction of the e^+ spin vector can be determined directly from its emission direction, the precession of the average direction of the highest energy e^+– a measurable quantity – can be used to probe the muon spin precession, $\boldsymbol{\omega}_s$.

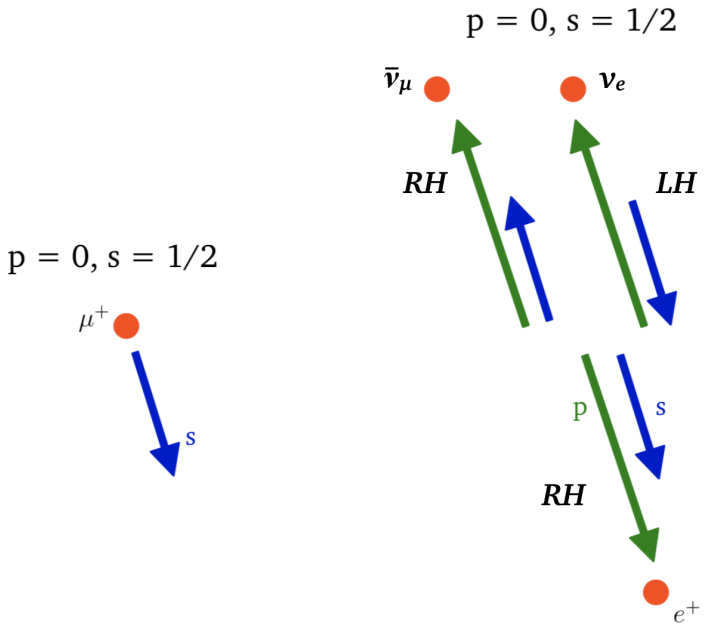

Figure 9: Schematic diagram of the parity violating muon decay

3.2.4 Cyclotron motion

A charged particle moving in an external magnetic field will undergo cyclotron motion; such is the case for the muons in the $g-2$ storage ring. The $g-2$ magnetic field is a constant, vertically aligned field, and so the e^+ follow a path of constant radius with angular cyclotron frequency $\boldsymbol{\omega_c}$. In the non-relativistic case, this frequency is given by:

$$\boldsymbol{\omega_c} = \frac{\boldsymbol{eB}}{\boldsymbol{m}} \,. \tag{3.21}$$

The momentum vector of a muon in the storage ring will precess about the vertically aligned magnetic field with frequency ω_c, in addition to the precession of its spin vector, ω_s. The difference between these two frequencies, $\boldsymbol{\omega_a} = \boldsymbol{\omega_s}$- $\boldsymbol{\omega_c}$, is referred to as the anomaly precession frequency and is given by:

$$\boldsymbol{\omega_a} = \boldsymbol{\omega_s} - \boldsymbol{\omega_c} = \left(\frac{g}{2} - 1\right)\frac{\boldsymbol{eB}}{\boldsymbol{m}} = a_\mu \frac{\boldsymbol{eB}}{\boldsymbol{m}} \,. \tag{3.22}$$

Conveniently, this expression depends directly on a_μ (rather than g_μ), which means that a_μ can

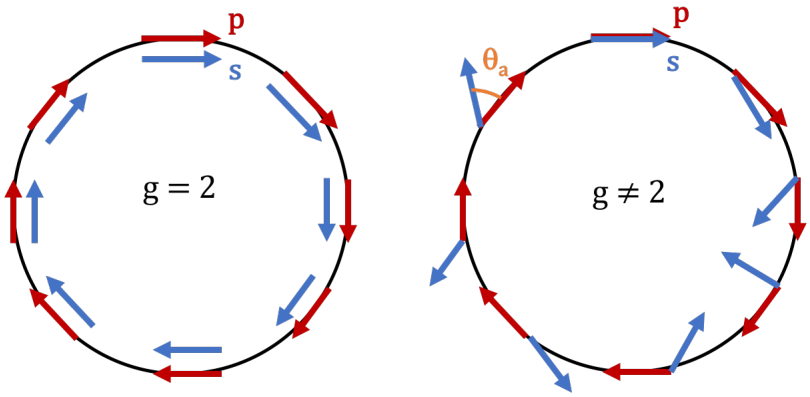

Figure 10: Cartoon illustrating the anomalous precession in the SR. Were $g = 2$, the muon spin vector $\boldsymbol{s}$ (blue) would remain aligned with the muon momentum vector $\boldsymbol{p}$ (red) as it orbited the SR. Since $g \neq 2$, the spin vector precesses about the momentum vector. The angle θ, known as the anomaly angle, varies with frequency $\boldsymbol{\omega}_a$.

be extracted directly from the measurement of a signal that varies with the frequency ω_a. The only other unknown in this expression is the magnetic field, B, which must be known to the same precision as ω_a to obtain the required precision on the a_μ measurement.

3.2.5 Extracting a_μ from the ω_a measurement

From equation 3.22, it is clear that even if $\boldsymbol{\omega}_a$ and $\mathbf{B}$ were known to the required precision, the overall precision would still be limited by the precision of the measurement of the muon mass. When expressed in kg, the muon mass has an uncertainty of 51 ppb [65]. It is possible to express a_μ in terms of two ratios that are known more precisely than the muon mass:

$$a_\mu = \frac{\mu_p}{\mu_e}\frac{m_\mu}{m_e}\frac{g_e}{2}\frac{\omega_a}{\tilde{\omega}_p} \,. \tag{3.23}$$

The ratio μ_p/μ_e, or the electron-proton magnetic moment ratio, is known to a precision of 8.1 ppb [65], while the muon-electron mass ratio, $\frac{m_\mu}{m_e}$ is 25 ppb [65]. The measurement of the electron g-factor, g_e, is the most precise measurement of an SM quantity ever made, with an uncertainty of 0.28 ppt [6]. Expressing a_μ in terms of these precisely-known ratios and the ratio between ω_a and ω_p, the free-proton precession frequency, provides an easier way for the experiment to achieve its target uncertainty on a_μ of 140 ppb. The $g-2$ experiment has an extensive suite of NMR probes and calibration systems to measure ω_p when induced by exactly the same external magnetic field as ω_a, ensuring correlation between the two frequencies.

Expression 3.23 can be further simplified using the relation $m_\mu/m_e = (g_\mu\mu_\mu)/(g_e/\mu_e)$:

$$a_\mu = \frac{\mathcal{R}}{\lambda^+ - \mathcal{R}} \ . \tag{3.24}$$

where $\mathcal{R} = \omega_a/\omega_p$ and $\lambda^+ = \mu_{\mu^+}/\mu_p$, which was determined in the LAMPF muonium hyperfine structure experiment [66] and is equal to:

$$\frac{\mu_\mu}{\mu_p} = 3.183345118(89) \ . \tag{3.25}$$

The $g-2$ experiment is designed to measure ω_a and ω_p to equal precision. In the following sections, the principles behind the ω_a measurement are explained in detail; the measurement and calibration of ω_p, and the hardware for producing the uniform, vertical 1.45T magnetic field is described in chapter 4. The focus of the work presented in this thesis is on the straw tracking detector system, whose primary function is to monitor the stored muon beam as a function of time throughout the muon fill in order to reduce sources of systematic error on the ω_a measurement.

3.3 Measuring ω_a

In the laboratory frame, a relativistic decay positron is boosted in the direction of the μ^+ momentum. As explained above, the emission direction of the decay e^+ is highly correlated with the direction of the μ^+ spin vector, and this in turn is highly correlated with the average e^+ energy. The e^+ emitted in the direction of the muon momentum will have the maximal average energy, and e^+ emitted in the opposite direction to the μ^+ will have minimal average energy. The correlation between the e^+ emission angle and the μ^+ spin direction means that the average e^+ energy depends directly on the angle between the μ^+ spin and momentum vectors. This angle varies with the anomaly frequency ω_a and is therefore referred to as the anomaly angle. This is illustrated in figure 10. Since the anomaly angle depends strongly on μ^+ energy, the number of μ^+ above some energy threshold observed by a detector will vary with time with a frequency ω_a, with maxima when the μ^+ spin is aligned with its momentum and minima when the μ^+ spin is in the opposite direction to its momentum. This method of extracting ω_a by measuring the number of decay e^+ detected as a function of time has been the fundamental measurement principle of $g-2$ experiments since it was first used in the CERN-II experiment in 1968 [14].

3.3.1 Relativistic corrections to ω_a

The relativistic muons in the storage ring are subject to the effects of Thomas precession as well as Larmor precession. Thomas precession is the effect of the rotation of the particle rest frame relative to the observer frame, and adds a slight correction to the spin precession frequency $\boldsymbol{\omega}_s$:

$$\boldsymbol{\omega}_s = g\frac{e\boldsymbol{B}}{2m} + \left(1-\gamma\right)\frac{e\boldsymbol{B}}{\gamma m}\,, \tag{3.26}$$

where γ is the Lorentz factor. In addition, the cyclotron frequency $\boldsymbol{\omega}_c$ is altered by relativistic effects:

$$\boldsymbol{\omega}_c = \frac{e\boldsymbol{B}}{\gamma m}\,. \tag{3.27}$$

Thus in the relativistic case, $\boldsymbol{\omega}_a$ is expressed as:

$$\boldsymbol{\omega}_a = g\frac{e\boldsymbol{B}}{2m} + \left(1-\gamma\right)\frac{e\boldsymbol{B}}{\gamma m} - \frac{e\boldsymbol{B}}{\gamma m}\,, \tag{3.28}$$

which simplifies to:

$$\boldsymbol{\omega}_a = g\frac{e\boldsymbol{B}}{2m} - \frac{e\boldsymbol{B}}{m} = \left(\frac{g}{2}-1\right)\frac{e\boldsymbol{B}}{m}\,. \tag{3.29}$$

The relativistic effects are cancelled out, and the expression for the precession frequency in equation 3.22 is recovered.

3.3.2 Electric field contributions to ω_a

The storage ring magnetic field provides only radial focusing of the muon beam; vertical focusing is provided by a set of electrostatic quadrupoles, as will be explained in section 4.3. The presence of an electric field alters both $\boldsymbol{\omega}_s$ and $\boldsymbol{\omega}_c$ and hence alters $\boldsymbol{\omega}_a$:

$$\boldsymbol{\omega}_a = \frac{e}{m}\left[a_\mu \boldsymbol{B} - \left(a_\mu - \frac{1}{\gamma^2-1}\right)\frac{\boldsymbol{\beta}\times\boldsymbol{E}}{c}\right], \tag{3.30}$$

where β is the particle velocity as a fraction of the speed of light in vacuum, c. The electric field in the storage ring is non-uniform, and it would be very difficult to control its precision to the same level as the magnetic field. The dependence on the electric field $\boldsymbol{E}$ (and the Lorentz factor) would spell disaster for measuring ω_a to any appreciable level of precision, were it not possible to simplify the expression significantly using a convenient choice of γ which cancels out the $\boldsymbol{\beta} \times \boldsymbol{E}$ term. This value of γ is referred to as the 'magic' γ, γ_{magic}:

$$\gamma_{magic} = \sqrt{1 + \frac{1}{a_\mu}}\,, \tag{3.31}$$

When $\gamma = \gamma_{magic}$, the expression for $\boldsymbol{\omega}_a$ reduces to the form in equation 3.22. This solution was first proposed in the CERN III experiment [14], where the electrostatic vertical focusing was first used, and has been a key feature of all $g-2$ experiments since. The value of γ_{magic} is 29.3 which corresponds to the easily experimentally achievable 'magic' momentum value of $p_m = 3.094$ GeV/c, which is the target momentum for the μ^+ injected into the storage ring. However, the unavoidable spread in the momentum of the stored beam of $\sim 0.15\%$ means that many stored muons will not be at p_m exactly, and the electric field will hence affect their precession. For muons with $p \neq p_m$, the precession frequency is given by:

$$\omega_a' = \omega_a \left[1 - \beta \frac{E_r}{cB_y} \left(1 - \frac{1}{a_\mu \beta^2 \gamma^2} \right) \right], \tag{3.32}$$

where E_r is the radial component of the electric field, B_y is the vertical component of the SR magnetic field, and the other terms have their previously stated definitions.

Using $p = \beta\gamma m = (p_m + \Delta p)$, the expression for the fractional difference in ω_a can be obtained:

$$\frac{\Delta\omega_a}{\omega_a} = -2\frac{\beta E_r}{cB_y}\left(\frac{\Delta p}{p_m}\right). \tag{3.33}$$

The presence of the electric field reduces the measured frequency and alters the expression for ω_a given in 3.22. The fractional momentum deviation can be expressed in terms of the 'equilibrium radius' x_e, which is the equilibrium orbit radius of the circulating muon relative to the 'magic'

radius R_0 (the orbit radius of a muon with $p \equiv p_m$):

$$\frac{\Delta p}{p} = (1-n)\frac{x_e}{R_0} \ . \tag{3.34}$$

The quantity n is the field index, given in equation 4.59 in section 4.2 where the electrostatic quadrupole system is described. This equation can be rearranged to obtain the strength of the electric field. Using equations 4.59 and 3.34, the fractional correction to ω_a can be obtained:

$$\frac{\Delta\omega}{\omega} = -2n(1-n)\beta^2\frac{x x_e^2}{R_0^2} \ . \tag{3.35}$$

Here, x is the radial position of the muon relative to the R_0. Instantaneously, x may be any value between the maximum and minimum of the radial betatron oscillation amplitude. However, in a uniform magnetic field and quadrupole focusing field, x is equivalent to the equilibrium radius x_e when averaged over all times, so this expression becomes:

$$\frac{\Delta\omega}{\omega} = -2n(1-n)\beta^2\frac{\langle x_e^2\rangle}{R_0^2} \ . \tag{3.36}$$

$\langle x_e^2\rangle$ can be obtained either from the so-called 'fast rotation analysis'. Lower momentum muons with lower orbit radii will, after many cycles, eventually 'overtake' the higher-radius muons, which causes the bunched beam to spread out over time; this effect, known as de-bunching, is entirely dependent on the muon momentum distribution, and so analysis of this effect can be used to obtain $\langle x_e^2\rangle$. In the Brookhaven experiment, the electric field correction to ω_a was $+0.47 \pm 0.05$ ppm.

3.3.3 Maximising the statistical significance of the ω_a signal

It was introduced above that the method for determining ω_a in the $g-2$ experiment is to count the number of decay positrons observed above some energy threshold as a function of time. The oscillation of this number tells us ω_a directly since the positron energy is highly correlated with its emission angle; high energy positrons are more likely to be emitted in the forward direction, and low energy positrons are more likely to be emitted antiparallel to the muon momentum direction. Therefore, the number of positrons above some energy cut will oscillate with frequency ω_a. It is important to note that if positrons of *all* energies were counted, there would be no oscillation, and the only signal observed in the calorimeters would be the exponential decay curve corresponding

to the rate of decay of the muons in the storage ring. It follows from this that some energy cut can be found that maximises the $g-2$ signal. If the cut is too low, then the amplitude of the oscillation will be reduced; too high a cut will reduce the statistical sensitivity too drastically. In this section, the 'trade-off' between these two considerations is discussed, and the optimal cut for maximising the ω_a signal will be determined.

Under the assumption that the energy of the decay e^+ $E \gg m_e c^2$, the differential decay distribution in the muon rest frame (MRF) (for μ^+) is given by:

$$dP(y,\theta) \propto N(y)\left[1 + A(y)cos\theta\right]dyd\Omega \ , \tag{3.37}$$

where $y = p/p_{max}$ is the momentum fraction of the e^+, $d\Omega$ is the solid angle, and $\theta = \cos^{-1}\left(\hat{p}\cdot\hat{s}\right)$ is the angle between the muon spin and the positron momentum, p_{max}. The number distribution, $N(y)$, is given by:

$$N(y) = 2y^2(3-2y) \ , \tag{3.38}$$

and the decay asymmetry A is given by:

$$A(y) = \frac{2y-1}{3-2y} \ . \tag{3.39}$$

It can be seen in figure 11 that both the number distribution and the decay asymmetry are maximal at $y = 1$, and the asymmetry changes sign at $y = \frac{1}{2}$.

It follows from equation 3.37 that the decay e^+ will have a preferred direction in the MRF when weighted according to their decay asymmetry. In the laboratory frame, at p_m, the e^+ are emitted very nearly parallel to the μ^+ momentum regardless of their energy or direction in the MRF. Thus it would not be straighforward to place a cut on the e^+ decay angle as any deviation from parallel would be almost impossible to observe in a detector. It is only practical to cut on the measured energy of the e^+ in the laboratory frame. Selecting only e^+ of a certain energy in the laboratory frame will typically yield a subset of positrons with a net momentum (in the MRF) either par-

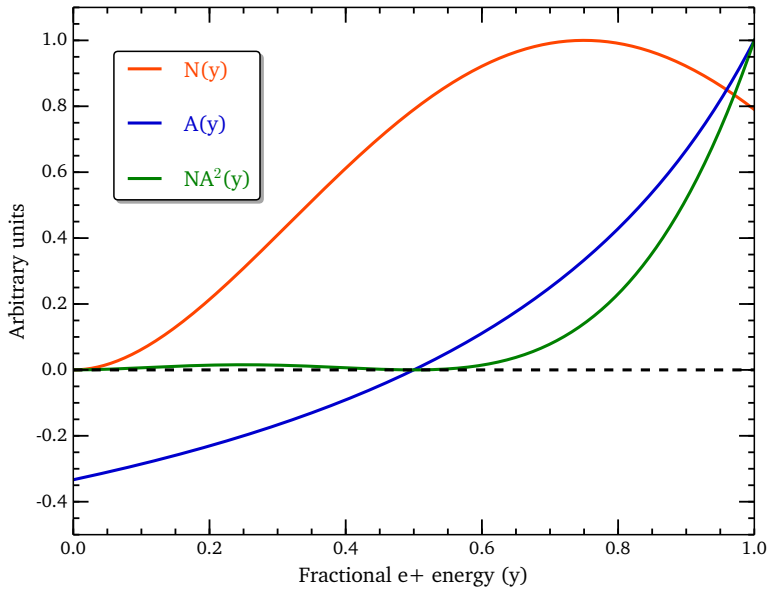

(a) Muon rest frame

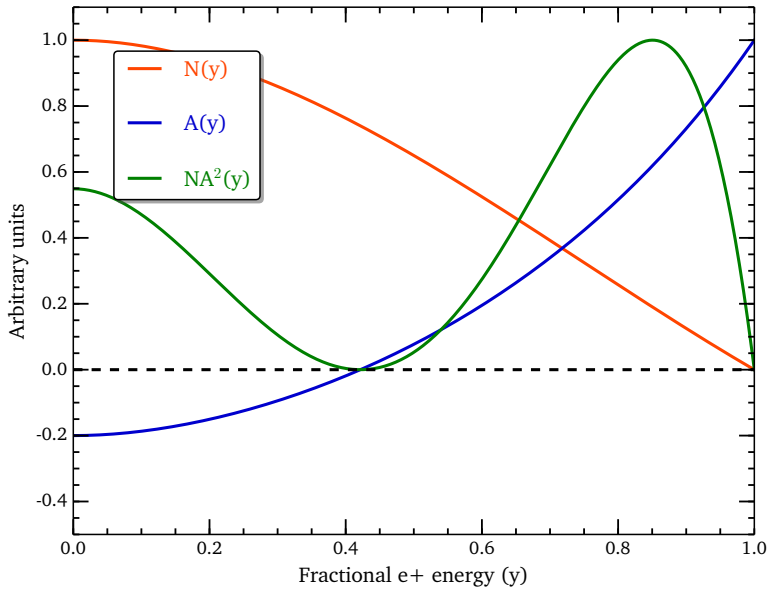

(b) Lab frame

Figure 11: Plots of the number distribution, N, the asymmetry function, A, and the statistical figure-of-merit NA^2 as a function of the fractional positron energy in (a) the MRF and (b) the lab frame. Each function is normalised to peak at 1.

allel or antiparallel to the muon momentum direction. For further discussion of this effect, see [15].

The energy dependence of the decay asymmetry is illustrated in figure 13. Figure 13a shows the effect of selecting only e^+ above a range of energy cuts, and figure 13b shows the effect of only selecting e^+ with energy less than the given cut. From the former plot, it is evident that selecting high-momentum e^+ only yields the greatest asymmetry, illustrating that the highest energy e^+ are more likely to be emitted in the direction of the muon spin. When high-energy events are removed, the tendency is towards e^+ of $E = 0$ being equally likely to be emitted either parallel or antiparallel to the muon spin, since as $E \longrightarrow 0$, the correlation between the positron momentum and the polarization direction weakens, and the only constraint on the emission direction is that the spin must be either parallel or anti-parallel.

Equations 3.37, 3.38 and 3.39 can be transformed into the laboratory frame to give the oscillation of the number of positrons with time as a function of their energy, from which the expressions for the measured number density and the asymmetry in the detector frame can be obtained:

$$N(y,t) = N_0(y)e^{-t/\gamma\tau}\left[1 + A(y)\cos\left(\omega_a t + \phi(y)\right)\right], \tag{3.40}$$

where

$$N(y) = \frac{1}{3}(y-1)(4y^2 - 5y - 5), \tag{3.41}$$

and

$$A(y) = \frac{1 + y - 8y^2}{4y^2 - 5y - 5}. \tag{3.42}$$

In both equations, $y = E/E_{max}$ is the fractional energy of the decay e^+ relative to the maximum energy of 3.1 GeV in the laboratory frame. The form of these functions is shown in figure 11b. The equations are modified when only positrons with energy greater than some energy cut are counted:

$$N_{th}(y) = \frac{1}{3}(y-1)^2(-y^2 + y + 3), \tag{3.43}$$

and

$$A(y) = \frac{y(2y+1)}{-y^2 + y + 3}. \tag{3.44}$$

The forms of these equations are shown in figure 12a. The distributions will be modified in reality

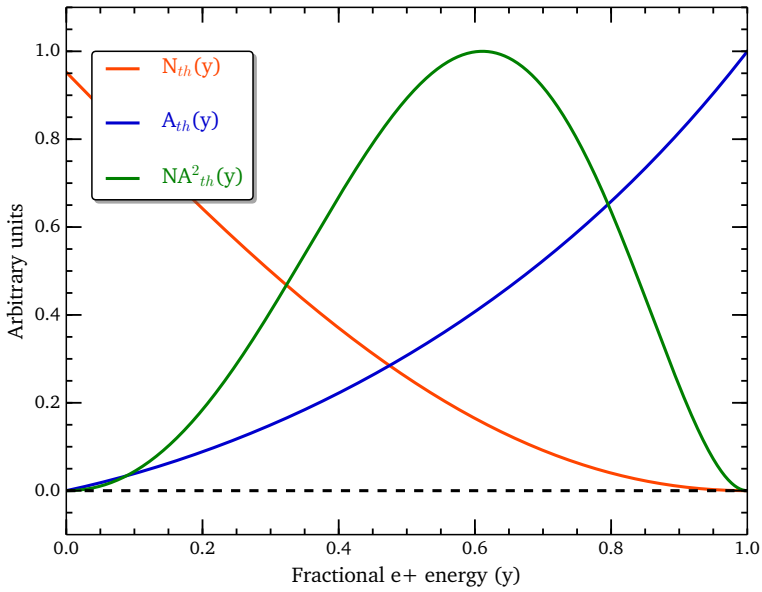

(a) Lab frame, no detector effects

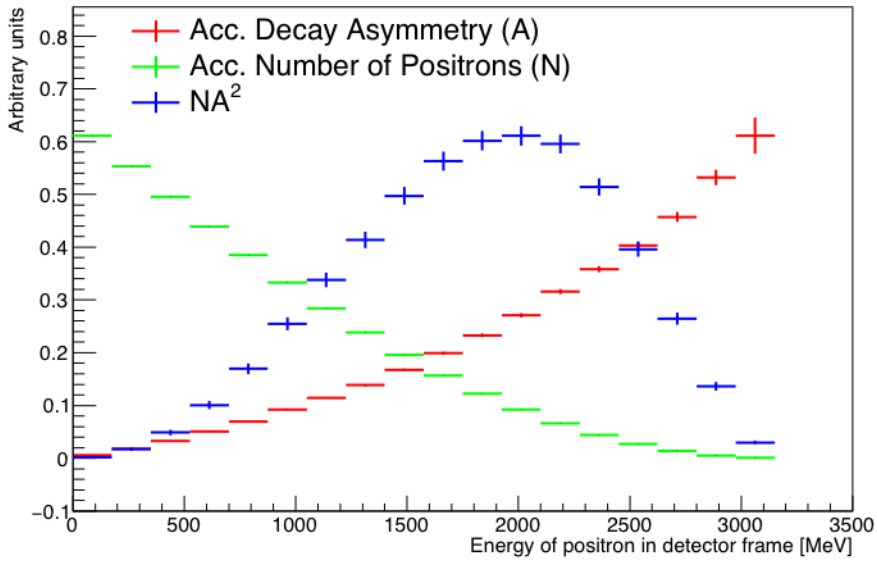

(b) Lab frame, with detector effects

Figure 12: The number distribution, N, the asymmetry function, A and the statistical figure-of-merit NA^2 as a function of the fractional energy of positrons above some energy threshold E_{th}. 12a shows the effect of selecting only positrons with $E > E_{th}$; the optimal value of NA^2 in this case is at around 0.6 E_{max} which corresponds to $\sim$ 1.8 GeV. Detector resolution and acceptance effects have not been considered. 12b is from simulation and includes detector effects; in this case,the optimal energy cut for maximising NA^2 is $\sim$1.9 GeV.

due to detector and resolution effects; these effects are included in the plots in figure 12.

The fractional statistical error on the precession frequency (obtained by fitting the five-parameter function for the total number of detected positrons in equation 3.40) is given by:

$$\delta\epsilon = \frac{\delta\omega_a}{\omega_a} = \frac{\sqrt{2}}{2\pi f_a \tau_\mu \sqrt{NA^2}}\,, \tag{3.45}$$

where f_a is the anomaly frequency, $\omega_a = 2\pi f_a$ and τ_μ is the muon lifetime.

If the magnetic field and muon momentum were fixed, then the quantity to maximise in order to minimise the statistical uncertainty of the measurement (the figure of merit) is NA^2. From figure 11b, it can be seen that in the detector frame, NA^2 would be maximised for positrons above $0.85E_{max}$, which corresponds to a detected positron energy of ~ 2.6 GeV. Considering only positrons above a certain energy cut, as in figure 12a, the optimal energy cut is actually $\sim 0.6E_{max} = 1.8$ GeV, which becomes closer to 1.9 GeV when detector effects are taken into account. A full explanation of these expressions is given in [15].

3.4 Muon EDM measurement

In addition to measuring $g-2$, a secondary Physics goal of the Fermilab $g-2$ experiment is to reduce the current limit on the magnitude of a muon electric dipole moment (EDM) by a further two orders of magnitude. The experiment is sensitive to a number of signals that would be introduced into the data by the presence of a non-zero muon EDM. These signals and their measurement techniques will now be discussed.

3.4.1 EDM measurement techniques

There are three main ways in which a muon EDM can be detected in the $g-2$ experiment:

- Increase in muon precession frequency.
- Direct detection of oscillation in the average vertical angle of the decay e^+.
- Measurement of a vertical asymmetry in the average arrival position of the decay e^+ at the detectors.

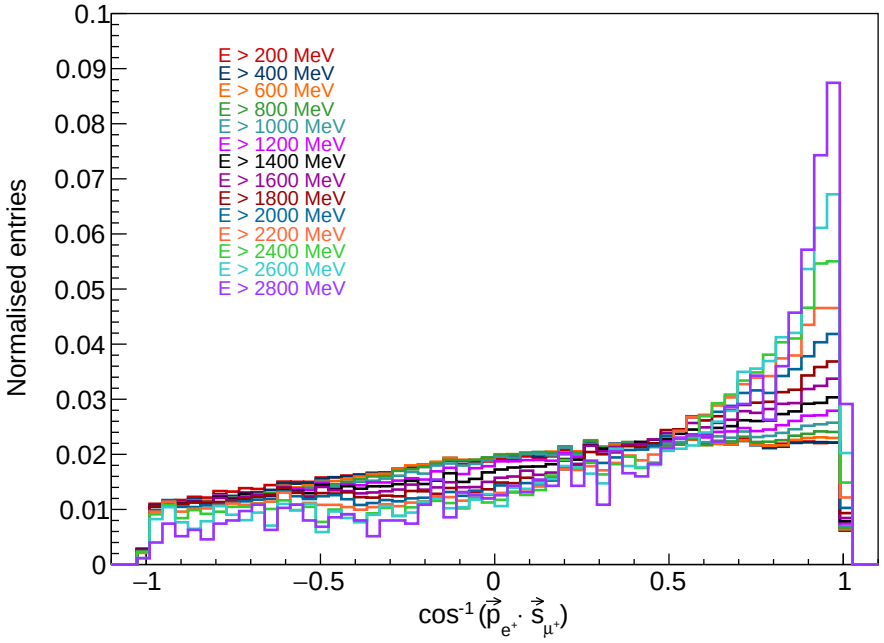

(a) Angle between e^+ momentum and and μ^+ polarisation vector, $p_{e^+} > p_{th}$

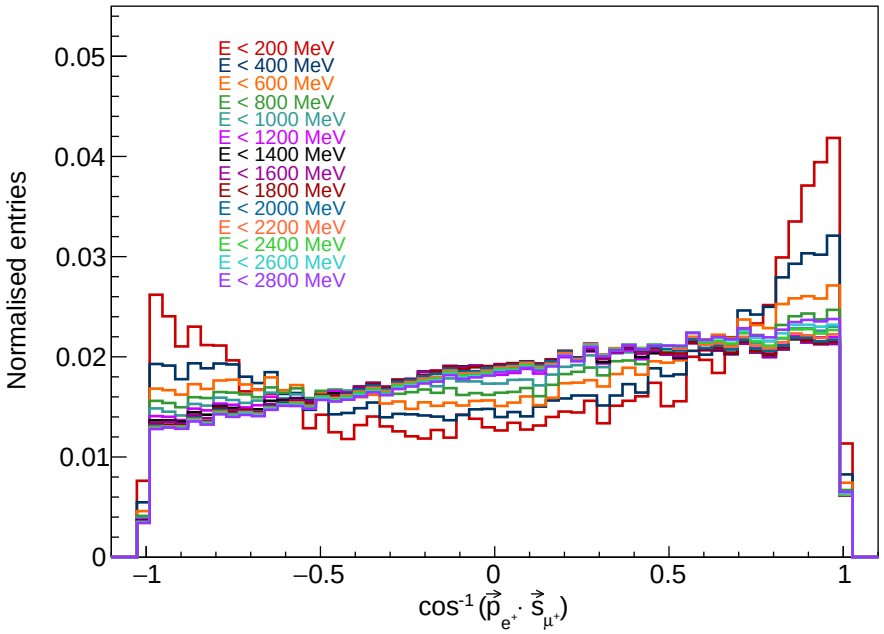

(b) Angle between e^+ momentum and and μ^+ polarisation vector, $p_{e^+} < p_{th}$

Figure 13: Plots of the number of positrons emitted as a function of the emission angle for different energy cuts. In both plots, the x axis is the angle between the positron momentum vector and the muon polarization vector in the MRF.

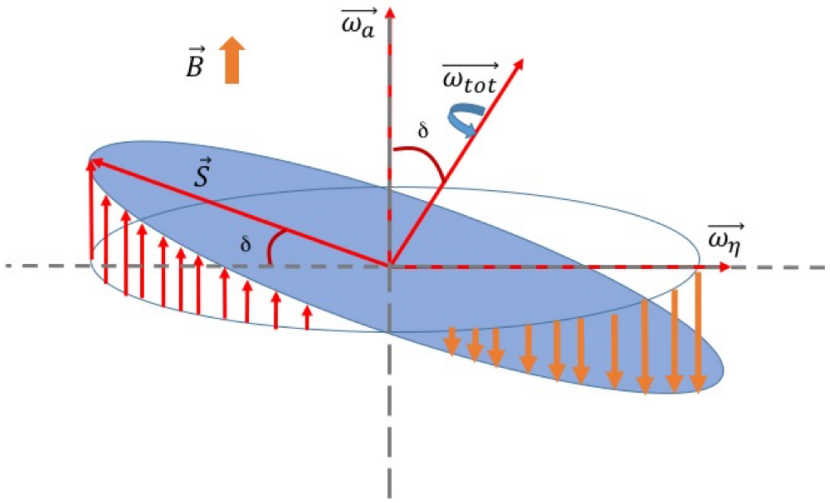

Figure 14: Diagram illustrating the effect of a muon EDM on the muon precession in the $g-2$ storage ring (SR). The EDM interacts with the motional electric field (the $\boldsymbol{\beta}\times$B term) to introduce an oscillation about the vector $\boldsymbol{\omega}_\eta$, which is perpendicular both to the direction of motion (out of the page) and the $g-2$ oscillation $\boldsymbol{\omega}_a$. The muon spin vector is illustrated by $\vec{S}$. The muon spin now precesses about the vector $\boldsymbol{\omega}_{a\eta}$, which is tilted away from the vertical by angle δ. The magnitude of δ increases linearly with increasing d_μ.

Increase in muon precession frequency due to vertical tilt

A muon with a non-zero EDM will experience a torque due to the interaction of its EDM with the motional electric field induced by the relativistic motion of the particle in the presence of a magnetic field (and with the electric quadrupole field). This additional torque adds a term to the spin equation (eq. 3.30):

$$\boldsymbol{\omega}_{a\eta} = \boldsymbol{\omega}_a + \boldsymbol{\omega}_\eta = \frac{e}{m}\left[a_\mu \boldsymbol{B} - \left(a_\mu - \frac{1}{\gamma^2-1}\right)\frac{\boldsymbol{\beta}\times\boldsymbol{E}}{c}\right] + \eta\frac{e}{2m}\left[\frac{\boldsymbol{E}}{c} + \boldsymbol{\beta}\times\boldsymbol{B}\right] \tag{3.46}$$

where η is a dimensionless constant equivalent to g, given by:

$$\eta = \frac{4d_{\mu^+}m_\mu c}{\hbar}\,, \tag{3.47}$$

where d_{μ^+} is the magnitude of the muon electric dipole moment vector, $\boldsymbol{d}_{\mu^+}$. It was explained previously that one of the fundamental principles underlying the $g-2$ measurement is that the muon precession vector must be perfectly aligned with the vertical magnetic field in order to observe the strongest possible precession signal. Any component of the magnetic field away from vertical will weaken the $g-2$ signal since the precession vector ω_a will not be vertically aligned.

The effect of a muon EDM on the spin precession vector is exactly analogous to the effect of a radial field component; the additional torque generated by the interaction of the muon EDM vector with the motional electric field acts radially, introducing a radial component to the direction of the total precession frequency vector $\boldsymbol{\omega}_{a\eta}$ and tilting it away from the vertical axis slightly. This is illustrated in 14. The magnitude of the precession plane tilt is given by:

$$\delta = \tan^{-1}\left(\frac{\omega_\eta}{\omega_a}\right) = \tan^{-1}\left(\frac{\eta\beta}{2a_\mu}\right). \tag{3.48}$$

It is obvious from equation 3.46 that the measured precession frequency would be increased slightly by the presence of a non-zero EDM; however, for any physically possible EDM value (i.e. any value of $d_\mu < 1.9\times10^{-19}\ e\cdot\text{cm}$ [2]), ω_a greatly dominates over ω_η and the measured precession frequency is unlikely to be altered to such a level that the size of d_μ could be extracted confidently from this measurement. Figure 15 shows the dependence of the tilt angle on d_μ. For very large d_μ, ω_η dominates over ω_a and the corresponding tilt angle is large; however for low EDM values, the relationship between ω_η and ω_a is linear; the tilt angle δ increases linearly with increasing d_μ and $\omega_a \gg \omega_\eta$. Thus it can be seen from figure 15 that for any physically possible value of d_μ, the fractional increase in ω_a due to an EDM will most likely be imperceptible.

Using Δa_μ to set a maximum limit on d_μ

The magnitude of a_μ can be used to place an upper limit on the size of a physically possible muon EDM by assuming that a large EDM is responsible for the discrepancy between a_μ^{exp} and a_μ^{th}. The fractional change in the precession frequency due to an EDM is given by:

$$\begin{aligned}\frac{\omega_{a\eta}}{\omega_a} &= \sqrt{1+\frac{\omega_\eta}{\omega_a}}\\ &= \sqrt{1+\delta^2}\\ &\approx 1+\frac{\delta^2}{2}\\ &= 1+\frac{\eta^2\beta^2}{8a_\mu^2}.\end{aligned} \tag{3.49}$$

Letting $a_\mu = a_\mu^{BNL}$, where the discrepancy from the SM was $\Delta a_\mu(E821-SM) = (261\pm80)\times10^{-11}$, and setting the upper bound of this equal to the entire difference in precession frequency yields

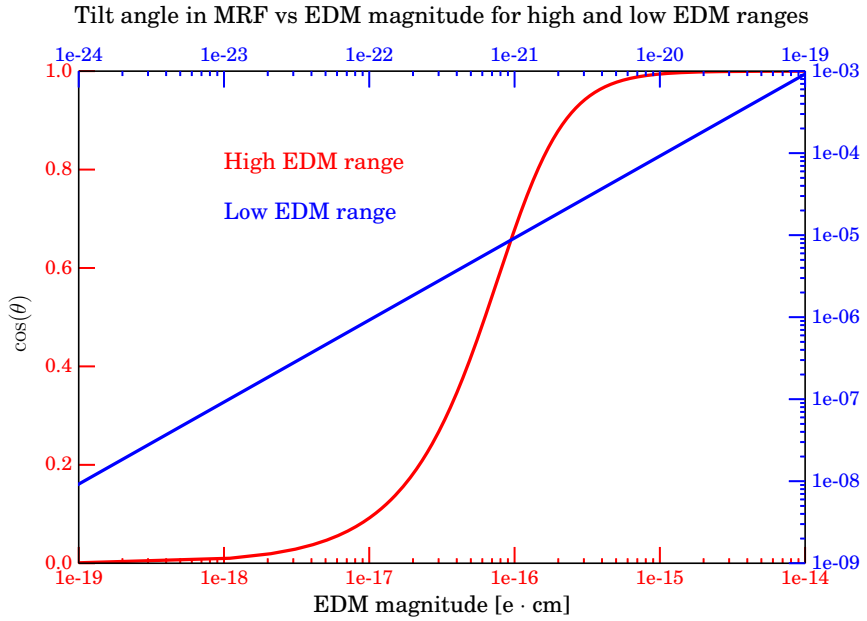

Figure 15: The angle from the horizontal plane as a function of EDM magnitude for high ($1\times10^{-19}-1\times10^{-14}$ $e\cdot$cm) and low ($1\times10^{-24}-1\times10^{-19}$ $e\cdot$cm) ranges.

an upper limit for d_μ:

$$\begin{aligned}\Delta a_\mu = (261+80)\times10^{-11} &= \frac{\eta^2\beta^2}{8a_\mu^2} \\ \implies d_\mu &\leq 2.6\times10^{-19}\ \text{e.cm}\ .\end{aligned} \tag{3.50}$$

Searching for an increase in precession frequency will be very difficult, given that the expected increase will be almost negligible, and is also not a very sensitive analysis technique from a systematic perspective; d_μ would need to be inferred indirectly from the measured precession frequency increase, but would also need to be identified from a range of ambiguous sources as the unique cause of such an increase. Fortunately, the tilt angle δ introduces an independent oscillation into the measured data which can be observed in two separate ways.

Direct measurement of precession plane tilt angle

The vertical tilt angle δ, shown in figure 14, causes an oscillation in the average vertical angle of the emitted decay positrons. Such an oscillation is at a frequency equal to $\omega_{a\eta}$, but – importantly

– 90° out of phase with the $g-2$ oscillation ω_a, allowing it to be easily distinguished from the usual precession oscillation, and any other sources of vertical oscillation that might exist.

The phase difference of vertical oscillation is a direct consequence of the positrons being preferentially emitted in the direction of the muon spin vector. It was explained previously that the ω_a oscillation has maxima when the muon spin vector is aligned with the muon momentum direction, and minima when the spin and momentum vectors are antiparallel. The maxima of the ω_η oscillation occur when the muon spin vector is directed radially outwards, since this is the point at which the precession plane tilt acts to emit the positrons with a component in the vertically upwards direction. The minima occur when the spin vector is directed radially inwards, since the precession plane is tilted vertically downwards and so the direction of the emitted positrons has some component vertically downwards. Thus, the maxima of the EDM oscillation are 90° out of phase with the maxima of the $g-2$ oscillation. This phase shift is crucial to the EDM measurement, as it is the signal that distinguishes an EDM oscillation from other oscillations that would be in phase with the $g-2$ oscillation.

The Fermilab $g-2$ experiment is equipped with tracking detectors that are designed to measure both the spatial profile and the momentum spread of the beam. They are able to measure the momentum of the decay positrons and extrapolate the magnitude and direction components of the positron momentum back to the muon decay position. The oscillation in the average vertical angle of the decay positrons can hence be determined directly using the tracking detectors. This method is expected to yield the greatest improvement in the sensitivity to the muon EDM since it is more robust against certain systematic effects than the calorimeter method (described below).

The BNL experiment was equipped with a traceback system that was used to attempt to directly measure the tilt angle in this way. By fitting an oscillation varying with the $g-2$ frequency and 90° out of phase with it, the uncertainty on the amplitude extracted from the fit was predominantly statistical, with a value of $-0.04\times10^{-19}\ e\cdot\text{cm}$. The systematic errors on this measurement were negligible compared to the statistical uncertainty. This value corresponded to an upper limit of [2]:

$$|d_{\mu^+}| < 3.2\times10^{-19} e\cdot\text{cm (95\% C.L.)}\ . \tag{3.51}$$

The tracking detector system in the new experiment is greatly improved from the system used at

BNL; as well as having greatly increased resolution and being optimised for maximal acceptance, it is able to run from much earlier times in the muon fill and will be used for the entire $g-2$ data-taking period. As such it will be able to record orders of magnitude higher statistics (number of tracks). There are also two locations for the tracking detectors, at 180° and 270° from the inflector exit (see chapter 4 for a detailed diagram) so the azimuthal acceptance is twice as large as in the previous experiment. The tracker-based method in the BNL experiment was statistically limited, and since the detectors are geometrically optimised and can switch on far earlier, the expected direct improvement in the tracker-based method this time around is significant; the new experiment anticipates a reduction in the current limit by a factor of 100.

One serious consideration that was made in the design of the tracking detectors was that they should have a radial and vertical acceptance that matches the true beam profile as accurately as possible. Any acceptance effects leading the trackers to reconstruct the beam at a higher radius, or higher mean vertical position, can directly bias the EDM search. The tracker acceptance has been studied extensively in simulation, and discussion of this is presented in chapter 7.

Determining precession plane tilt from a measurement of an asymmetry in the vertical positions of the detected decay e^+

The oscillation in the vertical angle of the decay e^+ can be indirectly determined by measurement of an oscillation in the vertical position of the arrival of the decay e^+ in the detectors. This could be determined using the trackers, which are optimised for position resolution, but measuring this oscillation using the calorimeters will yield a factor of 12 more statistics, since there are 24 calorimeters and only 2 tracking stations. The measurement principle here is to look for an oscillation in the up-down asymmetry in the number of e^+ detected in the top and bottom halves of the calorimeters, given by:

$$A(v) = \frac{N(up) - N(down)}{N(up) + N(down)} \,. \tag{3.52}$$

This is the general measurement principle that was used to place the upper limit on the muon EDM in the BNL experiment. Figure 16 shows a plot from simulated data (with an unphysically large value of d_μ to exaggerate the effect) which shows the difference between the number oscillation time spectrum measured using events from the top and bottom halves of the calorimeters only. At BNL, the technique was victim to numerous sources of systematic error, arising mainly from

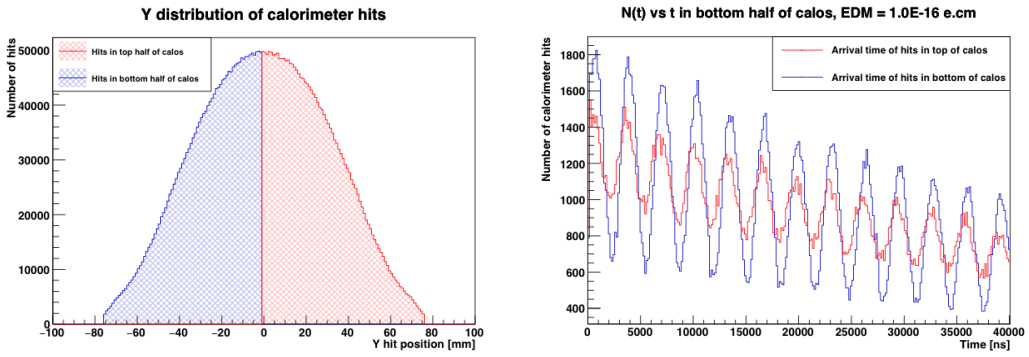

(a) Vertical position of calorimeter hits

(b) N(t) vs t for top and bottom halves of the calorimeters.

Figure 16: Plots from simulation illustrating the different amplitudes of oscillation of the number function N(t) in the top and bottom halves of the calorimeter, caused by the tilted precession plane due to a muon EDM. An unphysically large EDM of 1.0×10^{-16} e.cm has been used to exaggerate the effect.

detector misalignment. Since the oscillation about the mid-plane of the calorimeter is recorded, any shift in the vertical location of the detectors will seriously affect the sensitivity to this oscillation. The calorimeters in the Fermilab $g-2$ experiment have improved spatial resolution since they are segmented both radially and vertically, and so this systematic can be reduced, but not completely avoided. By contrast, the tracking detector method is less sensitive to detector misalignment (apart from in the sense that poor misalignment of the tracking detectors will affect the quality of the track reconstruction), since the principal uncertainty on that measurement is the error on the mean vertical position recorded as a function of time.

Another reason why the tracking detector method is expected to be more sensitive is that it is robust against any weakening of the signal caused by the bending of the e^+ tracks in the fringe field region. The magnetic field in the storage region is incredibly uniform, but the trackers are situated just inside the SR at a lower radius; the magnetic field components vary significantly in this region. This causes the tracks to bend from their usual trajectories; as such, a positron emitted with some positive ertical component may actually be detected in the bottom half of the calorimeter, and vice versa, since it can deviate from its birth trajectory by the time it reaches the calorimeters. The tracking technique is immune to this effect since it can propagate the trajectory of the e^+ through the varying field to get an accurate approximation of the e^+ momentum direction components at the μ^+ decay position.

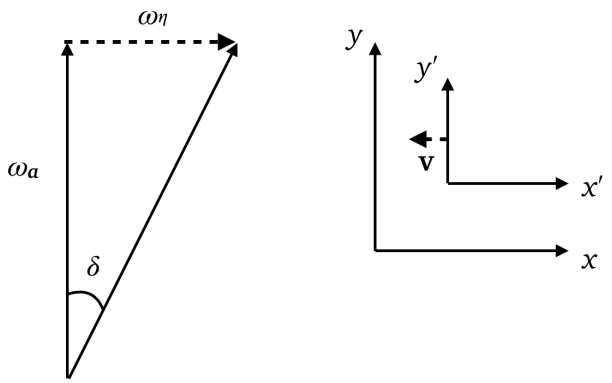

Figure 17: The positron momentum is Lorentz boosted, resulting in the electron momentum tilt being much smaller than the tilt angle delta in the MRF. The primed quantities illustrate the boosted frame.

3.4.2 Relativistic effects on the vertical angle measurement

The angle that is measured by the $g-2$ detectors is the average vertical angle in the decay positron momentum direction in the lab frame. This angle is much smaller than the EDM tilt angle in the MRF, since the momentum experiences a Lorentz boost which results in a reduction in the tilt angle. Considering the diagram in figure 17, the angle δ' denotes the reduced vertical decay angle in the lab frame. In the MRF, letting ω_η point in the $+x$ direction and ω_a in the $+y$ direction, the tilt angle δ is given by:

$$\tan\delta = \frac{\Delta x}{\Delta y}\,. \tag{3.53}$$

Boosting into the lab frame gives:

$$\Delta x' = \frac{\Delta x}{\gamma} \qquad \text{and} \qquad \Delta y' = \Delta y\,. \tag{3.54}$$

Thus:

$$\tan\delta' = \frac{\Delta x'}{\Delta y'} = \frac{\gamma\Delta x}{\Delta y}\,, \tag{3.55}$$

and

$$\delta' = \tan^{-1}\frac{\Delta y}{\gamma\Delta x} = \tan^{-1}\left(\frac{\tan\delta}{\gamma}\right). \tag{3.56}$$

This is the maximum angle that can be observed by the detectors. There is an additional reduction due to an acceptance factor of approximately 10%, which arises due to the fact that the detectors

mostly sample positrons that were not emitted in the direction of the greatest tilt angle. This factor is discussed in detail in section 3.4, where an attempt to parameterize it using simulation is presented.

3.4.3 Maximising sensitivity to muon EDM using asymmetry arguments

In a similar way to the treatment for the ω_a measurement, the statistical significance of the EDM measurement can be maximized by selecting only e^+ of a certain momentum range. However, the asymmetry function $A(y)$ has a different dependence on the e^+ momentum than for the ω_a oscillation. The statistical sensitivity of the vertical oscillation measurement is maximised when the vertical component of NA^2, NA_v^2, is maximised. The functional form of this asymmetry is plotted in figure 18, and is given by:

$$A_{EDM}(y) \propto \frac{\sqrt{y\left(1-y\right)}\left(1+4y\right)}{\left(5+5y-4y^2\right)}, \tag{3.57}$$

with a corresponding figure-of-merit expression:

$$NA^2_{EDM}(y) \propto \frac{y\left(1-y\right)^2\left(1+4y\right)^2}{\left(5+5y-4y^2\right)}, \tag{3.58}$$

where y is again the fractional energy of the e^+ in the laboratory frame. In contrast to the functional form for the $g-2$ asymmetry, $A_{g-2}(y)$, given above, $A_{EDM}(y)$ becomes 0 when e^+ of maximum energy are considered, the figure-of-merit NA^2_{edm} is maximised for e^+ of medium-range energy fraction. This relationship has been studied in simulation in order to determine the energy selection that will yield the strongest EDM signal.

3.5 Summary

The physical principles underlying the measurement technique for the anomalous magnetic moment, a_μ, and the muon EDM have been explained in this chapter. The following chapter will

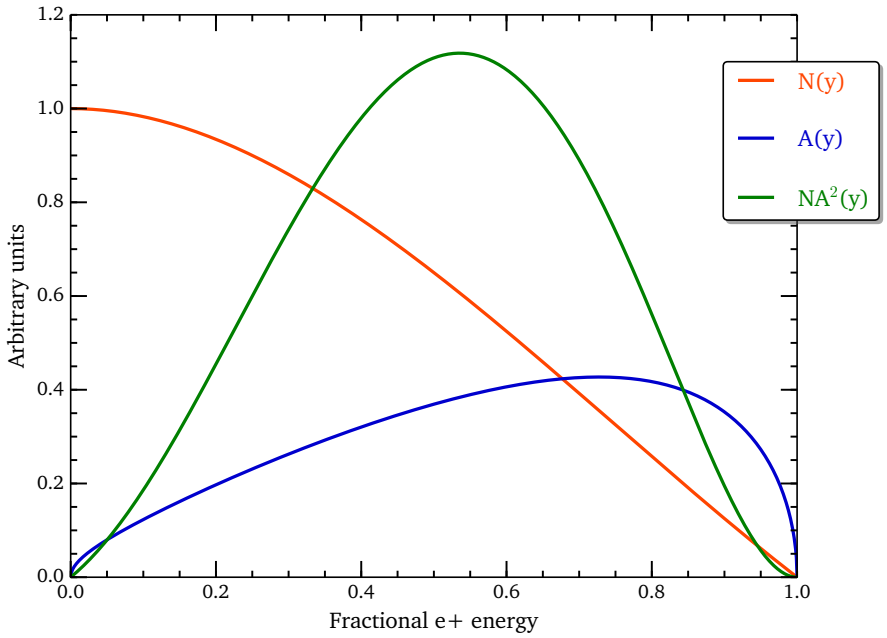

Figure 18: Plot showing the number function, N, the asymmetry, A, and the statistical figure-of-merit NA^2 for the EDM vertical oscillation signal. The EDM sensitivity is greatest for mid-range energies.

describe the experimental hardware.

Chapter 4

The $g-2$ experiment

The Fermilab muon $g-2$ experiment uses the Storage Ring measurement technique in which a beam of muons is injected into a magnetic storage ring with a vertically aligned field, in order to probe the rate of the precession of the μ^+ spin vector about the magnetic field axis, and from this determine the value of a_μ. This technique has been employed in previous $g-2$ experiments since its invention in at CERN in the 1960s [14]. This chapter outlines the technical aspects of the experimental setup.

The $g-2$ experiment can be broken down into the following stages:

1. **Muon production**: pions are produced from a beam of protons incident on a high-Z target; the pions decay, producing a polarized beam of muons to be delivered to the $g-2$ storage ring.

2. **Muon delivery to the magnetic storage ring**: the muon beam is guided through a gap in the SR magnet to deliver it to the storage region where the muons will circulate.

3. **Muon precession**: muons circulate around the SR and precess about the vertically aligned magnetic field, until they decay to positrons.

4. **Positron detection**: a suite of 24 electromagnetic calorimeters counts the number of decay positrons as a function of time in order to obtain ω_a.

4.1 Muon production

Figure 19 shows a schematic of the beamlines in the Fermilab accelerator complex. The booster produces a bunched beam of 8 GeV protons, which is sent via the Linac to the recycler ring. One booster pulse contains 4×10^{12} protons, which is too high for the required decay positron intensity at the $g-2$ detectors. In the recycler, the beam is re-bunched into four bunches of 1×10^{12} protons each, with at least 10 ms between bunches in order to satisfy the rate requirements of the detector data acquisition (DAQ) systems. The length of the bunches is less than 120 ns, which is less than the cylotron period of the muons in the storage ring (149 ns). The average pulse rate is 12 Hz.

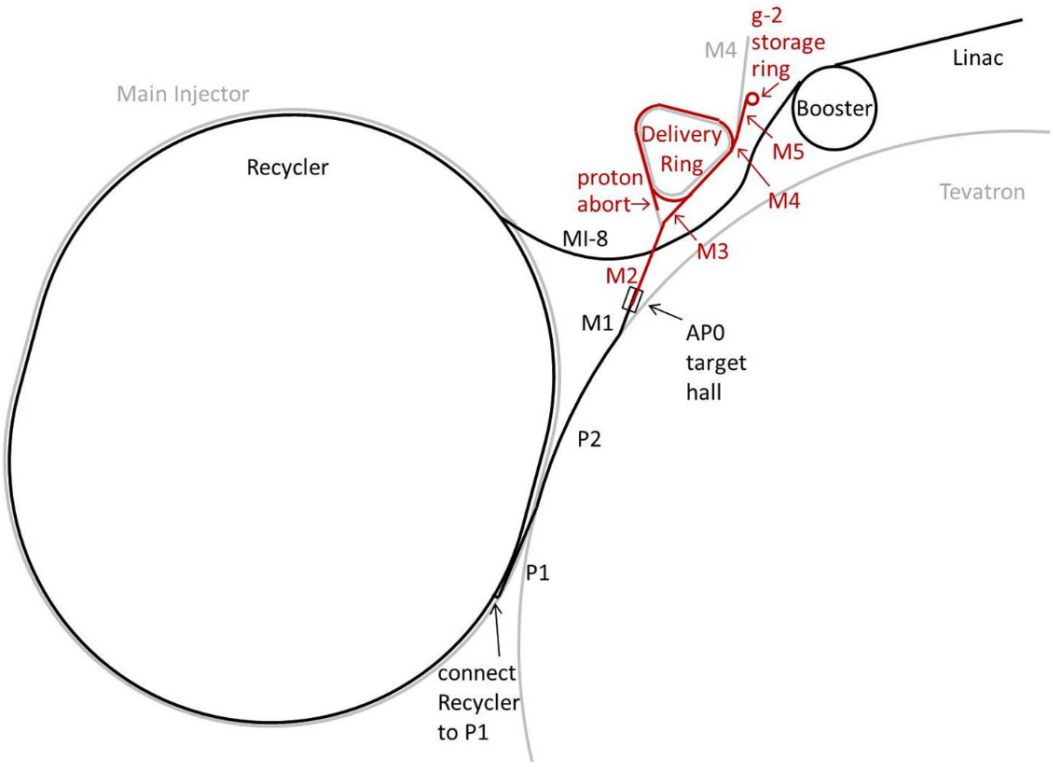

Figure 19: The Fermilab accelerator complex. Protons follow the black line. They are accelerated in the Linac and booster before being re-bunched in the recycler. They then travel through the P0, P1 and P2 lines to the AP0 target hall. The secondary pion beam (in red) travels through the M2 and M3 lines, around the delivery ring (DR), where pions and daughter muons circulate until all of the pions have decayed. The muon beam is then sent to the $g-2$ storage ring via the M4 and M5 beamlines. Image taken from [13].

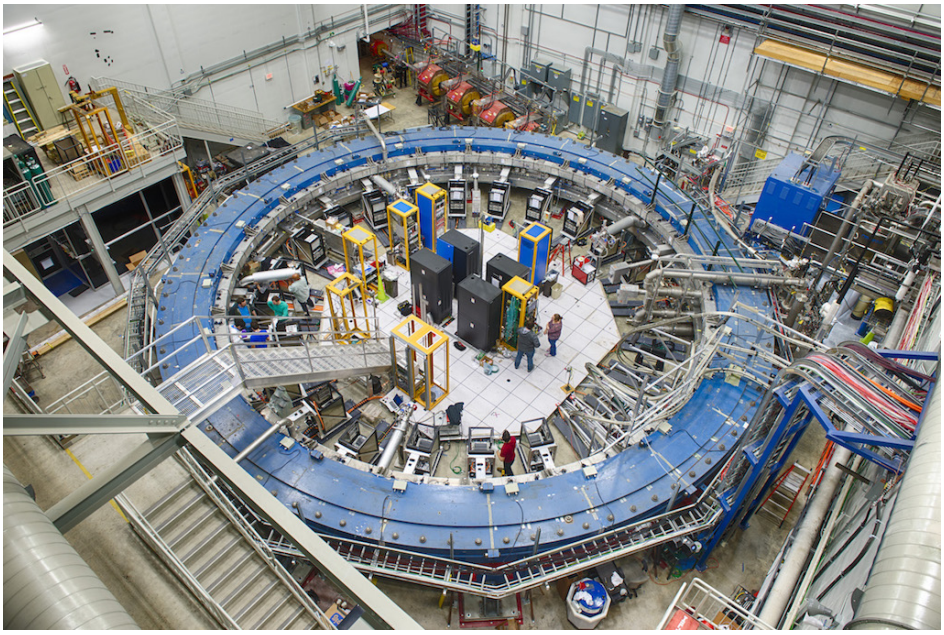

Figure 20: The $g-2$ storage ring at Fermilab.

After the beam has been re-bunched, the beam is directed to the pion production target station, which uses a modified version of the Tevatron antiproton production target, but optimised to produce π^+. The target station consists of an inconel pion production target, a lithium lens to focus the pions after production, and a pulsed magnet, used to select π^+ of momentum 3.115 GeV/c (just above $p_m = 3.094$ GeV/c) and bend them into the M2 beamline. The resulting π^+ beam travels along the M2 and M3 beamlines for a long enough time for the majority of the pions to decay to μ^+. The muons, undecayed pions and any remaining protons in the beam are directed into the delivery ring (DR). Here, the beam orbits until any remaining π^+ have decayed to μ^+, and the protons are separated out of the beam. The protons have a large enough mass to be removed using a kicker magnet. After these beamlines, a pure beam of polarised μ^+ is delivered to the storage ring.

4.2 Muon injection to the magnetic storage ring

The μ^+ beam enters the storage ring via an inflector magnet, which is designed to shield the muons from the storage ring magnetic field such that they are almost unperturbed on arrival in the storage region. The ideal muon orbit radius is referred to as the magic radius, since it is the orbit radius of muons with p_m. The inflector is almost tangential to R_0, but not quite, so the

muons begin to orbit the storage ring at a radius that is slightly offset from R_0. This offset must be corrected for to avoid the muons leaving the storage region and becoming 'lost'. The radial offset from R_0 at injection is corrected for by a series of three kicker magnets (together referred to simply as the kicker), located at 90° relative to the inflector exit. The kicker pulses during the first orbit, applying a tangential force to the circulating muons to 'kick' them onto their ideal orbit.

Throughout this thesis, reference will be made to two different coordinate systems that define the location of the beam, and of the detectors. Both of these coordinate systems are depicted in figure 21. The first coordinate system, the 'world' coordinate system, is a 'top-down' view of the SR, with the vertical coordinate coming 'out of the page', and the inflector exit defining the beginning of a circle with radius R_0 sweeping out an angle ϕ, which is equal to 0 at the inflector exit. The second important coordinate system is the 'beam' coordinate system. This coordinate system defines an azimuthal slice of the SR at a particular value of ϕ. The centre of the ring is the origin of the coordinate system, and the direction tangential to R_0 defines the 'out-of-the-page' direction.

Since there is a small momentum spread of the stored μ^+ beam, there is a corresponding spread in the orbit radius. A set of collimators are used to remove the μ^+ at extreme radii, in a process called scraping. Scraping starts at approximately 8 μs after muon injection and lasts for 5 μs. At the very beginning of the muon fill, the quadrupole strengths are varied in order to move the beam radially backwards and forwards to direct the tails of the beam into the collimators and thereby removing any muons > 4.5 mm from the beam centroid. The resulting momentum spread of the stored beam is 0.15%.

The storage ring magnet provides only radial focusing of the muon beam in the ring. Vertical focusing is also required in order to prevent the muons slowly drifting up or down and eventually leaving the storage region. It is not possible to use magnetic focussing as this would perturb the vertical magnetic field. Instead, electrostatic quadrupoles are used to focus the beam vertically. Four sets of quadrupole plates are located symmetrically around the storage ring as seen in figure 22. The strength of the focusing provided by the quadrupoles is given by the field index:

$$n = -\frac{\kappa R_0}{\beta B}\,, \tag{4.59}$$

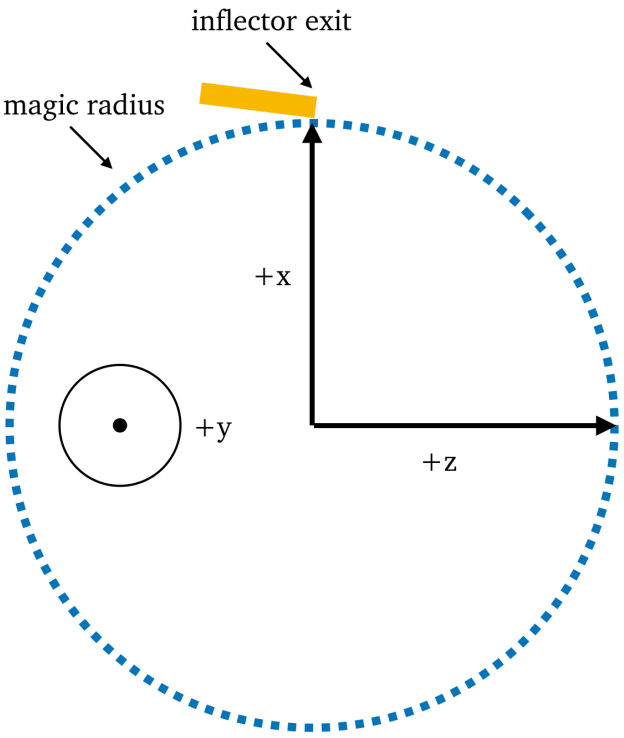

World coordinates

(a)

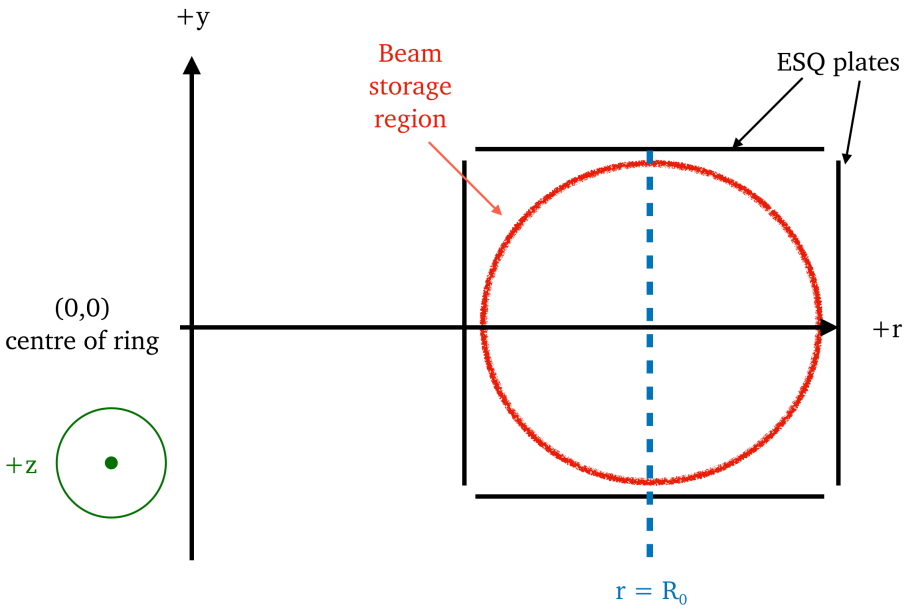

Beam coordinates

(b)

Figure 21: Diagrams (not to scale) of the coordinate systems defining the storage ring and beam position.

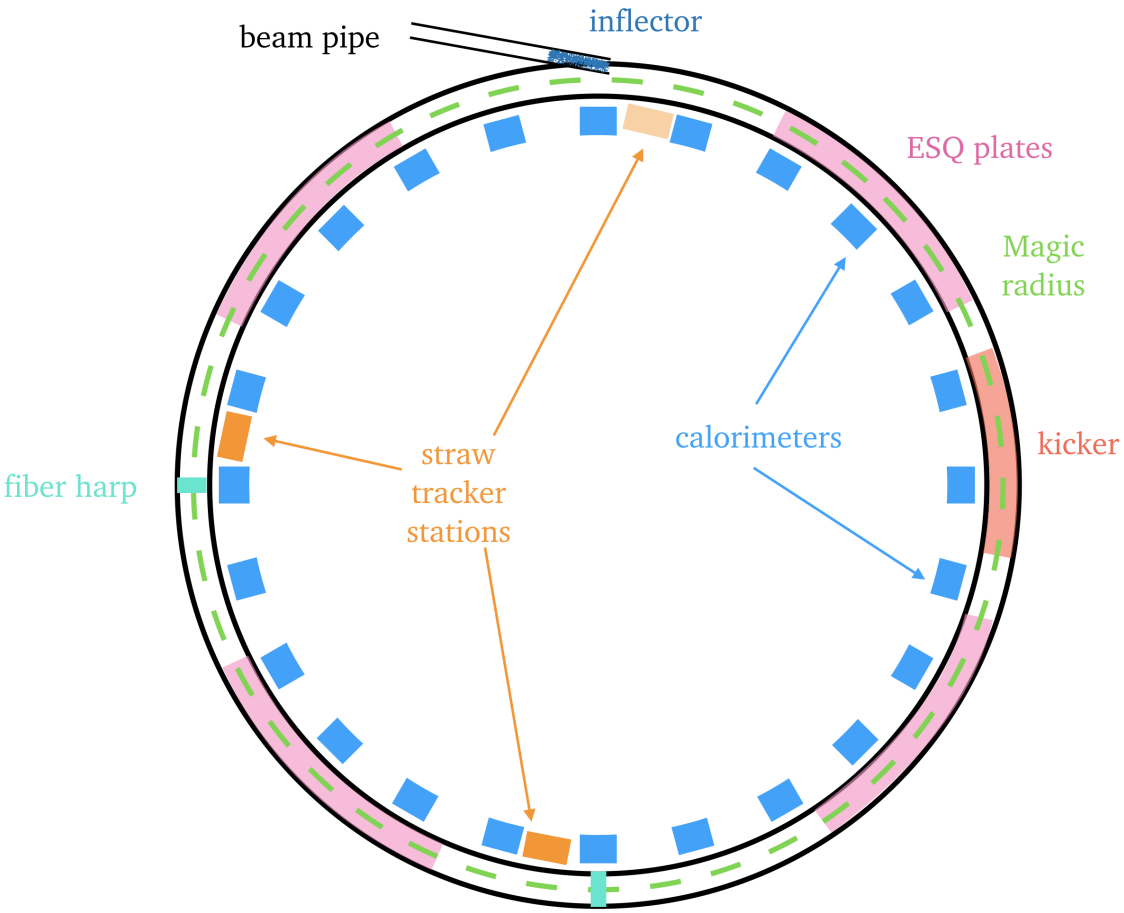

Figure 22: Schematic of the $g-2$ storage ring, showing the inflector and ideal muon orbit.

where R_0 is the magic radius, B is the nominal magnetic field strength and $\kappa = \delta E_r/\delta r$ is the field gradient. The field index can be chosen to achieve the desired run conditions, and must be set carefully in order to minimise some serious systematic errors on the ω_a measurement.

The quadrupole field provides a linear restoring force in the vertical direction, while the combination of the radial electric fields and vertical magnetic field causes a linear restoring force in the radial direction. These forces cause the stored muons to experience simple harmonic motion (SHM) in both the radial and vertical directions, causing the muons to oscillate periodically about their stored orbits both radially and vertically, with frequencies $\omega_x = \omega_c\sqrt{n}$ and $\omega_y = \omega_c\sqrt{1-n}$ respectively. These oscillations are called betatron oscillations. If a linear combination of the radial and vertical betatron frequencies is equal to an integer multiple of the cyclotron frequency, resonances can occur, which would cause the expansion of the muon beam until it was lost from the storage region. This could also lead to spin resonances, in which the muon spin is continuously rotated by a small amount on each successive betatron cycle. This effect would slowly alter the phase of the $g-2$ oscillation and have a serious effect on the determination of ω_a. Such effects can be avoided by careful choice of the operating strength of the quadrupoles.

4.3 Muon precession and coherent betatron oscillations

On their own, the betatron oscillations have a frequency much greater than ω_a, and so do not directly bias the ω_a measurement themselves. However, the radial betatron oscillations act to introduce a *coherent* oscillation with a frequency comparable to ω_a.

A given detector samples the beam exactly once per orbit from a fixed location. Since the betatron oscillations must have a different wavelength from the cyclotron frequency ω_c, the average radial position of the beam sampled by the detector varies slightly on each successive cycle. The cumulative effect of this is an apparent slow oscillation in the dectected average radial position of the beam, referred to as a coherent betatron oscillation (CBO). The effect is illustrated in figure 23. The blue line shows the radial betatron oscillation and the wavelength of the cyclotron oscillation is indicated by the vertical black lines. The radial position observed by the detectors (the black boxes) is indicated by the blue dots. The red line joining the blue dots illustrates the CBO, and it is evident that the period of the oscillation is much longer than ω_c. The CBO frequency, f_{CBO} is given by:

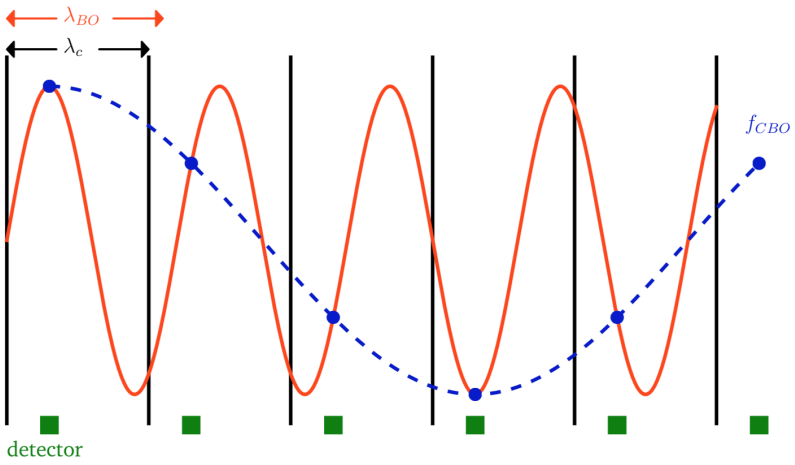

Figure 23: Cartoon depicting radial CBO.

$$f_{CBO} = \omega_c - \omega_x = \left(1 - \sqrt{1-n}\right)\omega_c \approx 470 \text{ kHz} . \tag{4.60}$$

This is close to the second harmonic of the anomaly precession frequency, ω_a. If f_{CBO}, or any of its harmonics, were equal to ω_a then it would not be possible to distinguish the $g-2$ oscillation from the CBO; again, this can be avoided by carefully setting the field strength of the focusing quadrupoles.

The muon spin precession frequency ω_s depends slightly on the betatron motion of the beam, since they introduce some $\boldsymbol{\beta} \cdot \boldsymbol{B} \neq 0$ component to equation 3.22, which is only valid when $\boldsymbol{\beta} \cdot \boldsymbol{B} = 0$ and $\boldsymbol{E} = 0$. The vertical betatron oscillations have the only significant effect on ω_s that requires a correction to be applied; this is known as the pitch correction, since the effect of the vertical oscillations is to cause the 'pitch' angle, ψ between the muon momentum and the horizontal plane to vary periodically:

$$\psi = \psi_0 \, cos(\omega_y t) . \tag{4.61}$$

where ω_y is the vertical betatron frequency. Using the approximations that all muons are at $p = p_m$ (i.e. ignoring the electric field correction), and that the momentum direction is perpendicular to the magnetic field vector, the correction can be given (approximately) as:

$$\omega_a' \approx -\frac{q}{m} a_\mu B_y \left(1 - \frac{\psi^2}{2}\right) = -\frac{q}{m} a_\mu B_y \left(1 - \frac{\psi_0^2 cos^2(\omega_y t)}{2}\right) . \tag{4.62}$$

Taking the time average of this oscillation yields the pitch correction:

$$C_p = -\frac{\langle \psi^2 \rangle}{2} = -\frac{\langle \psi_0^2 \rangle}{4} = -\frac{n}{4}\frac{\langle y^2 \rangle}{R_0^2}\,, \tag{4.63}$$

where n is the quad field index. The pitch correction, like the electric field correction, acts to lower the measured ω_a frequency and so the correction must be applied so as to increase the measured frequency. The pitch correction in the Brookhaven experiment was $+0.27 \pm 0.04$ ppm. This and the electric field correction were the only corrections to be applied to the ω_a measurement.

While not requiring an explicit correction, the horizontal CBO can have a considerably larger effect on the determination of a_μ than the vertical BO. A horizontal CBO with frequency close to, but not an exact integer of, the $g-2$ frequency will beat against the $g-2$ oscillation, and must therefore be accounted for in any fitting function to extract ω_a. The vertical BO, despite introducing the pitch correction, is comparatively small and dies away much faster than the horizontal BO, and can hence be ignored from the start times of the fit. The tracking detectors, introduced in section 4.4 and discussed in detail in chapter 5, will measure the radial and vertical position of the muon beam as a function of time throughout the fill, and can measure the horizontal CBO frequency, amplitude and phase accurately. They will also measure the average vertical position of the muons at the time of decay, enabling determination of the pitch correction.

4.4 Detector systems

Muons have a rest lifetime of 2.2 μs, which is time-dilated at the magic momentum to become 64 μs. The $g-2$ oscillation in the storage ring magnetic field has a period of 4.4 μs, so most muons will precess many times before decaying. The decay positrons from the circulating muons are measured for around 10 muon lifetimes, or $\sim$ 640 μs. The Lorentz boosted decay e^+ are emitted within 30° of the muon momentum direction; the high-energy e^+ that are accepted by the detectors are emitted within 2°. The emitted positrons have a lower momentum than the parent muons and will follow a path of lower radius, causing them to spiral into the centre of the ring where the detectors are located.

The main detectors for the ω_a measurement are a series of 24 electromagnetic calorimeters, evenly spaced around the ring. They are designed to measure the arrival time and energy of the

incident decay e^+ and count the e^+ with energy greater than a chosen energy threshold in order to record a signal from which ω_a can be extracted. Since the only use for the energy measurement is to select events above a threshold, and is not one of the experimental observables, there is a modest required precision on the energy measurement of 5% at 2 GeV.

Each calorimeter is composed of 54 PbF_2 crystals in a segmented 9×6 arrangement. The crystals of a calorimeter are shown in figure 24. When a relativistic positron passes through a crystal, Cerenkov light is produced and detected at the downstream end of the crystals, where it is read-out by silicon photo-multipliers (SiPMs). Each crystal is wrapped in a light-tight covering to prevent Cerenkov light produced in one crystal being transmitted to its neighbours. Using a Cerenkov medium produces a fast, short signal. This is crucial as the calorimeters are required to have a timing resolution of less than 100 ps for e^+ with kinetic energy greater than 100 MeV. The timing resolution is further aided by the segmented design, which also enables the calorimeter to identify showers separated either spatially or temporally. The calorimeter must have 100% efficiency in resolving showers with a time separation of greater than 5 ns, and a greater than 66% success rate at providing spatial resolution. These requirements are intended to reduce systematics due to pileup, where two or more positrons enter a single crystal close together in time, leading them to be reconstructed as a single particle with energy equal to the sum of the energy from the two incident particles. In addition to the resolution requirements, the calorimeter gain must be stable over a 200μs time period during the muon fill. To ensure maximal gain stability, a laser calibration system is used to monitor the gain with high precision and correct the reconstructed energy for any measured gain drifts.

As well as the calorimeters, which are responsible for measuring ω_a and detecting the key $g-2$ signal, there are a number of additional detector systems in the $g-2$ experiment. Two of these – the straw trackers and 'fiber harp' systems – are specifically designed to monitor the profile of the muon beam inside the SR. A good understanding of the muon beam profile is crucial for measuring ω_a accurately as there are a number of systematic effects associated with the changes in beam parameters as a function of time throughout the muon fill. Tracking detectors will be located at three[3] locations around the ring, directly in front of the calorimeters, in order to record the trajectories of the decay positrons as they travel from the decay point to the calorimeter.

[3]The 2017 experimental run included only two sets of tracking detectors, located at 180° and 270° from the inflector exit. A third detector has been constructed and is intended to be installed at the 5° location in future experimental runs.

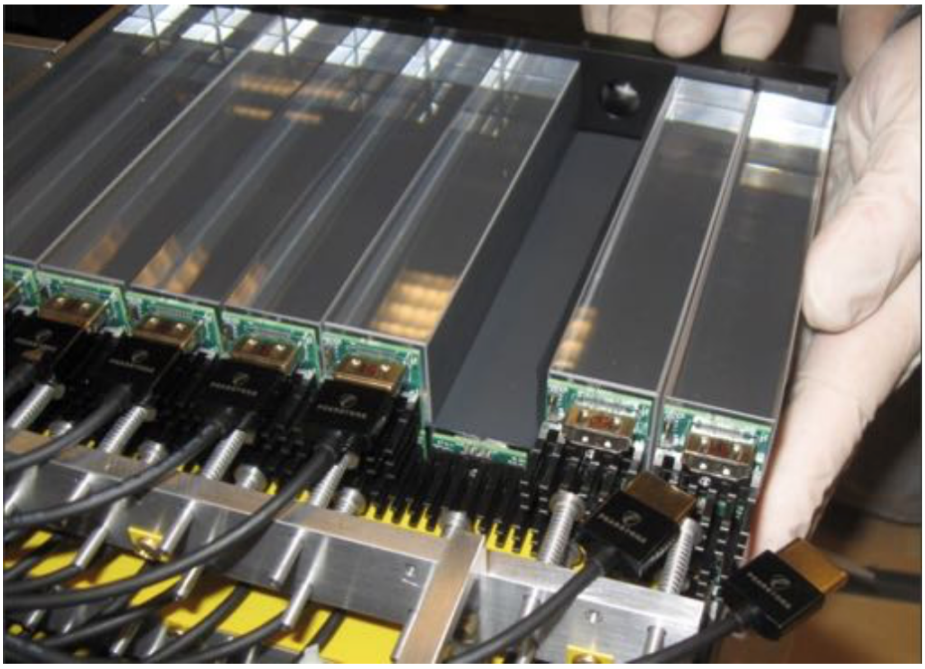

Figure 24: The PbF_2 crystals of a calorimeter being assembled. One layer of 9 crystals (with one crystal removed) can be seen.

These trajectories can be extrapolated back to the muon decay point, to provide information about the muon position at the time of decay. The tracks can also be extrapolated forwards to the calorimeters, to provide momentum information, improved spatial and timing resolution of the incident e^+. Such information will be used to corroborate the calorimeter's pileup identification. The tracking detectors provide a non-destructive measurement of the beam profile, so they can monitor the beam for the entire duration of the experiment. These detectors are discussed in detail in chapter 5. An image of the tracking detectors taken from a camera located in the beam region of the SR is shown in figure 25.

Another system designed to measure the beam profile is the fiber harp detectors. Each fiber harp contains seven parallel scintillating fibers; such a detector is shown in 26a. The retractable harps are located in the muon beam, positioned at right-angles to one another in order to measure the radial and vertical components of the beam profile. Locating the detectors inside the beam means that the muon profile can be measured directly, without the uncertainties associated with extrapolating from the decay positron trajectories. However, this does mean that they are destructive to the beam, since the circulating muons will pass through the harps several times before decaying, and significant multiple scattering will occur each time. Unlike the straw trackers, the harps will

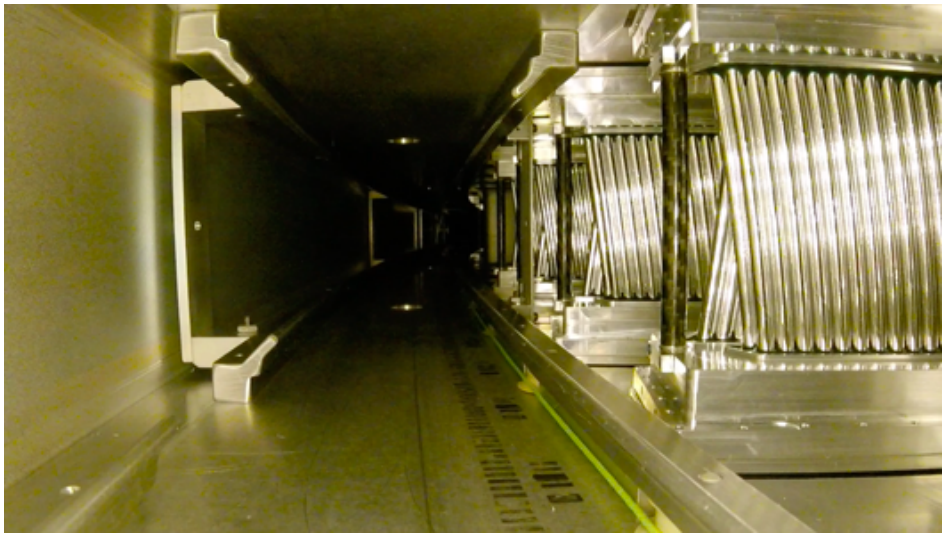

Figure 25: The tracking detectors as viewed from the inside of the storage ring.

not be used during normal running conditions, instead making their measurements during a series of dedicated runs for studying the beam. The plot in figure 26b shows the signals obtained on each of the fibers in the harp. Each line on the plot shows the intensity in an individual fiber signal as a function of time. Two different oscillations are apparent in the data; the slow oscillation of the CBO, and the fast rotation at the cyclotron frequency. Comparison of signals from the different fibers illustrates that the CBO amplitude varies as a function of radius (or height for a Y-harp). The measurements are direct and destructive; the circulating muons pass through the scintillating fibers themselves. The interaction with material causes the muons to lose energy and be deflected from their design orbit, so data from fiber harps is used only to study the beam parameters and not in the final ω_a analysis.

The injection beam monitoring system (IBMS) consists of two scintillating fiber detectors. The first is located upstream of the inflector, before the hole in the magnet yoke, and the second immediately before the inflector. A third detector is being installed in the 2018 summer shutdown at the downstream end of the inflector. The purpose of the detector is to monitor the beam profile throughout its injection to the SR, which is useful for beam tuning and providing feedback to the upstream accelerator teams. The beam can be tuned to match the acceptance of the SR in order to maximise the number of stored muons.

In order to accurately measure the injection time of a muon fill, scintillator counters, referred to

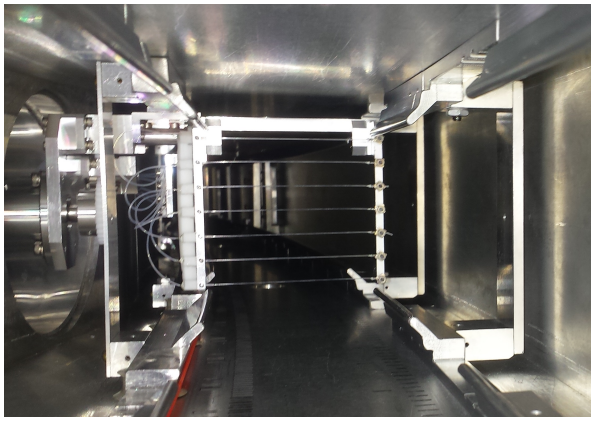

(a) The 'Y' fiber harp deployed in the storage ring.

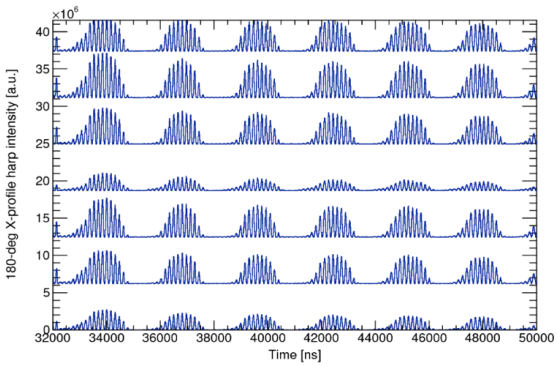

(b) Typical data from an 'X' fiber harp.

Figure 26: A photo of the 'Y' (vertical) fiber harp taken from inside the storage ring is shown in figure (a), and a plot of the data from an 'X' (radial) fiber harp is shown in (b). Each line in the plot represents the signal detected in an individual fiber; the intensity of the fiber signal is plotted as a function of time.

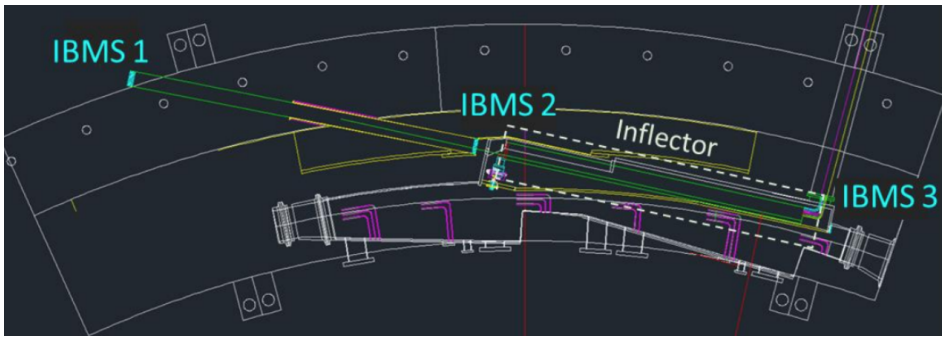

Figure 27: Locations of the IBMS detectors.

as the T0 detector, are placed in the opening to the storage ring. Their measurements allow the phases of data from multiple fills to be aligned, in order to avoid smearing the ω_a oscillation due to phase differences between the Fermilab accelerator clock and that of the $g-2$ experiment, which are independent systems.

4.5 The precision magnetic field

The measurement of a_μ requires determination of ω_a and ω_p, the free-proton precession frequency, to equal precision. The measurement principle for ω_a was described in the previous chapter; here, the storage ring magnet hardware will be described. The magnet is designed to provide a magnetic field of 1.4513 T strength, with a uniformity of 1 ppm when averaged over the full azimuth of the ring. It is this external B field that induces the two precession frequencies, ω_a

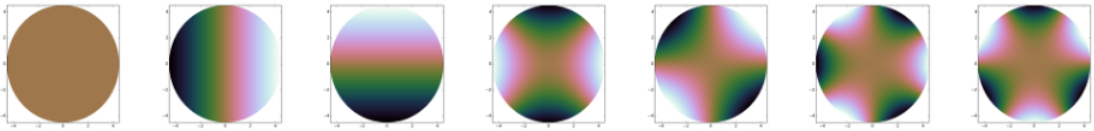

Figure 28: A diagram of the visualisation of the first seven terms in the multipole expansion of the vertical magnetic field. The pictures illustrate the symmetries across the muon storage region due to the different terms. From left to right, the moments are named: dipole moment (the 'main' moment which averages out uniformly over the region), and the normal quadrupole, skew quadrupole, normal sextupole, skew sextupole, normal octupole and skew octupole moments [67].

and ω_p, which is measured using a suite of NMR probes and calibration tools that will also be described in the following sections.

4.5.1 The storage ring magnet

The magnetic storage ring must provide a magnetic field of strength B = 1.4513 T as uniformly as possible over the full toroidal storage region with a major radius of $R_0 = 7.112$ m, and minor radius of 4.5 cm. The measurement requires a magnetic field directed entirely in the vertical direction, with no deviations. Such an exact field is forbidden by Maxwell's laws to exist over a finite space, however, and so the experiment is designed such that the unavoidable perturbations to the central field are minimised over the storage region (defined as a circle at a given azimuth, centred on R_0, with radius 4.5 cm). The uncertainty on the central field strength can be understood as the combination of several different possible symmetries over this region, referred to as 'multipoles' since each symmetry is due to an individual term in the 'multipole expansion' of the central magnetic field, given in equation 4.64. The first seven multipole moments are illustrated in figure 28. Each multipole represents a term in the expansion of the expression for the magnetic field strength for a given azimuthal slice of the SR. The expressions for the vertical and radial components of the magnetic field strength at a given azimuth, ϕ, are:

$$\begin{aligned} B_z(r,\phi) &= \sum_{n=0}^{\infty} \left(\frac{r}{r_0}\right)^n \left[a_n sin(n\phi) \; + \; b_n cos(n\phi)\right] , \\ B_r(r,\phi) &= \sum_{n=0}^{\infty} \left(\frac{r}{r_0}\right)^n \left[c_n sin(n\phi) \; + \; d_n cos(n\phi)\right] . \end{aligned} \tag{4.64}$$

where r_0 is the magic radius, and a, b, c and d are normalisation constants.

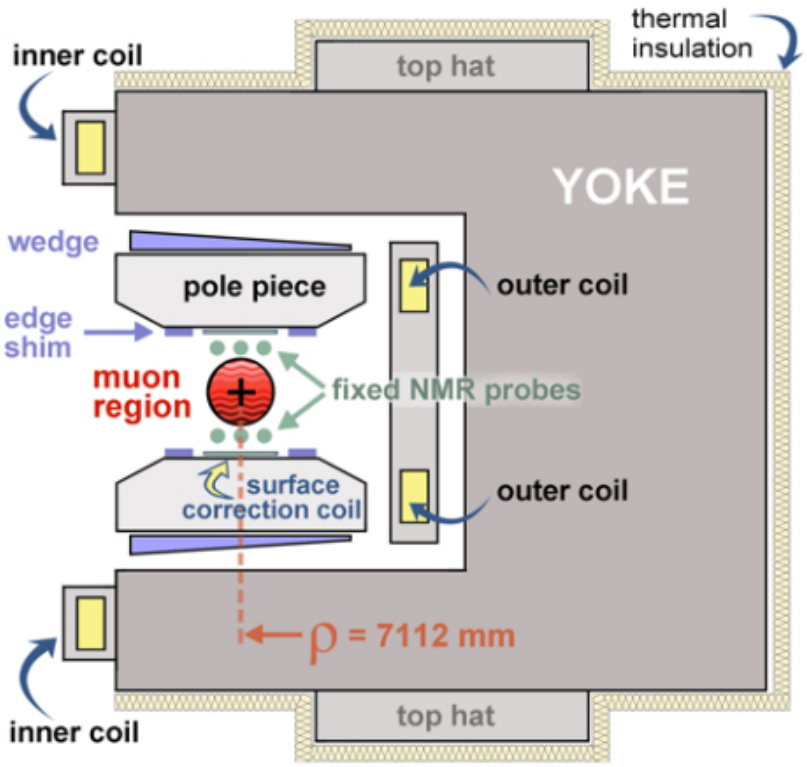

Figure 29: A diagram of the cross-section of the SR magnet. Taken from [68].

The SR magnet, shown in figure 20, contains many components devoted to averaging the dipole moment to perfect uniformity, and reducing the higher-order moments as much as possible. A diagram of the magnet's cross-section, illustrating the location of these components, is shown in figure 29. The magnet consists of:

- 3 superconducting NbTi/Cu coils
- 12 'C'-shaped steel yokes for flux return
- 72 high-purity steel poles (3 per yoke)
- In-built adjustment system of 1000 tunable knobs

To generate the required field strength of 1.4514 T, a current of 5176 A is supplied via three superconducting coils, two of which are located at the inner radius of the SR; the coil at the outer radius contains twice as much superconducting material as one of the inner coils in order to generate the same magnetic field as the two inner coils. The outer and inner coils are run with

opposing currents, leading to the generation of a vertically-directed field between them.

Each 'C'-shaped yoke surrounds a cavity containing the storage region in which the μ^+ circulate. The magic radius of 7.112 m is illustrated on the diagram in figure 29. The main pole pieces surround the storage region and provide the main (dipole) component of the field, which should average to 1.4513 T exactly. 'Top hats' are located on the top and bottom of the yoke, affecting the average field without affecting the higher-order multipoles. The rest of the magnet apparatus is devoted to the minimisation of the higher-order terms. Between the pole pieces and the upper and lower arms of the yoke are a set of steel wedge shims, which tune the dipole and quadrupole moments of the field. In order to maximise precision of the average field, the wedge shims must be completely flush against the pole pieces. To optimise this, each wedge has a 'shimming knob' which allows it to be moved radially inwards or outwards. Additional support is provided by a 'shim stack' of thin steel foils which can provide a slight tilt to push the face of the wedge even closer to the pole piece. Each wedge provides support to a 10° azimuthal range. Attached to the surface of the poles closest to the storage region are a set of edge shims which affect the quadrupole and sextupole moments. Additional steering of these components, as well as the dipole and octupole moments, is provided by small iron 'laminations' located on the surface of the poles. On top of the laminations are a set of surface coils which affect the higher-order multipoles. The surface coils are unique in that they are 'active' shimming devices, meaning they can be programmed during the experimental running; all of the other shimming components are passive and must be tuned beforehand.

4.5.2 Magnet shimming

Apart from tuning the surface coil currents, all other magnet shimming requires access to the SR and must take place when the experiment is not running. The mechanical shimming devices were all installed while the magnet was being assembled after its arrival at Fermilab, and the shimming campaign took place in 2016-2017 before the data-taking period began. Measurement tools were developed to probe the magnetic multipoles around the ring during shimming, such that the wedge pieces could be adjusted if necessary. The primary tool for measuring the magnetic field during shimming was a 'shimming cart' which could be moved around the entire circumference of the ring on a set of tracks designed for the calibration trolley (described below). On the cart was a lattice of 25 nuclear magnetic resonance (NMR) probes, as well as capacitive gap sensors

with a resolution of 70 nm to study the alignment of the pole pieces. In addition, the cart was mounted with retroreflectors to allow its position to be tracked using lasers with a resolution of 25 nm located at the centre of the SR [68].

The first phase of the shimming was to remove any discontinuities in the pole surfaces that could lead to significant deviations in the average field strength as a function of azimuth. Any measured discontinuities in alignment could be corrected for by adjusting the wedge shims and adding to the 'shim stack' if necessary. After the tilts of the pole pieces were optimised such that the pole pieces were in one continuous plane, the top hats and wedges were fine-tuned. The results from the shimming trolley analysis following the magnet shimming, prior to the Physics data-taking, is shown in figure 30. The dipole field strength as a function of azimuth for the current experiment are shown in red, compared to the same data from the Brookhaven experiment. The azimuthally averaged result is shown in figure 31.

4.5.3 Magnetic field measurement and calibration

There are several independent systems designed to measure the magnetic field in the SR. The main tool is an NMR trolley, which contains an array of proton NMR probes and can travel around the entire azimuth of the SR in order to map out the magnetic field seen by the μ^+. The trolley will measure the field during dedicated 'trolley runs' in-between data-taking runs, since the trolley will obstruct the path of the circulating μ^+ and cannot be in the ring while it is receiving beam. The SR contains a special trolley 'garage' to house the trolley while it is not being used. The NMR probes contain petroleum jelly, which is a proton-rich medium in which the protons will undergo Larmor precession proportional to the magnetic field strength. The frequency precession on the probes is 10 ppb [68]. Since the trolley cannot measure the field during experimental running, a suite of 378 'fixed probes' are located around the SR, mounted in grooves cut into the top and bottom surfaces of the vacuum chambers which reside in the magnet gap. These are also NMR probes containing petroleum jelly, and they can monitor the drift of the magnetic field in-between trolley runs, providing feedback to the magnet power supply such that its nominal field magnitude can be stabilised.

A maximally precise measurement of $\boldsymbol{\omega_p}$ requires determination of the Larmor frequency of truly 'free' protons. The protons in petroleum jelly are not truly free as they can experience chemical interactions that are not well understood. In order to extract the free proton precession

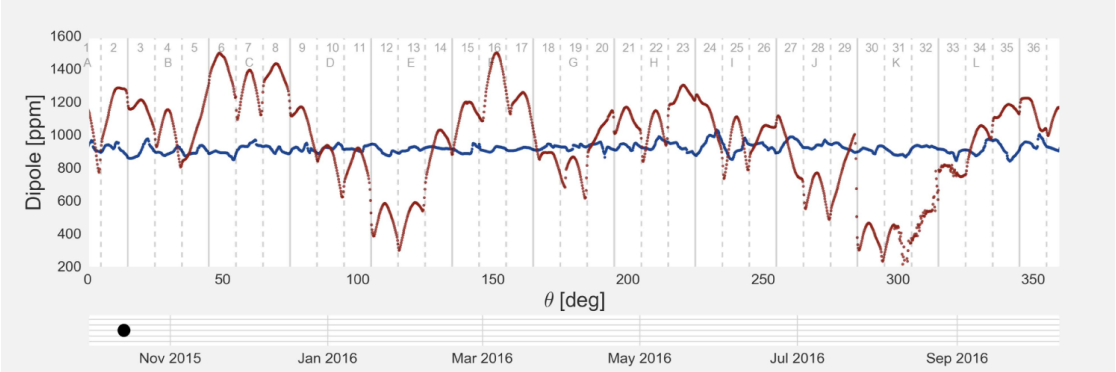

(a) August 2015

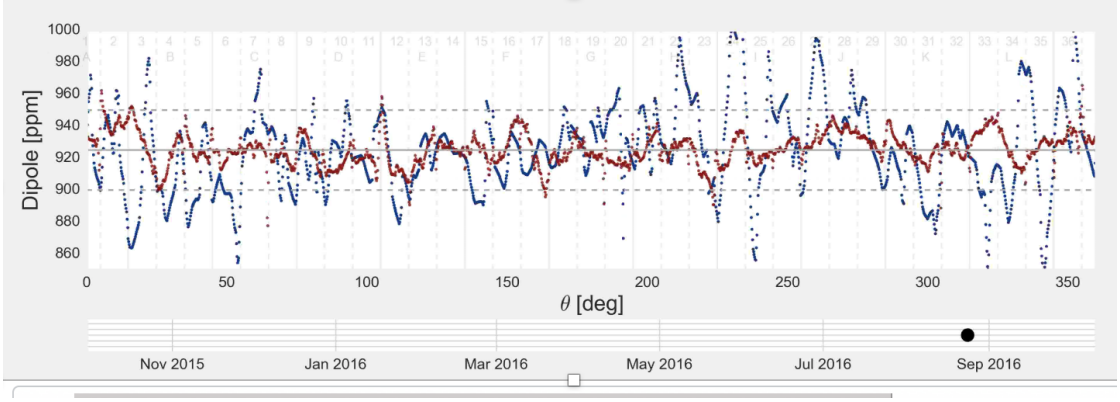

(b) August 2016

Figure 30: Each plot shows the dipole field strength as a function of azimuthal position, where $\theta = 0$ is the inflector exit. In both plots, the red line represents the measurements for this experiment and the blue line is the final result obtained for the Brookhaven experiment. Part (a) is the result obtained prior to the 'rough' shimming campaign in August 2015, and part (b) shows the final result prior to experimental running, measured in August 2016. In plot (b), the mean dipole strength is indicated by the solid grey line and the dashed grey lines indicate $\pm 25 ppm$ around the central value which was the target for this experiment. The data was recorded prior to the detectors and other systems being installed in the ring. This figure is taken from [67], where the shimming procedure is documented in full.

frequency, a calibration system consisting of several different tools was developed. The principal calibration will be provided by a so-called 'plunging probe', containing an ultra-high purity water sample with well-understood diamagnetic properties. The frequency of the protons in the water of the plunging probe can be compared to the frequency measured by the trolley and the fixed probes. The plunging probe is attached to a mechanical motion controller to move it out of the way of the beam, and it can be precisely controlled in order to align it with the trolley to ensure they are sampling the same region of the field.

In addition to the plunging probe, two water probes and a ^{3}He probe, together termed the Absolute Probe System (APS), are used to make independent measurements of the free proton precession frequency as a cross-check of the plunging probe measurements. One of the water probes is the one that was used in the BNL experiment, which was originally designed for maximal precision and has well-measured impurities and magnetic perturbations. It achieved a 50 ppb precision. There is also a new water probe, similar in design to the BNL one but with more stringent testing of its magnetic properties; its intended precision is 35 ppb. Using a ^{3}He probe provides an additional cross-check of the free proton frequency with different, uncorrelated systematics. The measurements of the absolute probes are not performed in the storage ring, but instead calibrate the measurements of the plunging probe by placing the plunging probe in the same magnetic field as the APS in an external 1.45 T test magnet at Argonne National Laboratory (ANL).

4.6 Summary

Since the SR magnet completed its epic journey to Fermilab in June 2013, the magnet shimming campaign was completed and gradually all of the beam focusing devices, detectors and supporting hardware were installed. The first muons arrived in the SR in June 2017, during a 6-week commissioning run that took place prior to Fermilab's summer shutdown, in order to test the full experimental operation for the first time. Full data-taking began again in November 2017 and is ongoing at the time of writing. The work presented in the following two chapters focuses extensively on the construction and testing of the straw tracking detector system, while the beam profile measurements recorded using the tracking detectors during the first months of the $g-2$ experimental running are presented in later chapters.

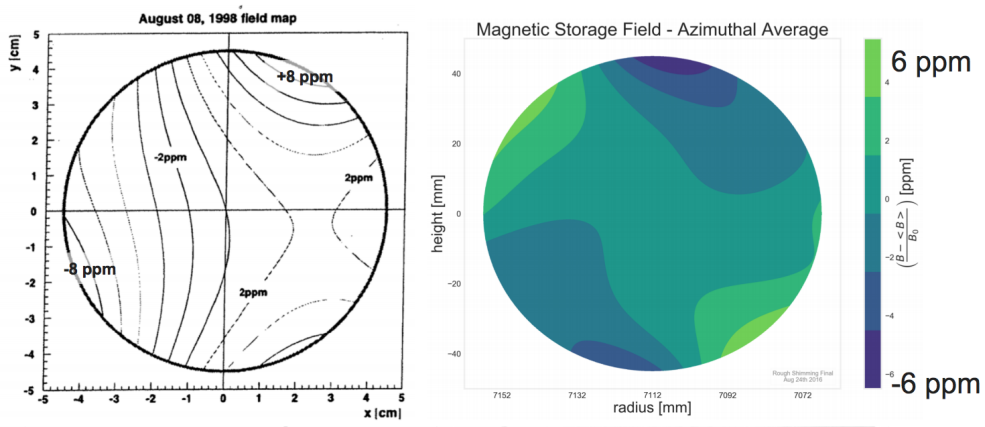

Date	*norm1*	*norm2*	*norm3*	*norm4*	*skew1*	*skew2*	*skew3*	*skew4*
August 08, 1998	7.73	-5.29	-2.79	0.38	-2.07	-0.02	-0.25	0.71
August 24, 2016	0.02	-0.71	0.75	0.44	-0.56	-3.77	0.62	1.61

(a) The azimuthally averaged magnetic field map for the Brookhaven experiment (left) [1] and measured in the Fermilab experiment in August 2016 (right) [67]. The table shows the measurements for the different moments measured in each experiment.

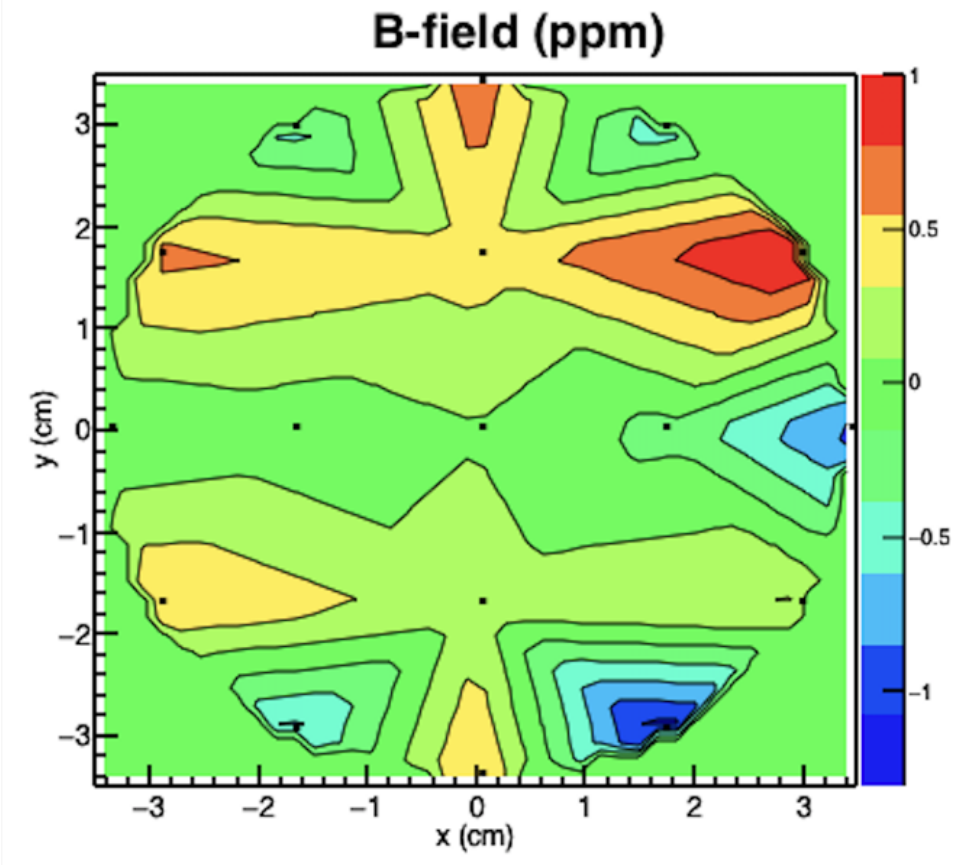

(b) The azimuthally-averaged magnetic field map measured in April 2018.

Figure 31: The azimuthally-averaged magnetic field map for the Brookhaven experiment (top left), the Fermilab experiment in August 2016 (prior to installing the detectors and ring equipment) (top right), and for the Fermilab experiment during experimental running in April 2018 (bottom).

Chapter 5

The Straw Trackers

The construction and testing of the $g-2$ straw tracking detectors will be the focus of the first part of this thesis; the other major focus is the development of software for the extrapolation stage of the track reconstruction software, and its use in performing analysis of the beam dynamics during the beam commissioning phase of the first $g-2$ data taking period. This chapter will explain the physics goals of the tracking detectors, and discuss their design in relation to those goals. The construction and testing methods used for building the trackers and ensuring they met the required specifications will then be described.

5.1 Overview

The basic principle of the tracking detectors is to detect the points at which a decay e^+ passes through a series of tracking 'planes', in order to reconstruct its trajectory between the planes to form a 'track', and then extrapolate the momentum, time and associated uncertainties from the point of entry to the detector back to the muon decay position. The tracks can also be extrapolated forwards from the downstream plane to the face of the calorimeters.

For the first $g-2$ experimental run, which started in October 2017 and will continue until June 2018, the storage ring is equipped with two 'stations' of tracking detectors, located at 180° and 270° around the ring (assuming that the mouth of the inflector, where the μ^+ are injected into the ring, is at 0°). An additional station is ready to be installed during the summer shutdown at Fermilab at the 15° location, ahead of the next major data-taking period.

5.2 Requirements of the tracking detectors

There are three main aims of the straw tracking detectors. The first two are associated with the reduction of significant sources of systematic error on the ω_a measurement; the third relates to the ability of the tracking detectors to search for a muon EDM. The aims are:

- Monitor the muon beam as a function of time throughout the muon fill.

- Isolate time windows with multiple positrons hitting the calorimeter in order to identify pileup events.
- Search for an oscillation in the vertical decay angle of the emitted e^+, in order to determine the presence of any tilt in the precession plane of the μ^+ that would be consistent with the existence of a non-zero muon EDM.

Each of these aims will now be discussed in turn.

5.2.1 Monitoring of stored beam profile

Monitoring the profile of the stored μ^+ beam is the primary function of the tracking detectors, and is important for several reasons. As discussed above, there are several major systematic errors on the measurement of ω_a that are associated with the behaviour of the muon beam. While the fiber harps provide direct measurement of the muon beam profile, their location in the muon beam means that their presence causes levels of multiple scattering that are destructive to the determination of ω_a. The tracking detectors provide an indirect measurement of the beam which is inferred from the trajectories of the emitted decay e^+, so can monitor the beam continuously throughout the entire period of data collection. They are the only system designed to do this. Specific beam properties that can be measured by the trackers include:

- Determination of the momentum spread of the beam.
- Measurement of the amplitude, frequency, phase and lifetime of the CBO.
- Convolution of the spatial distribution of the muon beam with the measured magnetic field to determine the effective field seen by the beam.

Measuring the momentum spread of the beam is important for several reasons. Many features of the beam are momentum-dependent; for example, the muon momentum is correlated with the average orbit radius (high-momentum tracks are expected to come from a higher radius). Additionally, the low-momentum tracks at lower orbit radii will actually have a slightly shorter cyclotron frequency (since they traverse a shorter path) and so will eventually catch up with the higher momentum muons in a process called de-bunching. This causes the so-called ‘fast-rotation’ effect. The tracker measurements of the e^+ momentum can verify other methods of determining the equilibrium radius using the fast rotation analysis by considering the relationship between radius and momentum.

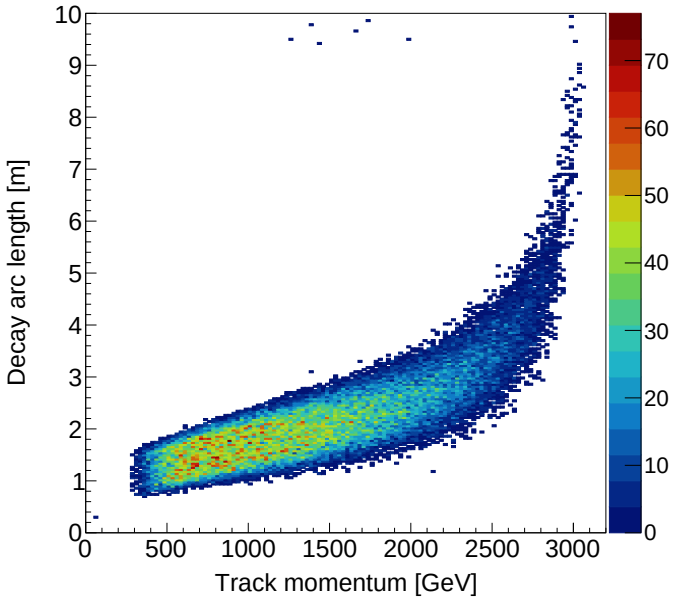

(a)

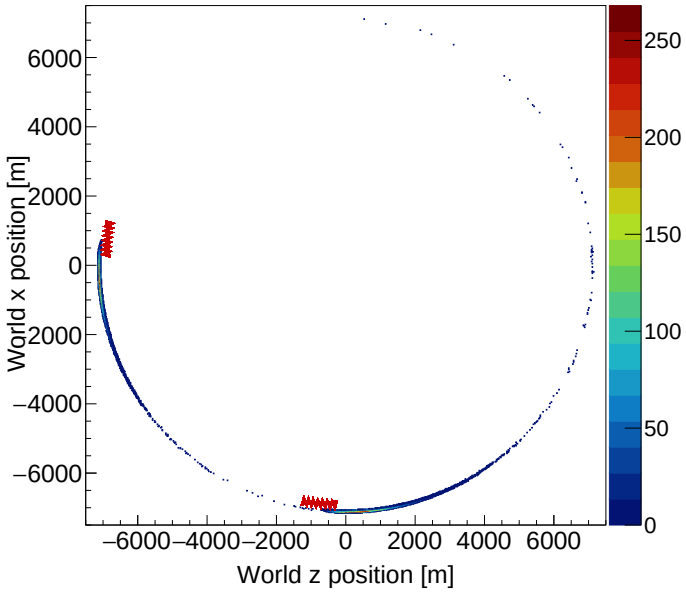

(b)

Figure 32: Simulated plots illustrating the tracker azimuthal acceptance. Figure (a) shows the true decay arc length (from decay position to calorimeter) of the e^+ as a function of momentum. Figure (b) is a top-down view of the SR showing the tracking detector locations (red) and the decay positions of the accepted μ^+.

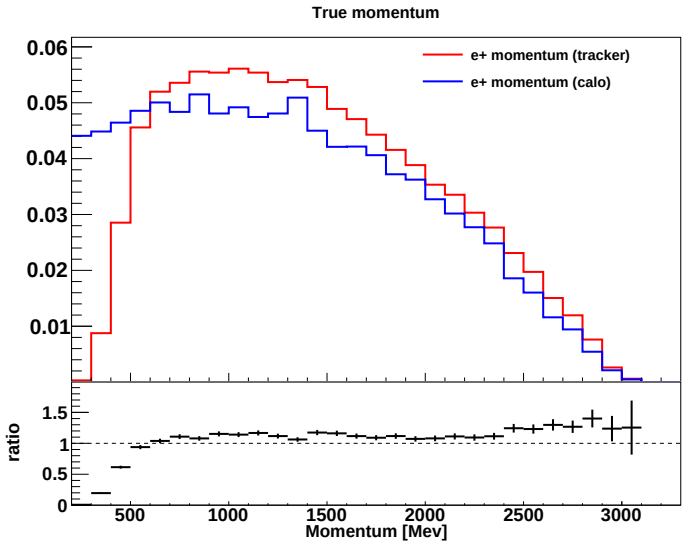

Figure 33: Momentum distributions from simulation showing the true momentum of tracks that hit enough tracking planes to form a track (red) and e^+ that hit a calorimeter (blue). The acceptance of the tracker tails off sharply at 0.5 GeV, but there is good agreement between the distributions for the energy range of interest.

The convolution of the spatial beam distribution with the measured magnetic field map is a very important step in determining a_μ to the desired precision. While the vertical (dipole) magnetic field strength is controlled incredibly precisely, higher-order 'multipole' terms contribute as a function of position in the storage region. These cause slight deviations to the *effective* field seen by the individual muons, which is the field that needs to be known in order to accurately determine a_μ. The beam distribution must be mathematically convoluted with the field map in order to determine the effective field to the required precision. The magnetic field in the SR is described in detail later in this section.

5.2.2 Reduction in calorimeter-related systematic errors on a_μ

In addition to its primary function of studying the muon beam profile, the trackers will provide valuable information to the calorimeters that will help reduce several other sources of systematic error on ω_a. The comparison between detected calorimeter energy and the measurement from the trackers of the momentum of the corresponding calorimeter event can also help with the alignment of the detectors, and to cross-check the calibration of the calorimeter gain as well as its timing.

The major benefit of the tracking detectors to the calorimeter analysis is their ability to isolate time windows containing multiple tracks, which can identify candidate pileup events. Pileup is the name given to events where two or more tracks are incident on the same calorimeter crystal, causing the calorimeter to reconstruct the energy of the event incorrectly; for example, if two e^+ of the same energy entered the same crystal, the calorimeter would reconstruct this event as a single e^+ with twice the energy. It is clear that such events can seriously affect the determination of ω_a from the calorimeter data, since this would effectively cause the calorimeter to miscount the number of positrons.

The ability of the trackers to measure the momentum of the incident particles is another important feature. One major systematic is the presence of muons that did not have the required momentum to remain in the storage region, and so instead slowly spiral into the centre of the ring where they are eventually observed by the detectors. These tend to have higher average momentum than the decay positrons, since the initial spread in momentum of the muon beam is small. This causes them to traverse a path with a lower radius of curvature, and will often have sufficient energy to pass through one or even two calorimeters completely, and so they can be identified as double or triple 'coincidence' events by looking in consecutive calorimeters for events close together in time. Comparing the energy of these events with the momentum of the corresponding tracker event can be a useful way to identify these events and remove them from the analysis. A plot from simulation, comparing the momentum distributions measured by the trackers and calorimeters, is shown in figure 33.

5.2.3 Direct detection of vertical angle oscillation

The trackers measure the momentum of the decay e^+ and propagate its magnitude and direction components back to the most probable decay position of the μ^+. This means that the vertical decay angle of the e^+ can be measured directly using the trackers. As explained in the previous section, an oscillation in the average vertical decay angle as a function of time in the muon fill is a signal of a non-zero muon EDM, since it is indicative of a tilt in the precession plane of the μ^+. The size of the tilt is directly related to the amplitude of the measured vertical oscillation, and is directly proportional to the magnitude of the muon EDM. The ability to directly measure the tilt angle sets this analysis method apart from the calorimeter-based method, which infers the oscillation in the vertical decay angle from a measurement in an up-down asymmetry in the average vertical

position of the detected e^+. The tracking detectors have a much greater sensitivity to the vertical angle than the traceback system used in the Brookhaven experiment, and so this is a major reason, along with the increase in statistics, why the Fermilab $g-2$ experiment is expected to reduce the current limit by two orders of magnitude.

5.3 Tracker design considerations

The design of the straw trackers is motivated by the physics goals described above. In principle, the trackers should have a spatial acceptance that matches the true profile of the beam as closely as possible. The beam aperture is defined by the distance between the quad plates; it is ±4.5 cm in radius both radially and vertically. The straw height should be approximately 10 cm high to ensure maximal vertical acceptance of the beam.

The trackers must have good performance over a large momentum range, and each tracker station must accept decay positrons from an azimuthal distance of up to 10m. A plot showing the azimuthal acceptance as a function of track momentum is shown in figure 32a. The resolution on the radial beam position must be less than 1mm in order to ensure accurate measurement of the CBO amplitude. Placing tracking stations at multiple locations around the ring not only provides redundancy and cross-checking, but is invaluable when tuning the beam and optimising muon storage. This is discussed in detail in chapter 8, where an analysis of the beam parameters using the straw trackers during the beam commissioning phase of the experiment is presented.

The number of planes and their orientation was designed with maximal radial position resolution of the muon beam profile in mind. The requirement on the per-straw resolution to ensure this aim is 300μm. The requirements in the vertical direction are relaxed since the positron track only has radial curvature. There should be as many detector planes as possible in order to reconstruct low-momentum tracks, which will not traverse the full length of the detector and so will need to have as many points on their trajectories recorded in as short a space as possible. To optimise reconstruction of high-momentum tracks, which follow stiffer, longer trajectories, the length of the tracker should fill the space between the two calorimeters to maximise acceptance. Another design constraint is that the tracker should be as close as possible to the muon orbit radius, without placing any dense material in the path of the e^+ that will cause multiple scattering and energy loss on their way to the calorimeters. This is the main reason why gaseous straw tracking

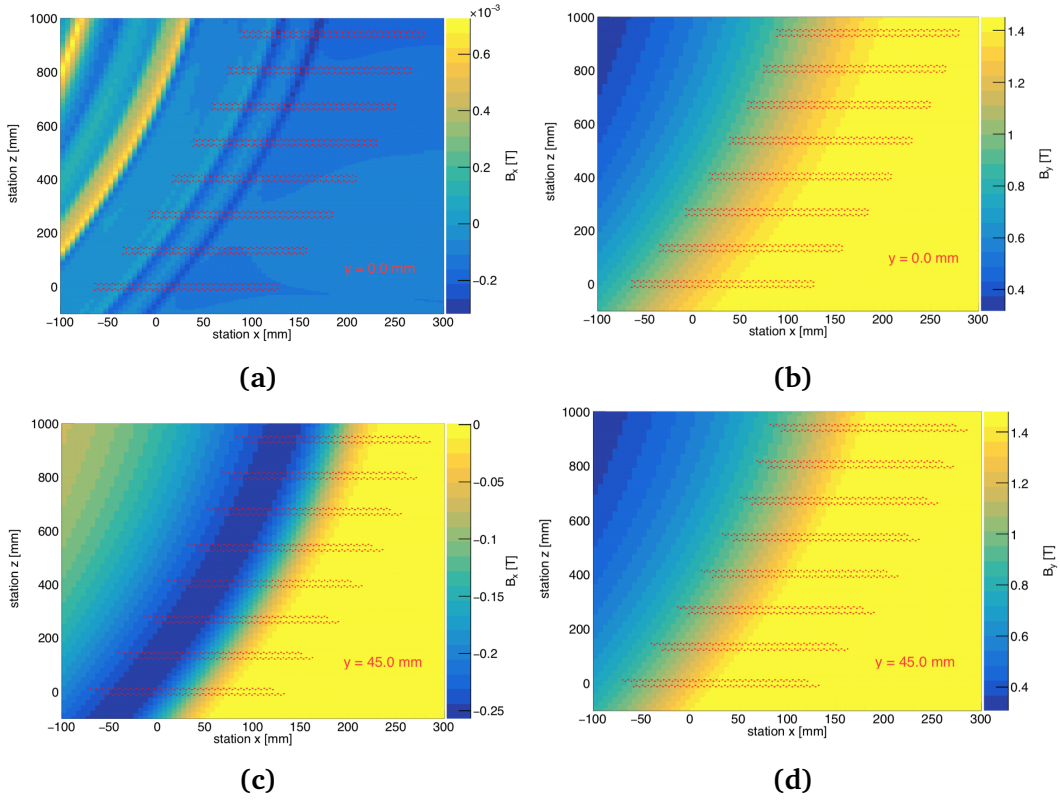

Figure 34: Plots of the magnetic field in the fringe region. All four plots are from a 'top-down' perspective; the red dots indicate the positions of the straws in the detector modules. The more uniform region at the right-hand side of the plots is the storage region where the muon beam is located. Plots (a) and (b) show respectively the radial and vertical components of the field at the mid-plane of the tracking detectors; plots (c) and (d) at a vertical position of +45.0 mm from the mid-plane, at the very top of the straw acceptance region. At the mid-plane (y=0) the radial field varies little and has a low magnitude for most of the region in which the modules are located. The vertical field decreases in strength quickly as distance from the magnetic pole-pieces increases. At the top of the straws, y = +45 mm, the radial field gradient across the module length is much greater than at the mid-plane.

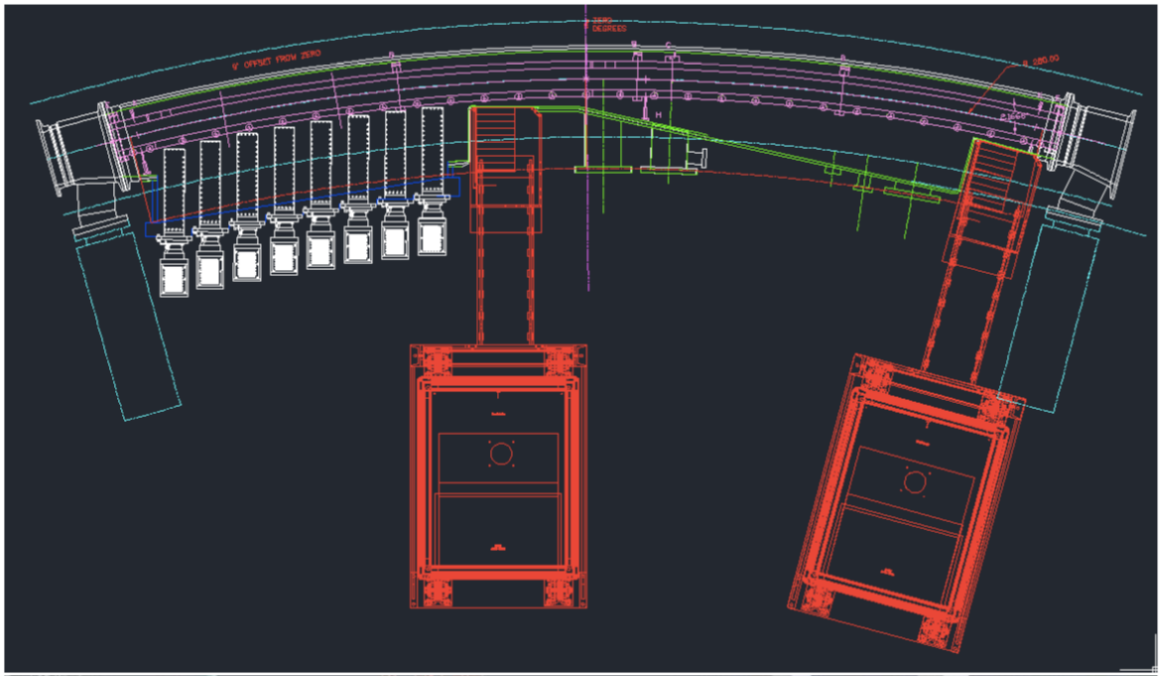

Figure 35: Technical drawing illustrating the location of a tracker station in front of a calorimeter. Image from [13].

detectors were chosen for $g-2$, despite detectors such as silicon trackers having higher resolution capabilities, since such detectors would place too much material in the way of the calorimeters.

The locations of the tracking stations in the SR at 15°, 180° and 270° were chosen so that they would have a clear view of the muon beam, unobstructed by quadrupole plates or collimators from which the e^+ could scatter.

5.4 Principles of detection in straw trackers

This section will describe how the e^+ track creates a signal in the straw detectors that can be converted into a space-point on a track.

Each straw in a tracker module can be considered as an individual drift-tube. The basic principle of detection is as follows: the positively-charged e^+ travels through a drift gas and interacts with the gas molecules as it passes. These interactions occur at random, and the particle leaves a trail of ionisation along its trajectory. During each random interaction with a gas molecule, the e^+ may ionise the molecule, releasing one or more electrons from the atom encountered in the collision.

Such an interaction is termed a primary ionisation, and the electrons released are referred to as a cluster. Secondary ionisations may occur when electrons are ejected from the interaction of a primary electron with a drift gas atom. At the centre of each straw is a thin wire, called a sense wire, across which positive high voltage (HV) is applied. The walls of the straw are electrically grounded and so these act as a cathode, with an electric field directed radially towards it and away from the sense wire (acting as an anode). The radial electric field between the sense wire and the straw walls causes both the ions and electrons liberated from the ionisation to experience a force, causing the electrons to drift towards the positively charged sense wire, and the positive ions to drift slowly towards the straw walls. As the electrons drift towards the wire, they interact with other gas atoms, causing them to decelerate. The net drift of charge across the straw induces a signal in the sense wire.

In the absence of a magnetic field, the electrons will drift in a straight line radially towards the sense wire. However, the path of the drift electrons will be modified if the straw is in the region of a magnetic field. The drifting electrons will experience a Lorentz force, causing it to follow a curved path. The magnetic field in the region of the $g-2$ straw trackers is mostly in the direction perpendicular to the radial electric field in the straw; there is a small radial component that varies along the length and width of the tracking detector region, as can be seen in figure 34. This varying field is significant over the distance of the full station of 8 modules, and must be carefully accounted for when grouping straw hits in separate modules into a track. However, the field is largely constant for an individual straw. If the magnetic field is perpendicular to the electric field, the trajectory of the drift electron is shifted by the Lorentz angle, and there is a resulting spread in the arrival times of the electrons associated with the uncertainty created by this angular shift. The Lorentz angle is proportional to the drift time since an electron with a larger drift time will experience the magnetic field for a longer time. Since the magnetic field strength is necessarily very high, the angle cannot be reduced by minimising B. The effect can be mitigated, however, by choosing a gas with a high density, which is inversely proportional to drift time [69].

The signal induced in the sense wire by the drift of primary electrons from the ionisation reactions between the positron and the drift gas atoms is small, and almost impossible to distinguish from the background noise signals caused by the random motion of particles in the gas. However, the

electric field strength in the straw increases as a function of $\frac{1}{r}$ where r is the distance to the sense wire. As the drift electrons approach the sense wire, they are accelerated between collisions with gas atoms enough to undergo further ionisation reactions with subsequent atoms they encounter. The electrons liberated from these ionisations are also accelerated in the strong electric field, and go on to ionise further atoms still. This causes an effect known as 'avalanche', where very many subsequent ionisations occur close to the wire. This causes an amplification of the signal induced in the wire by the net drift of charge in the straw. The amplification factor of the original signal is roughly proportional to the number of primary ionisations, and so drift chambers that operate in this way are termed 'proportional counters'.

The ions produced in the avalanche interactions drift towards the straw walls, just like the primary ions. Since they are produced very close to the wire at the centre of the straw, they travel a long distance to the wall and hence induce a large signal in the sense wire - much larger than that produced by the avalanche electrons. However, the large ions are relatively slow moving and so have much larger drift-times than the light, fast electrons, and so the signal is delayed relative to the electron signal. This signal is called the ion tail, and it can arrive up to μs after the electron signal. The fast electron signal triggers the electronics, which then suppress the large signal from the ion tail, such that signals from charged particles passing through the straw a short time after the first signal can also be recorded without being affected by the previous ion signal. This feature of the electronics allows the readout to cope with a high rate of particles entering the detector.

As well as producing electrons, the ionisations in the avalanche can produce photons, in a similar proportion to the electrons due to the comparable magnitudes of their cross-sections [69]. Some of these photons will have sufficient energy to cause further ionisations in the gas. Furthermore, photons may have a longer mean-free-path than the electrons, meaning that they can travel beyond the electron avalanche region before causing their own ionisations. In this case, the electrons they produce may cause their own avalanches, and the affect continues causing what is known as the 'breakdown' of the gas. To avoid this, a so-called 'quench gas' is added to the drift gas, which can absorb the photons before they can start new avalanches. A good quench gas should have many modes of excitation such that it can absorb photons in as many ways as possible; organic molecular gases are good candidates. The choice of quench gas for the $g-2$ detectors is discussed later in this chapter.

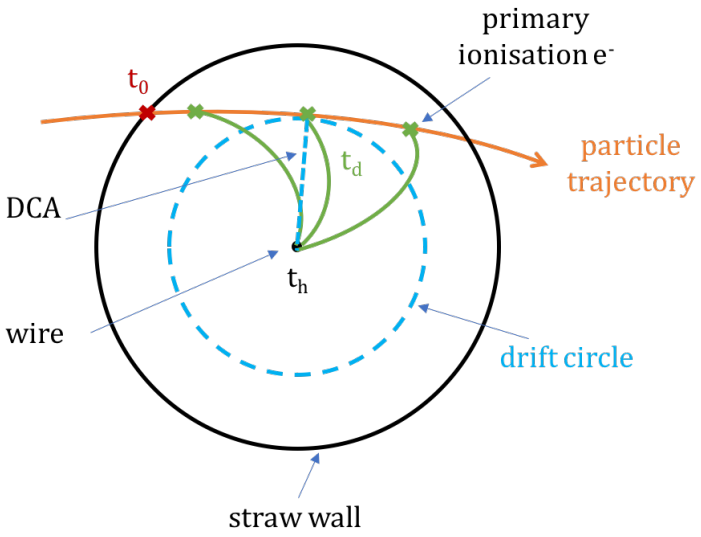

Figure 36: Diagram illustrating the determination of the drift time t_d from the time the particle entered the straw, t_0, and the hit time t_h, the time when the signal from the primary ionisation e^- reached the sense wire.

The signal that is measured is the time when the electron-induced sense-wire signal is large enough to cross some threshold and trigger a 'hit' in the readout electronics. Further information about the time of the hit can be obtained in order to infer a more precise measurement of the trajectory of the positron. The hit time of the track is defined as:

$$t_h = t_0 + t_d \ . \tag{5.65}$$

where t_0 is the time that the particle entered the straw, and t_d, the drift time, is the time that it took the ionisation electrons to drift from the primary interaction point to the wire and cause an avalanche sufficient to trigger the readout. The drift time can be extracted from the hit time t_h if t_0 is known. The drift time can be converted into a distance, referred to as the Distance of Closest Approach, or DCA, from the wire to the primary ionisation point. This is an ambiguous, directionless distance, and so the DCA refers to the radius of a so-called 'drift circle', where the primary ionisation could have occurred at any point on the circumference of the circle. This is illustrated in figures 36 and 37. The DCA is also ambiguous in the vertical direction, so the drift circle actually defines the boundary of a drift cylinder around the wire for the entire length of

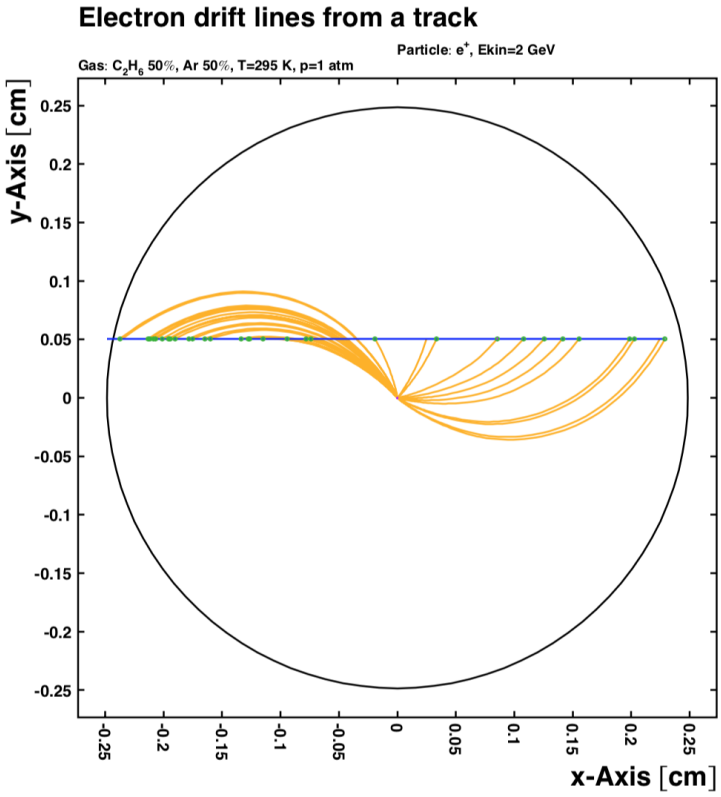

Figure 37: A diagram from GARFIELD [70] illustrating a track passing through a straw. The blue line represents the positron track, which ionises the drift gas atoms in the straw. The ionisation clusters are illustrated in green; the drift lines of the electrons produced in the ionisation are illustrated in yellow. The drift electrons traverse a curved path (due to the magnetic field) to the HV wire in the centre of the straw, and the ions drift to the grounded straw walls. The net drift of charge across the straw induces a signal on the HV wire.

the straw. The ambiguity is resolved by combining this cylinder with the drift cylinders of other straws hit by the e^+. The planes of straws in the detectors are oriented at different angles to allow the vertical position to be resolved; the detector design is discussed in the next section.

5.5 Tracker construction

5.5.1 Straw design

The straws for the $g-2$ detectors are made from two layers of mylar, wound in a spiral, with an outer diameter (O.D.) of 5 mm. The mylar is coated in a layer of aluminuium which reduces the permeation rate of gas through the straw walls, and also provides a shielding layer. The inner wall of the straw is coated with a thin (200µm) layer of gold to allow the inner wall to act as a cathode. Two batches of straws were used in the production of the tracking detectors; the batches

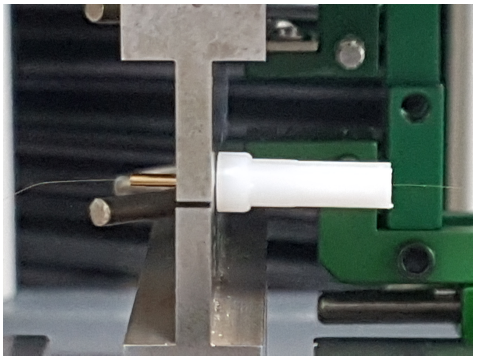

(a) The machine crimping tool for the 'long' pins.

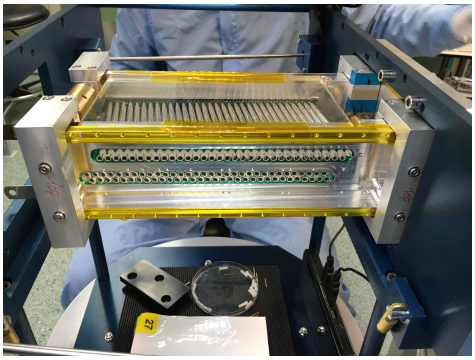

(b) A module in the stringing jig.

Figure 38: Photos of the wire crimping procedures. The 25 µm wire is threaded into the 'long' pin that connects to the ASDQs prior to insertion in the module. The pin is 'crimped' onto the wire by applying a force of 1kN to the pin which is seated in a gap between two plates. The plates are machined such that the gap is a fixed depth, ensuring uniform crimping across all pins. The wire is then threaded into the module, and held in place by a short pin that does not connect to any electronics. This pin is crimped in place using a custom-built crimp tool while the module is mounted in a stringing jig.

differed slightly in wall thickness, due to a thinner glue layer between the mylar layers, resulting in slightly different inner diameters (I.D.). To avoid any undesirable complications associated with using straws of different geometry within a single detector (the drift due to a traversing e^+ will be slightly different in a straw with a smaller I.D. compared to the drift in a larger straw), all straws for a single tracking station came from the same batch. The first batch (batch 1) were used to produce the first tracking station (located at 270° from the inflector exit), and the batch 2 straws were used for the other two stations at 15° (not currently installed in the SR) and 180°. The batch 1 straws had a wall thickness of 15µm and the batch 2 straws had a wall thickness of 12µm. This affected the relative permeation rates of gas from the straws. The testing of the straw leak rates is discussed in detail in chapter 6.

The straws (shown in figure 39) have a length of 10 mm and are active over the full length. At either end of the straw, an aluminium end-pice is glued in using conductive silver epoxy. At the centre of each wire is a 25 µm wire, which is made from gold-plated tungsten. The wire is held in place by two gold crimp pins at either end, which are inserted into injection-moulded plastic endpieces that are slotted into the aluminium straw end-pieces. The plastic end pieces have channels on either side to enable gas to flow freely through the straw. The wire is tensioned

to 30-50 g before being crimped in place, to ensure the removal of any kinks or bends in the wire which could cause discharges or sparks. Crimping was chosen as the mechanism for holding the wires in place since it allowed maximal control over the location of the wire in the straw, which must be located at the very centre of the straw in order to achieve the required resolution on the per-straw position measurement. The plastic end pieces into which the crimp pins are embedded are not glued in place, allowing an individual wire to be removed and replaced if damaged. This is one reason why straw tubes were chosen as the design for the tracking detector rather than a multi-wire chamber, in which damage to an individual wire has a high chance of causing damage to neighbouring wires. Some stages of the tracker construction at Liverpool are shown in figure 38.

5.5.2 Tracker module design

Each tracker station consists of 8 tracker 'modules'; one of these is depicted in figure 40, and a diagram of a full tracking station shown in figure 35. Each module consists of 4 layers of 32 straws each, grouped into two pairs of layers called 'views'. In one view, both layers of straws are oriented at a stereoangle of $+7.5°$ away from the vertical, and the straws in the other view are angled at -7.5°. The first view is referred to as the 'U' view and the second as the 'V' view. Having two views at different angles enables the vertical height at which the track entered the module to be resolved. The position reconstruction process is discussed later in this section and is illustrated in figure 46.

The straws are inserted into the module by being glued into two aluminium manifolds using a combination of silver epoxy, to ensure a good ground connection between the straw and the module, and structural epoxy to provide a good gas seal between the outside of the straw and the manifold. The gold pins that hold the sense wire in place are connected to the electronics boards housed inside the manifolds - these are described below. The manifolds are seated in an aluminium flange which bolts into the vacuum chamber. On the other end of the flange are two 'snouts' which connect the manifolds to the crate that houses the back-end readout electronics.

After the straws have been inserted into the manifolds, and before the electronics are installed, the manifolds are pulled apart slightly using a jack in order to apply tension to the straws. This removes any kinks or creases in the straw walls such that every individual drift tube has a constant

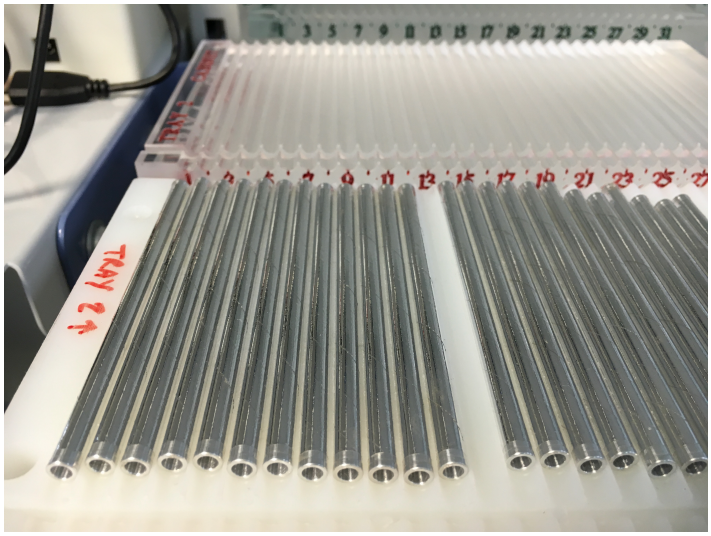

Figure 39: The straws for one manifold with their Al end-pieces glued in.

radius, and there are no sharp points which could cause discharges. The tension must be applied very carefully in order not to damage the straws or introduce small holes from which gas could leak into the Storage Ring Vacuum (SRV). At the inner edge (closest to the beam) of the straw module is a 5mm diameter carbon fiber post, which supports the manifolds and ensures that they remain a fixed distance apart for the entire length of the module, such that the tension across every straw and wire is constant. The post is made from carbon fiber as this has a comparatively high strength-to-density ratio. This is important as the location of the post at the end of the module places it in direct sight of the positron trajectory on the way to the calorimeter. If the post were made from a dense material, the e^+ could undergo energy loss, causing inaccurate reconstruction in the calorimeter. e^+ that pass through the carbon fiber post may also undergo multiple scattering, which causes them to deviate from their original trajectories. This means that e^+ which pass through the post and then go through enough straw layers to form a track will be extrapolated to an incorrect muon decay position. The fraction of straw tracker events that hit the post, and other solid material such as the walls of the vacuum chamber, was studied extensively in simulation; this is discussed in detail in chapter 7.

5.5.3 Gas choice

The choice of gas for a drift chamber is motivated by several, occasionally conflicting, requirements. Avalanche multiplication occurs in all gases, but in noble gases such as argon, avalanche multiplication occurs at much lower fields than in complex molecules, since the only mode of energy

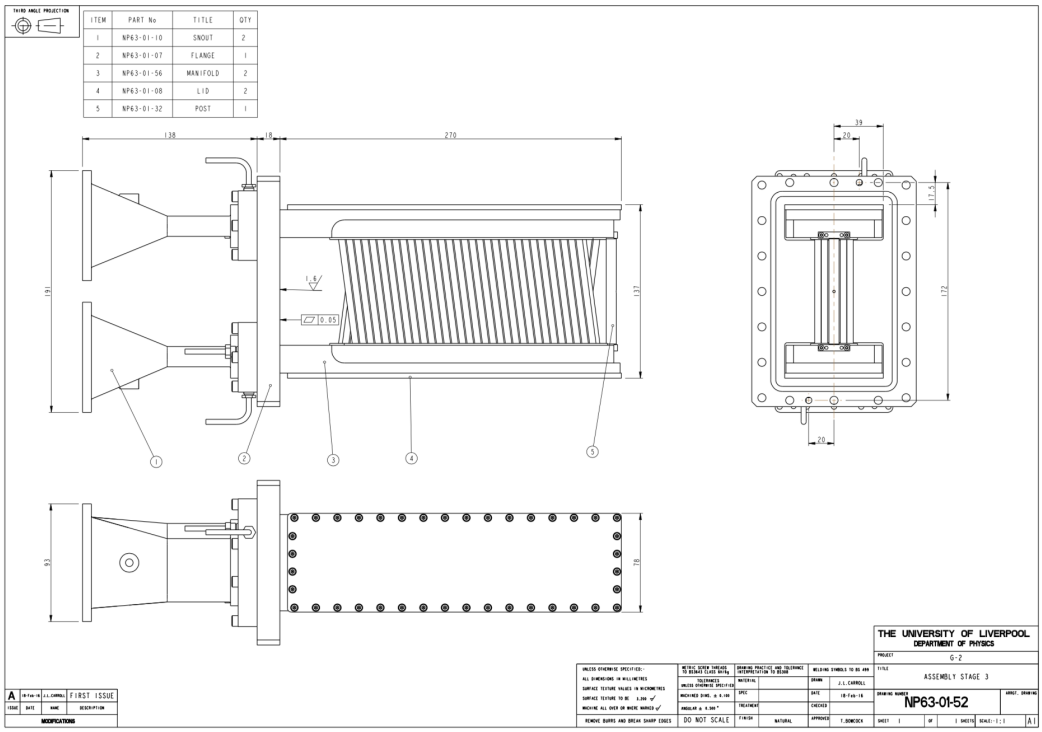

(a)

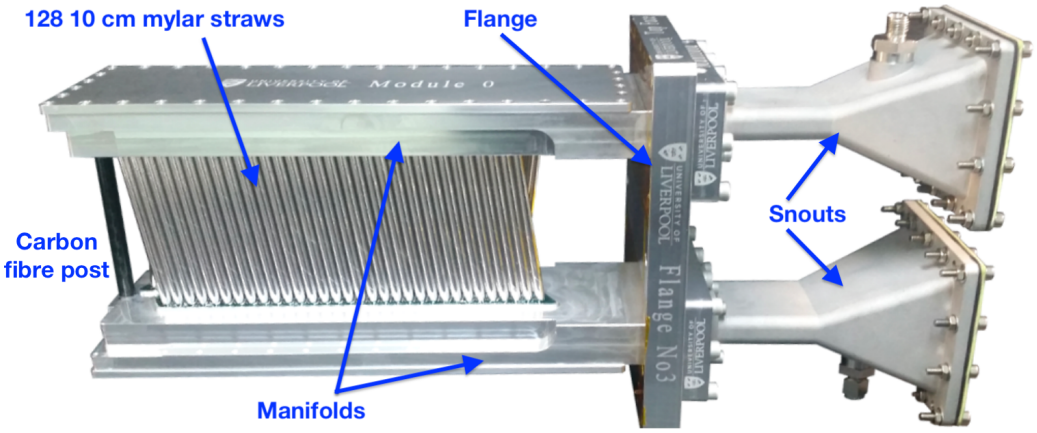

(b)

Figure 40: The technical diagram of a tracker module (a) and a picture of a completed module (b).

dissipation in a noble gas is ionisation. Being relatively abundant and cheap compared to other noble gases, argon is a good choice of drift gas. However, argon is unable to absorb energy without returning to the ground state and releasing a photon, whose minimum energy is well above the ionisation potential of any metal likely to be used for the cathode, and so ionisation photons can liberate photoelectrons from the cathode which can go on to induce further avalanches in the gas [71]. This means that it is not possible to achieve gains above $\sim 10^4$ with argon alone, since the multiple ways in which spurious avalanches can be induced cause the gas to enter permanent discharge, or breakdown, quickly. The addition of a so-called 'quench gas' to the argon can prevent breakdown, however, and allow the argon based detector to reach higher gains while remaining in proportional counter mode. Polyatomic molecules tend to have a large number of non-radiative excited states, and as such they can absorb the emitted photons without radiating new ones. A molecule with many rotational and vibrational modes can absorb photons of a high energy range, making them natural partners for a drift gas like argon. Organic compounds such as hydrocarbons and certain alcohols exhibit this behaviour, as do some inorganic compounds like CO_2. Adding even a small amount of a quench gas to argon can help the detector achieve gains of up to 10^6.

In addition to gain considerations, a gas mixture with well-understood drift behaviour is required, since the drift-times are used to determine the position at which the e^+ travelled through the straw; a precise understanding of the drift-time to radius relationship is thus essential. The drift time of the electrons to the sense wire is determined largely by its probability of collisions with gas molecules along the way, which slows them down, in combination with the acceleration they experience as they enter an increasingly strong electric field region as they approach the wire. Complex quantum-mechanical effects, such as the Ramsauer effect, introduce a dependence of the collision cross-section on electron energy, and so their likelihood of collision and rate of deceleration varies with changing electric field strength. To further complicate this, the addition of even small amounts of different gases can dramatically alter this behaviour [71]. The behaviour of different gas mixtures has been extensively studied [69, 71], and so a well studied gas can be chosen for the $g-2$ detectors. In particular, it is desirable to select a gas mixture where the acceleration of electrons close to the wire is largely cancelled by collision probability effects, resulting in a drift velocity that is almost constant throughout the straw. This is referred to as 'saturated drift velocity', and is achieved at a velocity of ~ 5 cm/μs for a typical argon-hydrocarbon mixture [69].

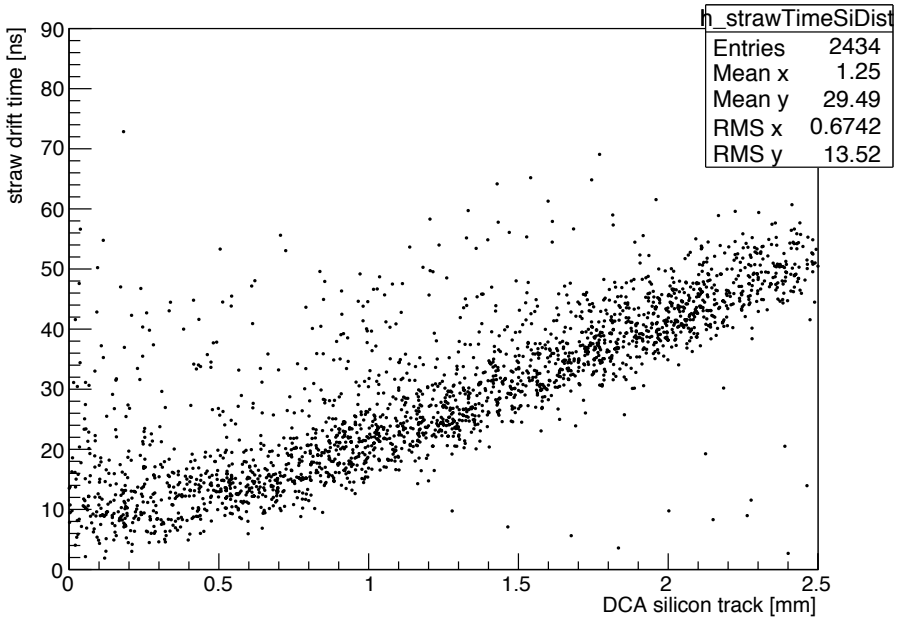

Figure 41: The drift-time to distance relationship in the straws, measured at the 2015 test beam by comparing signals in the tracker module to the well-known track position measured using a silicon telescope. [72].

5.6 Tests of the tracking detector performance

In June 2015, a prototype tracking detector module was tested at the Fermilab Test Beam Facility (FTBF). A beam of 3 GeV/c protons was used to test the performance of the detector with different HV settings and with different gas mixtures. The module was tested at both 1500V and 1800V, with the gas mixtures 80:20 Ar:CO_2 and 50:50 Ar:C_2H_6. Four layers of silicon, together referred to as a silicon telescope, were used to measure the position of the track to high precision. Two layers were located upstream of the straw tracker, and two layers downstream. This allowed the signals detected in the straw tracker to be compared to a very well known track, reconstructed between the silicon telescope layers. The high-momentum protons followed very straight trajectories since no magnetic field was present for this test. The straw drift time as a function of distance between the wire (where the signal is recorded) and the position at which the track traversed the straw (measured using the silicon telescope) is illustrated in figure 41. The test beam results are documented fully in [72].

5.7 Readout electronics

After a signal is detected on the sense-wire, the data flows through a complex suite of electronics which convert the analog straw signal into a digital hit that is suitable for use in the track reconstruction software. The data path will be described in the following section. The readout system for the straw trackers was designed by the UCL and Boston University teams, and is fully documented in [72].

The readout system includes 'frontend' processing, which refers to the boards used to detect the sense wire signals and convert these to straw hits, and 'backend' boards which interface with the frontend boards and synchronise the data from the numerous channels using the experimental clock information. The frontend electronics contain two different types of boards: the Amplifier Shaper Discriminator with charge (q) encoding (ASDQ) board and the Time to Digital Converter (TDC) board. The ASDQs are housed in the manifolds of the straw modules and are the first board encountered by the signal from the sense wire. When a charged particle enters the straw and creates a signal on the wire, the ASDQ records the time that the particle traversed the straw by triggering a 'hit' if the signal crosses a threshold. The boards also contain HV connectors to supply HV to the sense wires. The gold pin that holds the sense wire in place in the straw is connected directly to the ASDQ board. Each ASDQ board connects to 16 straws. There are four ASDQs in each manifold; the four in the 'top' manifold connect to straws in the 'U' view and the straws in the 'bottom' manifold connect to straws in the 'V' view.

The signal induced on the sense wire undergoes amplification, signal shaping and threshold discrimination in the ASDQ board. The process of signal shaping is illustrated in figure 43. The multiple avalanche signals from a particular track passing through the straw are integrated into a single, smooth pulse, which can then be interpreted by a discriminator that determines if the pulse passes the threshold for a hit. The shaping includes the cancelling-out of the large, slow signal due to the ion tail that follows the signal from the drift electron avalanches. Cancelling out the ion tail signal prevents it from overlapping with subsequent primary signals due to electron avalanches from other charged particles entering the straw. The leading and trailing edges of a shaped pulse that passes the discriminator threshold are recorded by the ASDQ as a digital straw hit.

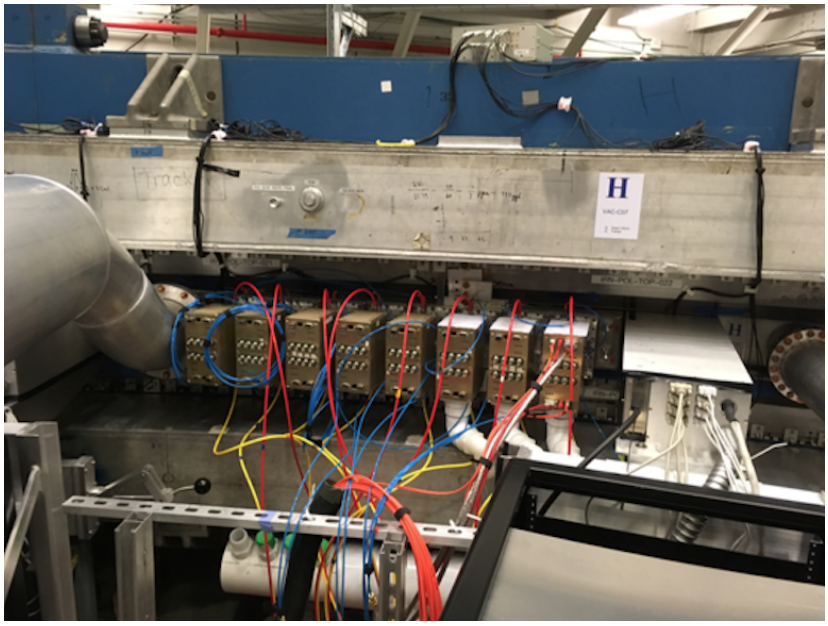

Figure 42: The 8 FLOBBERs of one tracker station installed in the SR.

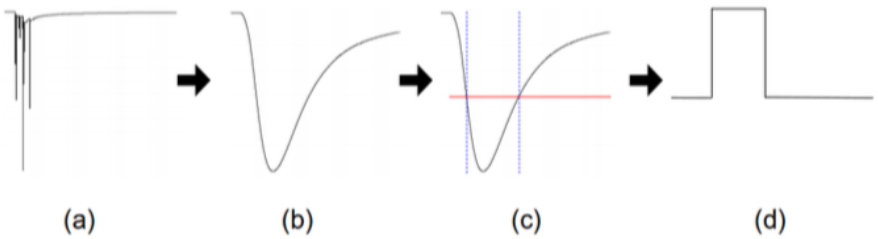

Figure 43: The diagram illustrates the shaping of the sense wire signal in an ASDQ. In part (a), a series of short, sharp signals are detected from the successive electron avalanches caused by the primary ionisations from a charged particle travelling through the drift gas of a straw. In part (b), the signal is amplified and shaped into a smooth pulse by the ASDQ. In part (c), the red line illustrates the threshold imposed by the discriminator, and the blue lines illustrate the two points at which the pulse shape crosses the threshold. Part (d) shows the digital pulse that is communicated from the ASDQ to the TDC. The two transitions of the digital pulse represent the times of the leading and trailing edges of the shaped pulse. The ion tail is not included in this diagram. [72]

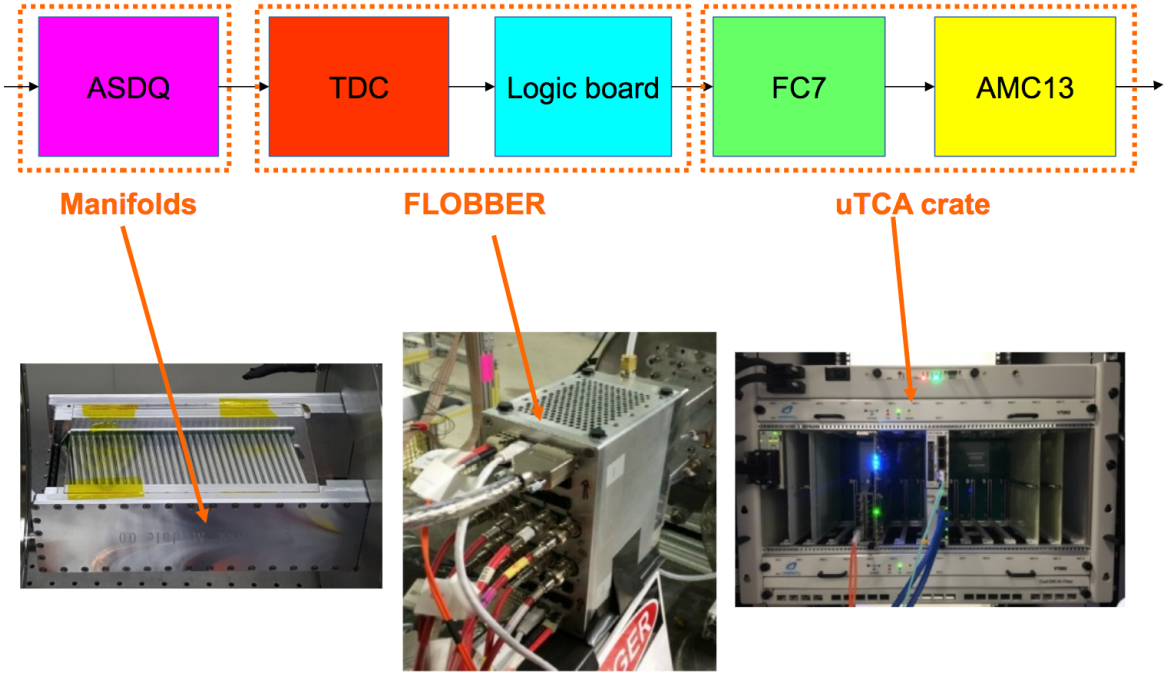

Figure 44: Schematic diagram illustrating the data path from the sense wire signal in a straw to straw hit information that can be used in software [72].

The digital information from the ASDQ is communicated to a TDC via a flexicable, which travels from the ASDQ in the manifold via a 'snout' to the FLOBBER (Frontend Low-Voltage Optical Box to BackEnd Readout) (shown in figure 42), which is a custom-designed crate that attaches to the straw module and houses the TDCs, HV boards and logic boards (LBs). These boards must be close to the straw modules to minimise signal transition lengths, but do not need to be directly connected to the straws like the ASDQs. The boards are hence mounted outside the vacuum chamber for ease of access and cooling, with the additional benefit that there is less material within the SRV volume.

Each TDC board connects to one ASDQ board and processes the data from 16 straw channels. The TDC is connected to the experiment's external 40 MHz clock. The role of the board is to time-stamp the ASDQ signal with a precision of 625 ps, and communicate the leading-edge of the signal as the straw hit time to the downstream data processing systems.

The time-stamped signals from four TDCs are passed to a logic board (LB), whose general purpose is to combine the signals from the TDCs into a single data-block that can be passed onto the downstream data processing in response to a trigger command. A fiber-optic cable connects each

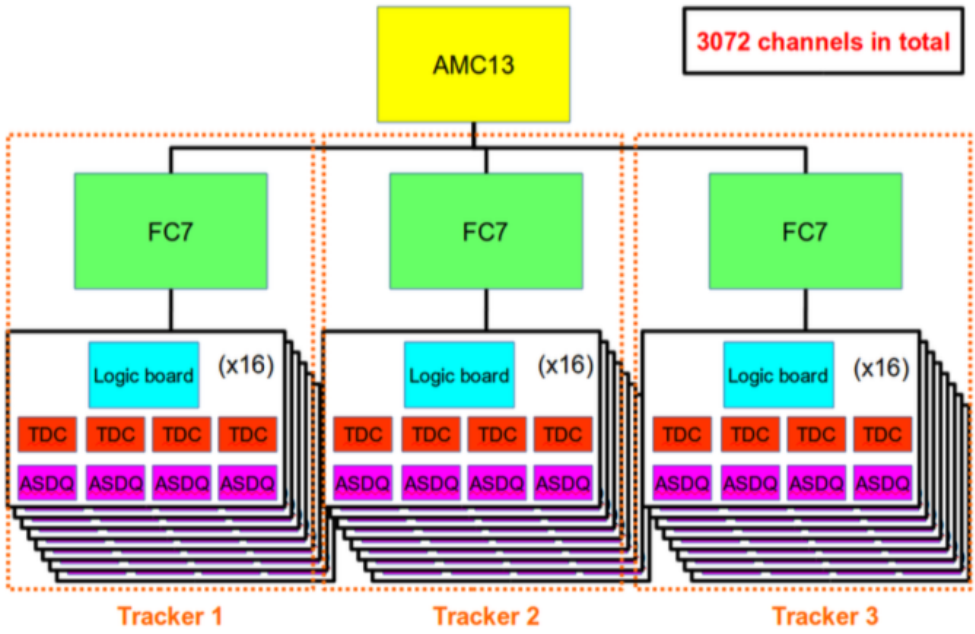

Figure 45: Diagram illustrating the structure of the frontend (ASDQ, TDC) and backend (LB, FC7 and AMC13) boards and the number of each board used in the readout system [72].

LB to the higher-level backend boards in order to receive the external clock and control signals and transmit the data from the TDC. A fiber-optic cable is used as this allows data to be sent quickly over a large distance. This is required since the higher-level backend boards contain magnetic components, and must therefore be situated on a rack in the centre of the SR at a sufficient distance to ensure no perturbation to the magnetic field in the storage region. The clock and control signals are sent to each TDC from the LB, and an event-builder in the LB firmware combines all the data from all TDCs into a single event that can be communicated downstream to the FC7 and AMC13 boards.

The FC7 and AMC13 boards are housed in a microTCA crate, located on a rack away from the storage region. There is a similar relationship between these boards and the LBs connected to it as there is between an individual LB and its corresponding TDCs; the FC7 aggregates the data from multiple LBs into a single data-block using an event-builder in the firmware. Each FC7 communicates with one tracker station, so there are three FC7s in total for the experiment; a single AMC13 unifies the data from the three FC7s in order to provide a single interface with the clock, control and tracker data acquisition (DAQ) system. The use of a microTCA crate and AMC13 board for high-level data communication is common to all systems in the $g-2$ experiment; this

allows the same software to be used for tasks such as data unpacking and slow control monitoring. The data chain is illustrated pictorially in figures 44 and 45.

5.8 Track formation

The diagrams in figure 46 illustrate the process for reconstructing the 2D hit position in a straw module. The first part illustrates a track passing through neighbouring straws in the layers of a tracker module. In an individual straw, the DCA of the track to the wire defines the radius of a drift cylinder which defines a surface containing all the possible points at which the track could have traversed the straw, based on the drift-time information from that straw alone. By grouping the drift cylinders from two neighbouring straws in a particular view, the number of ambiguous hit positions is reduced; instead of the possible positions lying on the surface of a cylinder, a vertical line is defined in the plane of that view. The intersection of lines in neighbouring views – oriented at ± 7.5° stereoangles – provides the 2D hit position for the track in that module.

After the 2D positions have been obtained, a fitting algorithm is used to connect the positions in all the modules of a tracking station that recorded hits. The track fitting provides the position, momentum and associated uncertainties in the form of a covariance matrix at the entrance and exit of the tracker station. These parameters are then extrapolated back to the muon decay point. This extrapolation process is covered in detail in chapter 7.

5.9 Summary

The tracking detector modules were built at the University of Liverpool and transported to Fermilab for pre-installation testing. Tests of the tracker performance were performed using radioactive sources to measure the detector response in each channel. In addition to these electrical tests, the vacuum performance of each module was measured both at Fermilab and in Liverpool. The vacuum tests are described in the next chapter.

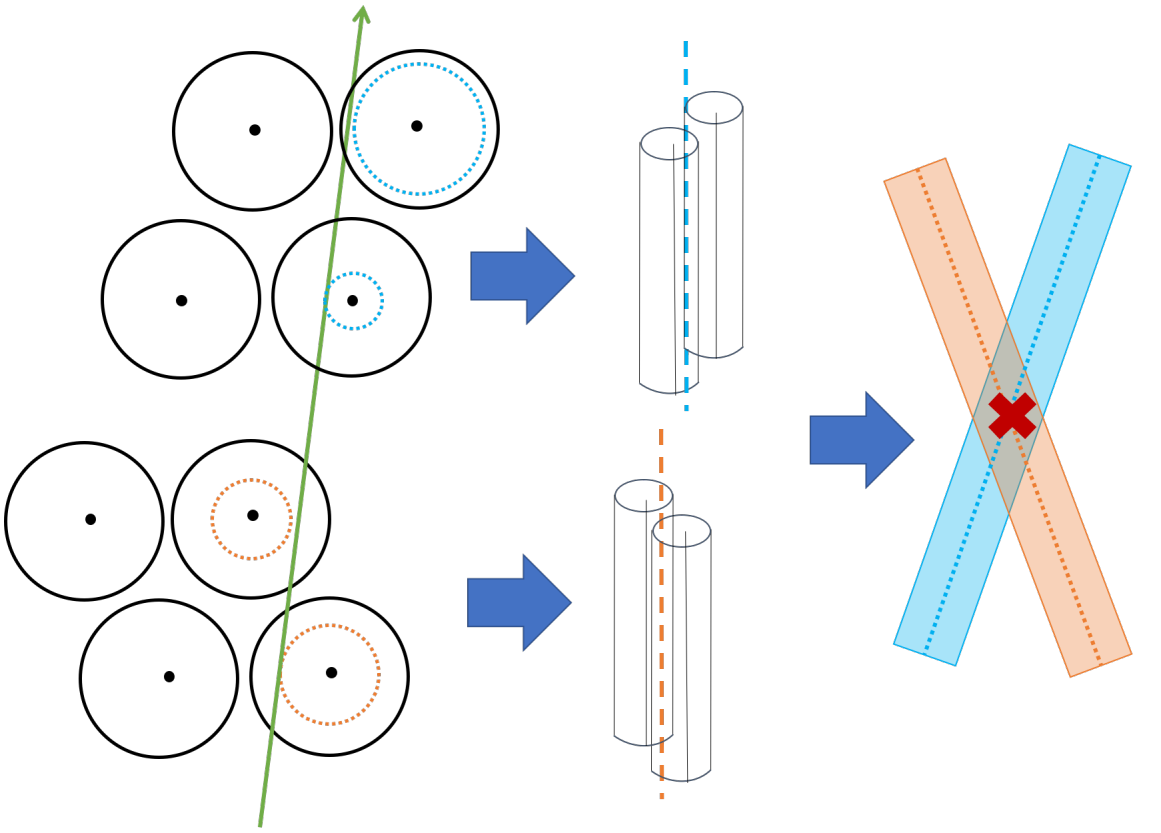

Figure 46: Diagrams illustrating the 2D position reconstruction process.

Chapter 6

Testing the tracker vacuum performance

6.1 Vacuum requirements of the tracker modules

In order for the electrostatic quadrupoles (ESQ) to achieve their intended voltage and to minimise the risk of sparks, the Storage Ring Vacuum (SRV) pressure must not exceed 1×10^{-6} Torr at the quad stations. Mylar is permeable to certain gases [73], so it was known at the time of design that there would be some non-negligible permeation of the straw gas into the SRV; the leak rate of the tracker modules must be low enough to be entirely mitigated by the pumping capabilities of the SRV system.

It was required that the per-tracker leak rate should not exceed 4.5×10^{-5} Torr·L/s; this corresponds to a per-module leak rate upper limit of 5.6×10^{-6} Torr·L/s, to ensure the SRV would be at a low enough vacuum pressure to ensure optimal performance of the ESQ. In the worst-case scenario, the per-tracker leak rate *must* not exceed 1.2×10^{-4} Torr·L/s, corresponding to a per-module worst-case upper limit of 1.5×10^{-5} Torr·L/s.

The leak rate of every straw to be used in the tracker modules was measured prior to installation in a tracker module. The rate at which the pressure increased after switching off the vacuum pumps, known as the 'rate of rise' (RoR), was measured for each module after production to ensure it met the vacuum specifications before being installed in the SR. This chapter describes the straw leak testing system and quality assurance procedure, as well as the results from the full suite of leak rate and performance tests performed on the tracker modules prior to their installation in the storage ring. Finally, the results from vacuum tests performed on the SRV after the tracker installation will be presented.

6.2 Straw leak tests

Every full length (130 cm) straw to be used was leak tested prior to being cut to length for use in the tracker modules. The target upper limit for the per-module leak rate means that the average full-length straw leak rate should not exceed 7×10^{-7} Torr·L/s, or 5.6×10^{-5} ccm[4].

At the time of setting up the leak tests, the choice of drift gas was still under discussion, but the most likely choice was a 50:50 mixture of Ar:C_2H_6. The leak tests were designed to be performed using CO_2, and could not be adapted to use an ethane sensor instead for safety reasons. The leak rates were measured using 50:50 Ar:CO_2 and quoted for that ratio so that the number could be easily compared to the 50:50 Ar:C_2H_6 leak rate. (The leak rate of Ar is negligible compared to that of CO_2 [73]). During the testing procedure, the test gas was switched to pure CO_2. The leak rates were converted from the measured 100% CO_2 leak rate to the leak rate for 50:50 Ar:CO_2 to allow straightforward comparison with the previously measured 50:50 Ar:CO_2 values. All straw leak rates presented in this section are quoted for 50:50 Ar:CO_2.

6.2.1 Leak testing chamber design

The straw leak testing procedure at Liverpool uses two identical leak testing chambers (figure 47a), originally designed for the mu2e experiment. A leak testing chamber consists of two copper tubes of approximately 1.5 m in length, connected at one end by an electronics box which contains a fan to ensure gas circulation around the chamber, and at the other by a small bridging tube. A diagram of the chambers is shown in figure 47b. There are two bidirectional valves in the chamber. One connects the chamber to the gas line, and the other is used to switch the chamber between the 'open' configuration (where the gas flows from the inlet around both pipes of the chamber and is then exhausted after a single circuit) and the 'closed' configuration (where the chamber is sealed at both ends and the fan blows the gas around the entire volume).

An EE891 CO_2 sensor module [74] is housed alongside the fan in the electronics box at the end of the chamber. The sensor has a measurement range of 0 - 2000 ppm with an uncertainty of ±50 ppm +2% of the measurement value at room temperature. The CO_2 is detected via the Non-Dispersive Infrared Technology (NDIR) measurement principle. The measurements are read

[4]The straw leak testing equipment procedure measures the straw leak rates in ccm, while it is more intuitive to discuss the vacuum pressure in terms of Torr·L/s. 1 ccm = 0.025 Torr·L/s.

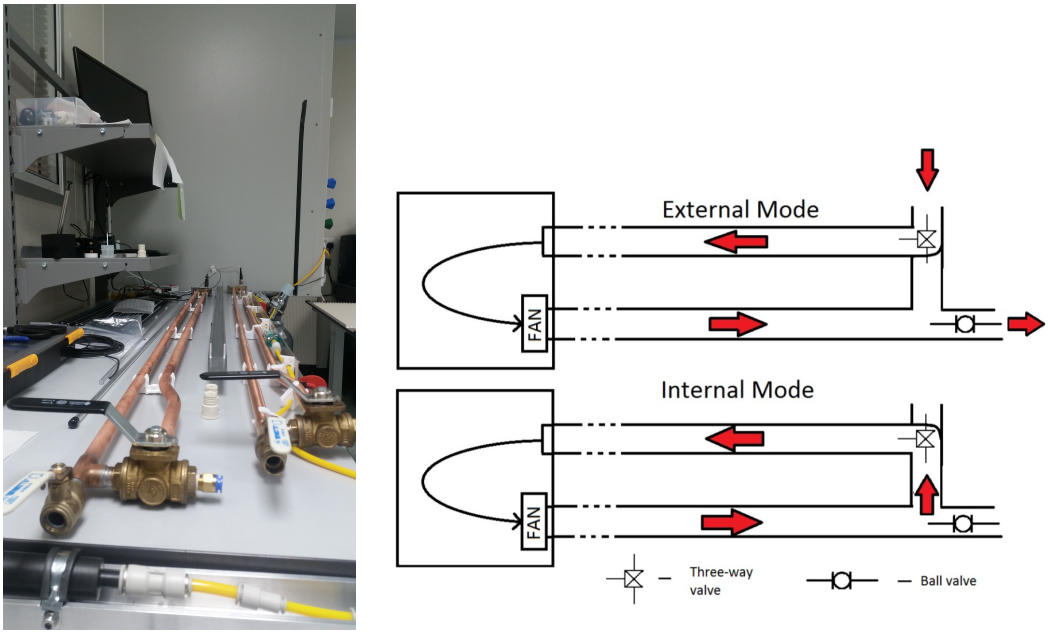

(a) (b)

Figure 47: Photo of the leak testing chamber apparatus in the Liverpool clean room, and diagram of the leak testing chambers illustrating the internal and external modes [75].

out via a digital E2 serial interface using an arduino. The steerable measurement interval is set to the minimum possible 15 s to ensure the most accurate determination of the leak rate in the shortest possible time.

6.2.2 Leak testing procedure

The leak rate of the straw is measured by filling the straw with CO_2 at a pressure of 15 psi and inserting it into a sealed chamber with a CO_2 detector.

Chamber preparation

Prior to performing the leak test, the chamber is flushed with nitrogen to remove any residual CO_2, at a rate of 2.5 L/min for approximately 20 minutes.

Straw preparation

The straws arrive from the vendor in lengths of 130 cm with a supportive layer of paper inside. The length and resistance of each straw is measured prior to any handling as a quality control procedure. The straws must be leak tested without the paper layer, so this is removed carefully

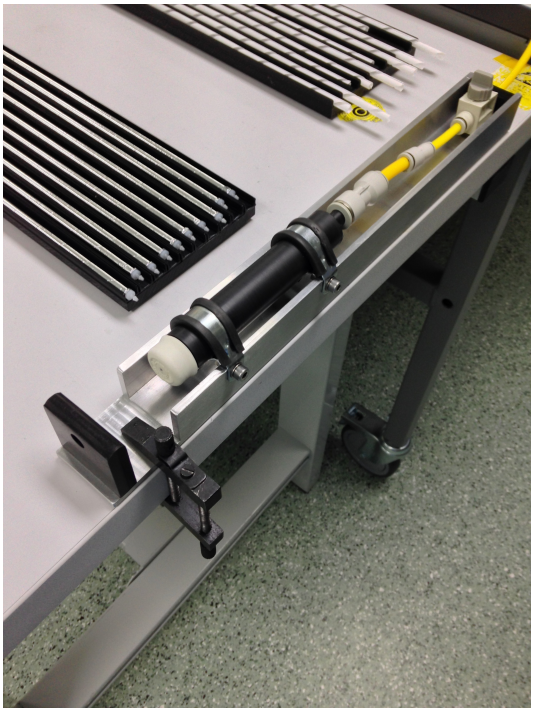

Figure 48: The full-length straws prepared for leak testing, with their injection moulded endpieces glued in. Also shown is the custom-built syringe filling apparatus, used in the calibration procedure.

prior to testing. After paper removal, the straw resistance is measured once again to check that removing the paper did not damage the straw. The paper of every 15^{th} straw is visually inspected using a SmartScope to ensure that the gold layer on the inside of the straw is not being removed with the paper.

Approximately 5 cm of viton tubing is attached to an injection-moulded straw end-piece, one of which is inserted into either end of the straw to be leak tested. The diameter of the end-piece is slightly smaller than the straw diameter in order for it to be inserted into the straw without damaging it. The end-pieces are glued into the straws using rapid Araldite; this is applied generously in order to ensure a good gas seal. The straw is left in a preparation tray while the glue cures for up to 3 hours.

When the glue has cured, the straw is carefully transferred into a metal leak-testing tray. The tray has higher walls than the straw height in order to protect it during its time in the leak testing chamber, and is flat at either end where the viton tubing rests. The CO_2 is connected to one end of the straw and the straw is flushed with CO_2 for 30 s. After flushing, a barbed plug is used to

seal the other end of the straw and stop the flow of CO_2.

The straws in the SRV will experience a pressure of 15 psi, and so they are leak tested at a relative pressure of 15 psi above atmospheric pressure (30 psi absolute pressure). However, the straws must be able to withstand up to 25 psi (relative) to ensure they would not be damaged in the event of a problem with the gas supply, which contains a relief valve that directs the gas away from the straws if the pressure in the system exceeds 25 psi. To check that the straws meet this requirement, the pressure of the CO_2 inside the straw is increased to 25 psi and held for 1 minute before being reduced to 15 psi for the leak test. When the pressure is at 15 psi, the viton tubing is clamped to isolate the straw from the gas line, and then cut between the clamp and the gas line; a second barbed plug is inserted into the open end of the tubing and the clamp is released. The straw is secured in its metal tray using kapton tape and is then inserted into the leak testing chamber, which continues to be flushed with nitrogen at a rate of 2.5 L/min. The nitrogen flush continues for 2 minutes after the straw is inserted, to remove any residual air that was introduced with the straw and tray. The chamber is then switched to the 'closed' configuration and the nitrogen line removed before running the leak test.

Running the leak test

Straw identification information and the desired time for the leak test are entered via a GUI prior to starting the test. Initially, data was taken for 2 hours, the maximum possible test length, in order to obtain the smallest error on the leak rate measurement. The length of test is limited by the viton tubing used to connect the straw to the gas line; after 2 hours, it becomes saturated with CO_2, which will then begin to leak through the tubing and affect the measurement of the straw leak rate. In addition, the straw should not be left sealed with the permeating gas for too long, since the pressure in the straw would eventually become so low relative to its surroundings that the straw material would become creased and potentially damaged. The measurement time of 2 hours was reduced after the per-straw leak rate requirement was better understood (see section 6.2.3) since the required precision of the leak rate was relaxed, and the rate of the other module production procedures had increased such that leak testing now took a significant fraction of the total time to produce a module. The test time was reduced to 40 minutes.

The raw ppm values from the detector and the average leak rate of the measurements taken

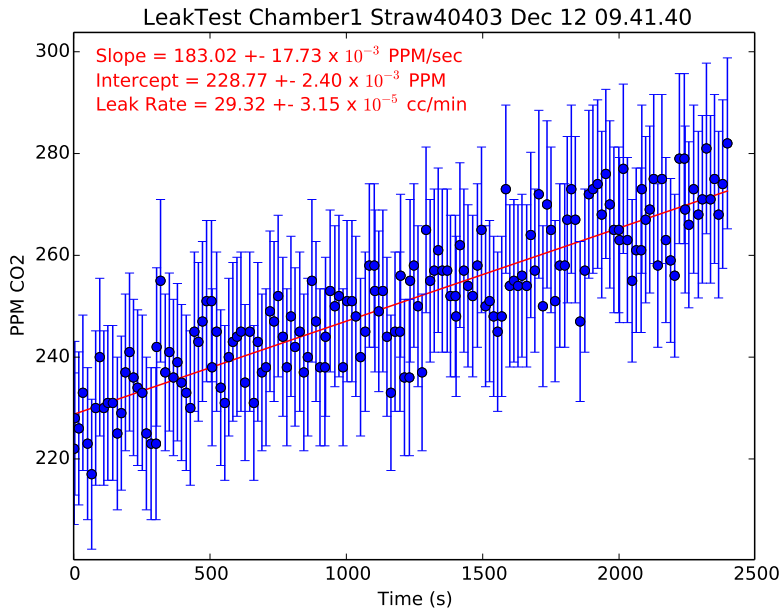

Figure 49: An example of the output of the straw leak tests. The y axis shows the ppm recorded by the CO_2 sensor in the leak testing chamber; the x axis is the time of the recording. The error on each ppm measurement is determined by the accuracy of the detector; for this sensor, the uncertainty on each ppm value is ±50 ppm +2% of the value. A slope is fitted using a least-square minimisation technique, and is converted into a leak rate according to equation 6.66.

are displayed continually throughout the test so that the user can manually stop the test if the readings indicate a problem with the test e.g. a burst straw or failed glue seal. Otherwise, the test ends after the specified test time, and a plot such as that in figure 49 is uploaded automatically to an online database, along with a pass/fail flag.

Calibration and background measurements

The gradient, given in ppm/s, of the leak test plot (figure 49) is converted into a leak rate in units of ccm using the following equation:

$$\text{Leak Rate [ccm]} = \text{slope [ppm/s]} \times \text{chamber volume [cc]} \times 10^{-6} \times 60 \ . \tag{6.66}$$

From equation 6.66, it is clear that in order to obtain an accurate leak rate measurement, the volume of the testing chamber must be known. This is determined by injecting a known volume of CO_2 into an empty leak testing chamber and measuring the average ppm value recorded by

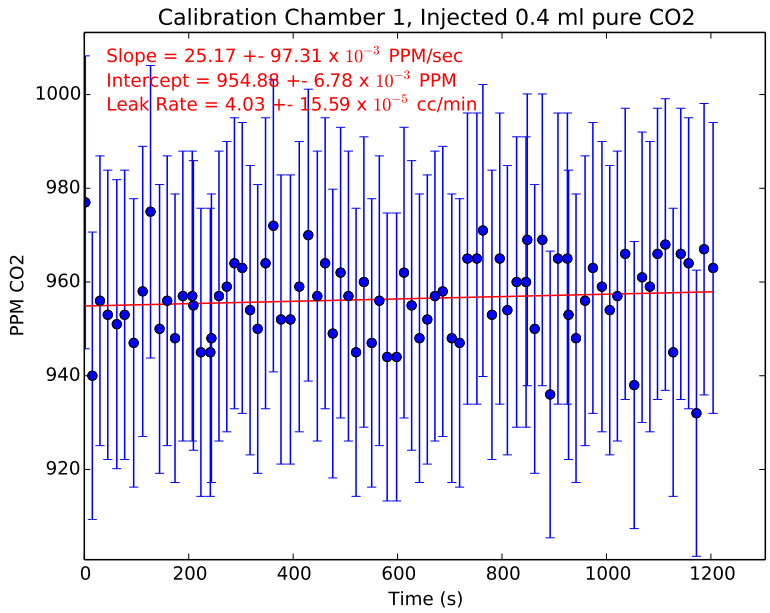

(a)

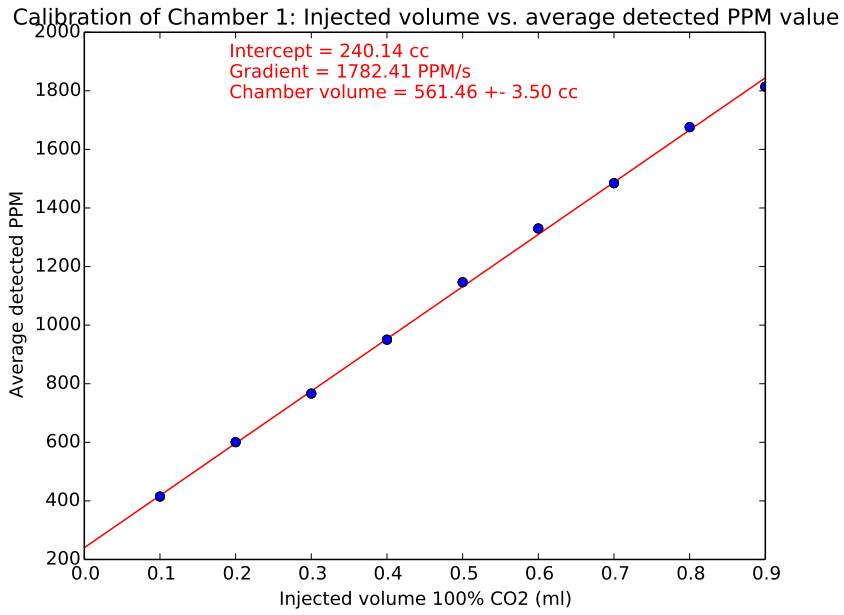

(b)

Figure 50: Plots from the calibration tests for a leak testing chamber. Plot (a) is the result of a single calibration measurement; in this case, 0.4 ml pure CO_2 has been injected and readings taken for 20 minutes. The data is fitted to obtain the intercept which gives the average detected ppm value for this injected volume. This measurement is performed for a range of injected volumes and the results are shown in plot (b). If the sensor is behaving correctly, the detected ppm value should increase linearly with increasing injected volume. The intercept of plot (b) is effectively a measurement of the offset of the CO_2 sensor - the reading returned when the chamber is empty. Several batches of calibration tests were performed over time to ensure the offset was consistent and not just indicative of a problem with one particular set of measurements. It can be seen in figure 51 that this offset is consistent with the long-term background measurement performed on this chamber.

the sensor over a period of time. The chamber volume can be determined using the equation:

$$\text{Chamber volume [cc]} = \frac{\text{Injected volume [cc]}}{\text{Measured volume [ppm]} \times 10^{-6}} \,. \tag{6.67}$$

While the chamber volume can be determined from any sensible injected volume, an average chamber volume measurement is determined from calibration measurements taken for a range of different injected volumes. Obtaining a plot of the measured volume for a range of different injected volumes is also a good way to ensure proper behaviour of the CO_2 sensor; figure 55b shows the average measured ppm value for injected volumes in the range $0.0 - 0.9$ ml. This plot should be linear for a well-behaved sensor, since the measured volume should increase linearly with increasing injected volume.

To perform the calibration tests, the chamber is flushed with Nitrogen to remove any residual CO_2. Instead of sealing the chamber using both valves, as for a usual leak test, the open end of the chamber is sealed using a suba-seal through which a syringe can be injected; the gas inlet side is sealed using the valve as usual and the nitrogen line removed. A 1 ml syringe with a side-hole (rather than a hole at the end of the needle) is used to ensure that no material is removed from the suba-seal on injection, and that the seal will be unbroken when the needle is removed. The syringe is filled with pure CO_2 using a custom-built apparatus, shown in figure 48. The apparatus is made from a hollow plastic tube with a volume much larger than the volume of the syringe. The tube is connected to a gas supply at one end and is open at the other to enable the volume to be flushed with the gas to be injected. The open end is then sealed with a suba-seal, through which the syringe needle can be inserted in order to extract the desired volume of gas. The data from one calibration test is shown in figure 50.

In addition to periodic chamber calibration tests, the background leak rate measured by the sensor is also measured regularly. The chamber is flushed with Nitrogen for at least 20 minutes before it is closed to atmosphere and a leak test is performed on the empty chamber. An example of a background measurement is shown in figure 51. The most recent background measurement for each chamber is entered as part of the pre-test information in the GUI before each leak test, and the background rate is subtracted from the measured leak rate for each straw.

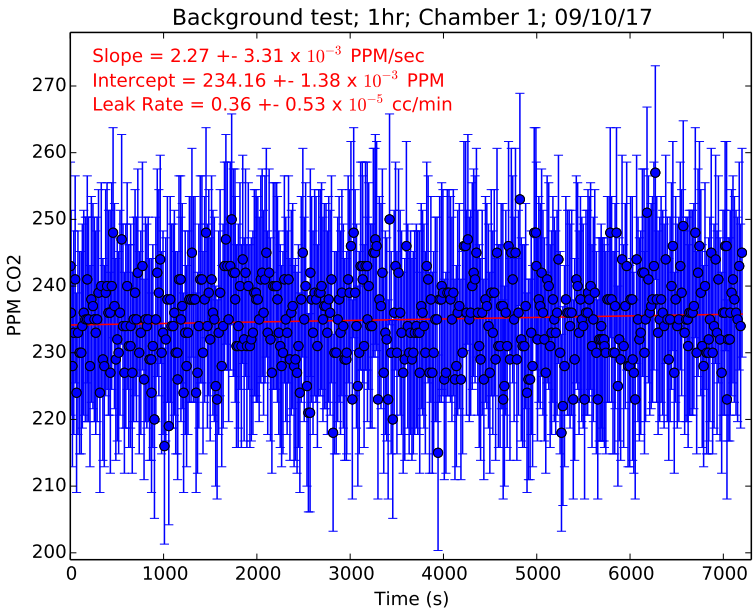

Figure 51: A background leak rate measurement for Chamber 1.

6.2.3 Results of leak tests

The average per-straw leak rate for straws from the first batch of straws to be tested (batch 1), tested with 50:50 Ar:CO_2, is 0.95×10^{-4} ccm, from figure 52. At the time of testing the batch 1 straws, the factor for converting the leak rate of CO_2 to that of ethane had not been quantified, although it was expected that ethane would leak at a much slower rate than CO_2. Since the conversion factor was not known, it was originally decided that the straws should conform to the stricter requirement for using Ar:CO_2, in case any future decision was made to use this rather than Ar:C_2H_6 (the choice of drift gas is discussed in section 5.5.3). The original threshold for straws was initially set at 1.0×10^{-4} ccm. It was quickly noticed during the initial testing of the straws that several straws were failing this requirement. Since satisfaction of the per-tracker leak rate specifications required only that the *average* leak rate of the straws should not exceed 1.0×10^{-4} ccm (for 50:50 Ar:CO_2[5]), the conservative threshold was relaxed to 2×10^{-4} ccm in order to obtain enough straws to produce a full tracker station. The pass rate of straws at the relaxed threshold was $\sim$ 88%.

[5]The original design of the trackers was to use 80:20 Ar:CO_2. Assuming that the leak rate of Ar is negligible compared to the leak rate of CO_2, the average per-straw leak rate requirement of 5.6×10^{-5} ccm would be satisfied at a leak rate of 1.4×10^{-4} ccm as measured using 50:50 Ar:CO_2. In order to allow for a safety factor, the target average was set at 1.0×10^{-4} ccm for 50:50 Ar:CO_2.

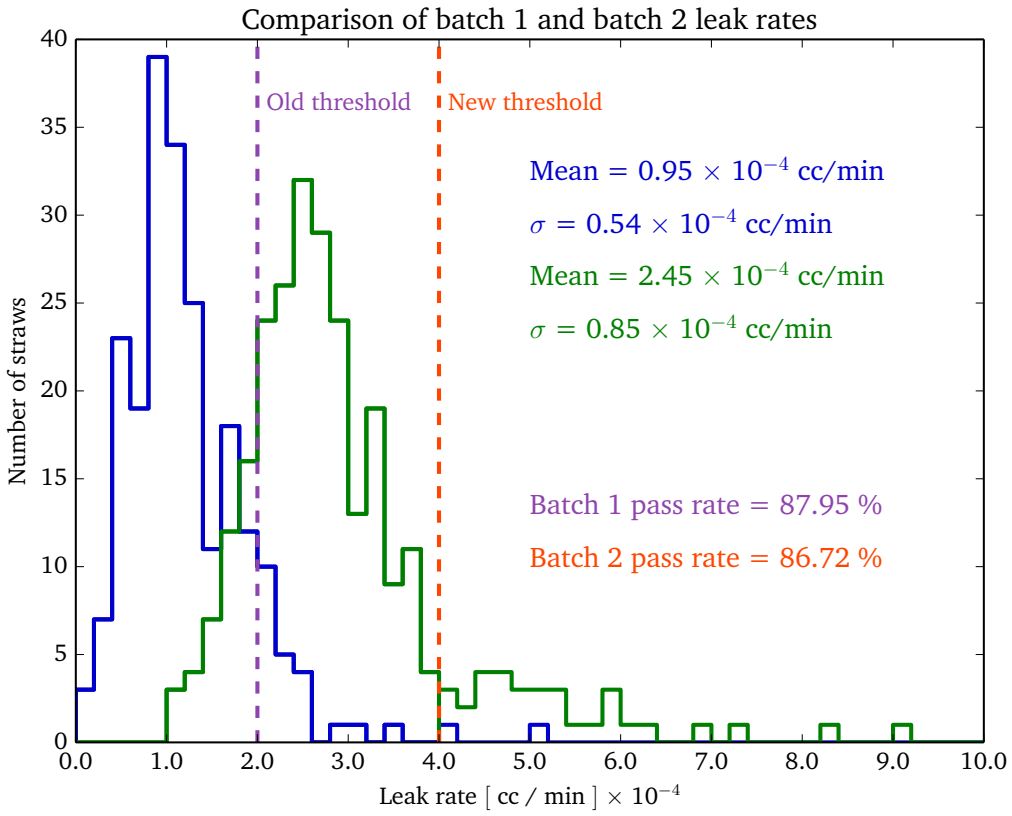

Figure 52: Leak rates for all batch 1 (blue) and batch 2 (green) straws. All leak rates are quoted for 50:50 Ar:CO_2 gas. The mean leak rate for batch 1 straws was 0.95×10^{-4} ccm for 50:50 Ar:CO_2 gas; the pass rate for the old threshold of 2×10^{-4} ccm was 88%. The mean leak rate for batch 2 straws was 2.45×10^{-4} ccm; the pass rate at the new threshold of 4×10^{-4} ccm was 87%.

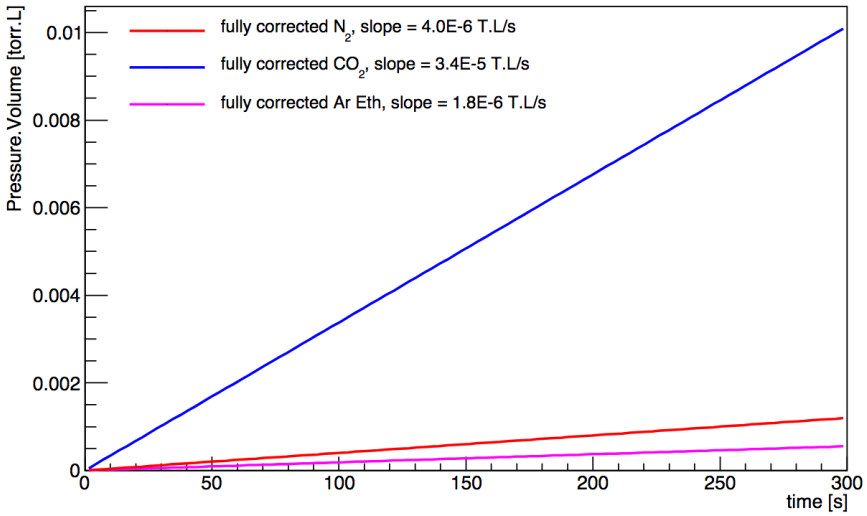

Figure 53: Summary of the RoR tests performed on module 00, a batch 1 module, with different gases. The slope of 3.4×10^{-5} Torr·L/s using 100% pure CO_2 is slightly higher than, but not inconsistent with, the measured leak rate of pure CO_2 for module 00 of 1.96×10^{-5} Torr·L/s calculated from the individual straw leak tests.

The batch 2 straws differed in radius and wall thickness from the batch 1 straws. To avoid complications associated with having straws of different geometry within a single tracker station, it was required that all straws for a particular station should come from the same batch. Batch 2 straws were used for the construction of the second and third tracker stations. Due to the difference in wall thickness, the average leak rate for the batch 2 straws was considerably higher than that of the batch 1 straws, at 2.45×10^{-4} ccm. The increase in average leak rate was apparent from the first few straws that were tested, and it was clear that the 2×10^{-4} ccm threshold would need to be relaxed further in order to obtain enough straws to build the remaining modules. By the time that the testing on the batch 2 straws began, extensive vacuum tests had been performed at Fermilab on the first production module, and the module leak rates using Ar:CO_2 and Ar:C_2H_6 had been studied in depth. These tests confirmed the initial hypothesis that ethane would permeate at a much slower rate than CO_2 (figure 53). The per-module leak rate measured using pure CO_2 was 3.5×10^{-5} Torr·L/s, while the per-module leak rate using 50:50 Ar:C_2H_6 was 1.88×10^{-6} Torr·L/s– an improvement of almost a factor of 20. The results of these studies enabled the per-straw leak test threshold to be relaxed to 4×10^{-4} ccm. The pass rate of the batch 2 straws at this threshold was $\sim$ 87%.

The leak rate distributions and pass rates for batch 1 and 2 straws are shown in figure 52. The

		50:50 Ar:CO_2 (ccm)	50:50 Ar:CO_2 (Torr·L/s)	50:50 Ar:C_2H_6 (ccm)	50:50 Ar:C_2H_6 (Torr·L/s)
Per-straw	**Batch 1**	9.35×10^{-4}	1.17×10^{-5}	2.33×10^{-5}	2.92×10^{-7}
	Batch 2	1.93×10^{-2}	2.42×10^{-4}	4.83×10^{-4}	6.04×10^{-6}
Per-module	**Batch 1**	9.35×10^{-4}	1.17×10^{-5}	2.33×10^{-5}	2.92×10^{-7}
	Batch 2	1.93×10^{-2}	2.42×10^{-4}	4.83×10^{-4}	6.04×10^{-6}
Per-tracker	**Batch 1**	7.48×10^{-3}	9.35×10^{-5}	1.87×10^{-4}	2.34×10^{-6}
	Batch 2	1.93×10^{-2}	2.42×10^{-4}	4.83×10^{-4}	6.04×10^{-6}

Table 2: The average per-module and per-tracker leak rates for batch 1 and batch 2 straws. Both the batch 1 and batch 2 per-tracker average leak rates satisfy the per-tracker upper limit of 4.5×10^{-5} Torr·L/s comfortably when Ar:C_2H_6 is used.

average per-tracker permeation rates for trackers built from batch 1 and batch 2 straws are summarised in table 2; both types of tracker station satisfy the per-tracker leak rate upper limit when Ar:C_2H_6 is used.

6.3 Summary of tracker vacuum performance

6.3.1 Vacuum tests at Liverpool

Each tracker module is placed in a vacuum tank at Liverpool prior to being transported to Fermilab in order to test it meets the required vacuum levels, and to check that no damage occurred to the straws during construction. The vacuum pressure in the tank is read-out via a serial link for the duration of the pump-down – a plot of the vacuum pressure is shown in figure 54.

The QA procedure at Liverpool requires each module to reach a vacuum pressure of 1×10^{-6} Torr in a reasonable time before it is able to be shipped to Fermilab. In the event that a module does not reach the required vacuum pressure, the module is removed from the tank and any potential leaks are identified. If no problems with any of the gas seals or O-rings on the manifolds are found, the straws are inspected for leaks that may have been incurred during module assembly. Any straws with holes in are identified and can be plugged inside the manifold to stop the gas from flowing through this channel. In cases where this straw is in an accessible location, the straw is cut out and the hole glued. While straws only failed very occasionally, any failed straw caused undesirable delays in the post-production vacuum testing of the modules. During the construction of the batch 2 modules, a visual quality inspection step was added to check the straws for defects after they had been leak tested and cut to length. This was added since it was noticed that some

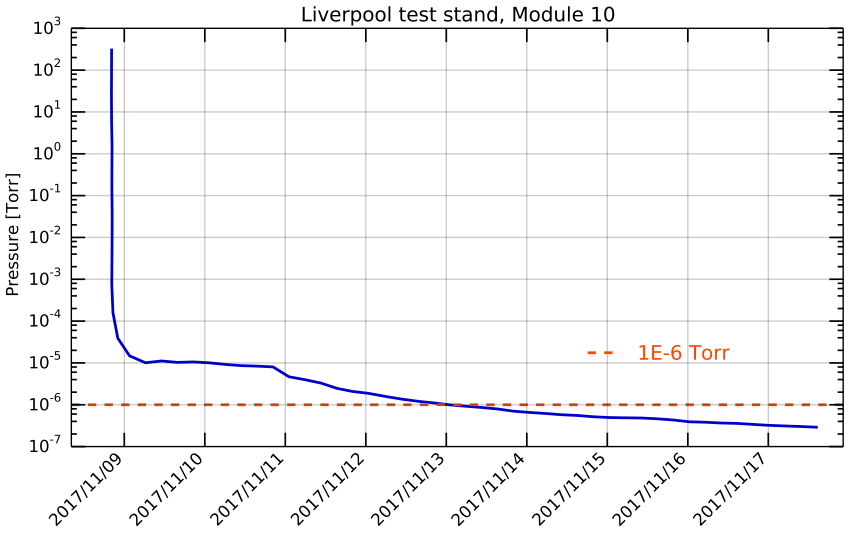

Figure 54: Plot of the pressure in the Liverpool vacuum tank as a function of time. Each module is pumped down to ensure that the vacuum in the tank reaches a pressure of 1×10^{-6} Torr in a reasonable time.

straws had weak seams, localised to a small area of the full length straw, which would be liable to tear and induce a leak when the module was tensioned. After this step was added, no further straw leaks were detected post-assembly.

6.3.2 Post-transport vacuum tests at FNAL

Each tracker module is tested for vacuum performance after it has been shipped to Fermilab to ensure it was not damaged during transportation. The minimum vacuum pressure reached is recorded for each module. Long-term pump-down tests were performed on selected modules only, since it was not possible to test all modules for a very long time due to time constraints. The modules that were tested for a shorter time were checked against the rate of pump-down for the long-term tests; if a module reached the expected pressure for the given time period then the test could be ended early. The RoR of every module was measured by switching off the vacuum pump but leaving the tank sealed, and measuring the increase in vacuum pressure over a period of 3 minutes. The rate of rise and minimum pressure of each module can be seen in figure 55.

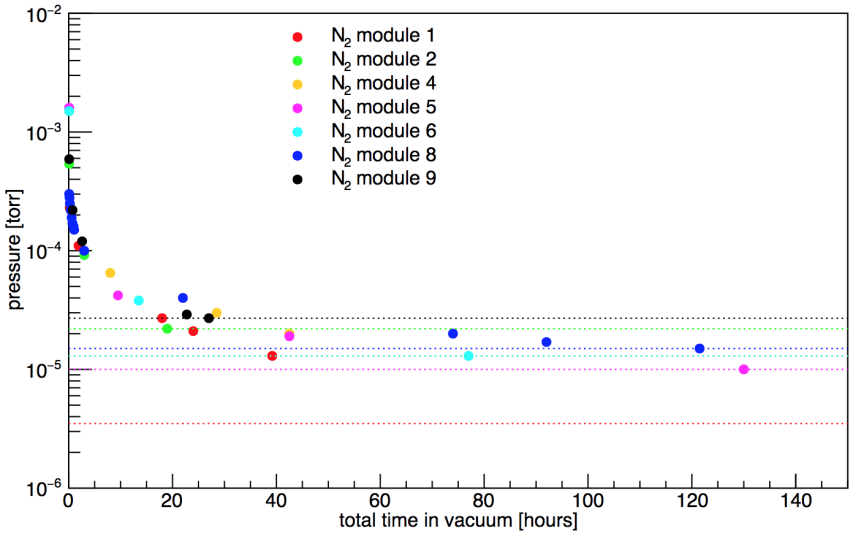

(a)

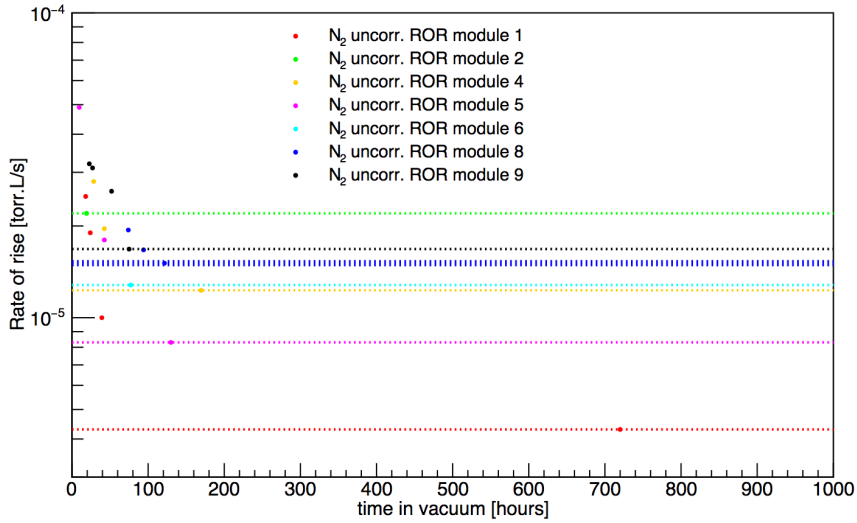

(b)

Figure 55: Plots summarising the post-transport vacuum tests performed at Fermilab. Plot (a) shows the minimum pressure reached in the vacuum tank by each module; plot (b) shows the minimum rate of rise measurement for each module. The tests were performed using nitrogen, and per-module RoR must be less than 1.2×10^{-5} Torr·L/s.

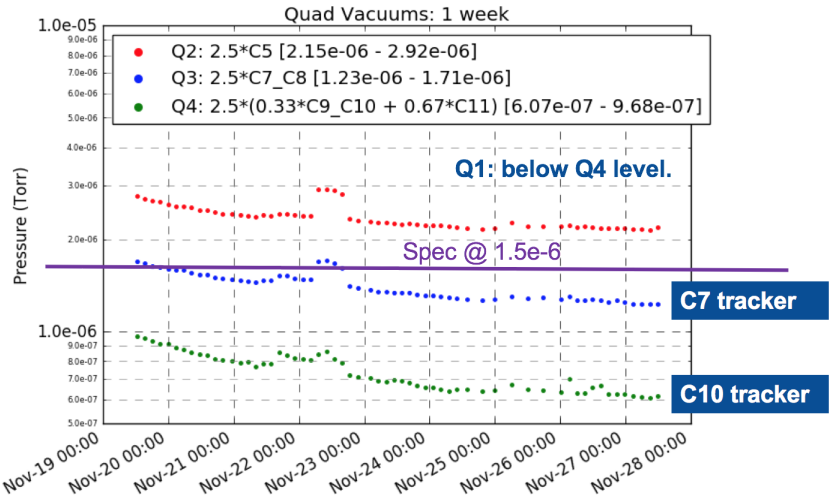

(a)

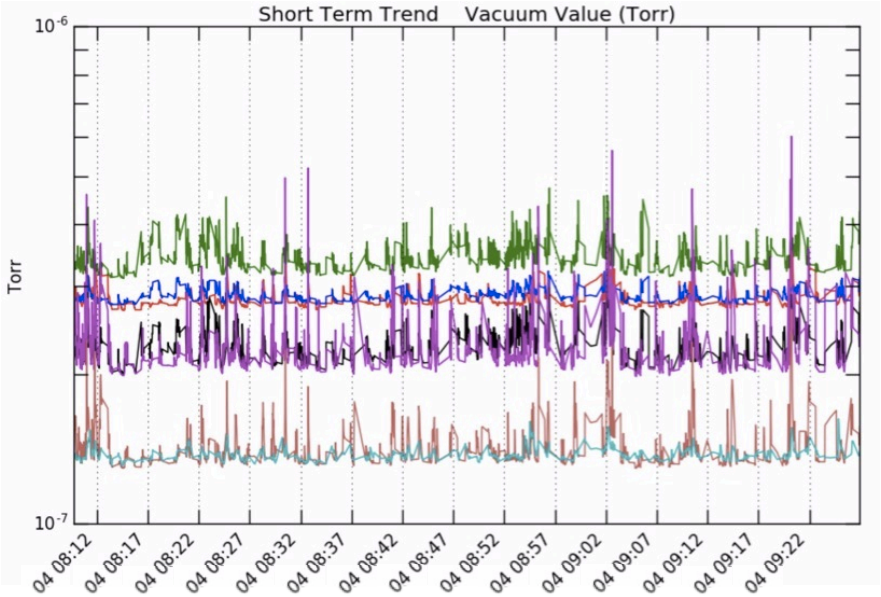

Figure 56: The SRV pressure at the tracker stations. (a) shows the gauge readings after the initial pump-down and (b) shows the SRV status in April 2018. In plot (b), the different colours represent data from the different gauges around the SR. The purple and green lines are from the gauges closer to the two tracker stations.

6.3.3 Overall SRV performance and measurements

Figure 56a shows the vacuum pressures recorded by the gauges closest to the two tracker stations at the end of the initial pump-down; figure 56 shows a screen shot of the online SRV monitoring system in April 2018. After an initial period of out-gassing, the target vacuum pressure was comfortably achieved, and the trackers have been operating stably in vacuum for the full running period.

Chapter 7

Development of track extrapolation software

As well as producing the straw tracker hardware, a major part of the straw tracker commissioning was to develop reconstruction software to turn the raw straw hit information into a measurement of the muon beam. Individual straw tracker hits would be grouped together in narrow temporal windows, and a trajectory would be fitted to the space points on the tracker planes. The trajectory in the straw tracker provided the magnitude and direction components at the point where the track entered the detector. These components were used as input to the track extrapolation algorithm, which was used to propagate the track parameters back through the varying magnetic field until the most probable muon decay position was reached. A unique challenge that presents itself in this experiment is that there is no fixed interaction point, and so the most likely decay position must be estimated.

In this chapter, a brief overview of the track finding (grouping together of hits) and fitting procedures will be provided, followed by an in-depth explanation of the Runge-Kutta extrapolation algorithm that was implemented to propagate the track trajectory. The method used to identify the most likely muon decay position will be described, and results from simulation illustrating the performance of the extrapolation algorithm will be presented.

7.1 Overview of track reconstruction procedure

The hits in the straw trackers are grouped together into track 'candidates' and the points on the candidate are fitted according to the procedure described in chapter 5, in order to obtain the track parameters (position, momentum) at the entrance and exit planes of the tracker. The track parameters at the entrance to the trackers are extrapolated back to the assumed muon decay position. There is no fixed interaction point in the $g-2$ experiment, and so the trajectories of the decay e^+ are extrapolated back to the point at which the momentum of the positron is tangential to the magic radius (the 'point of radial tangency'). This is described in detail later in this section.

The parameters at the exit plane are extrapolated forwards to the calorimeter face in order to provide precise information about the position and momentum of the e^+ hitting the calorimeter, and cross-check the calorimeter's identification of pileup events; this uses an identical procedure as described in this chapter.

A fourth-order Runge-Kutta Nystrom algorithm [76] is used to propagate the track parameters through the varying magnetic field in the fringe region (where the trackers are located) and through the uniform field until the approximate position of the muon decay is reached. A fixed-step approach is used, to allow the geometry in the simulation to be queried at each step, in order to determine the likelihood that the extrapolated track passed through material. Tracks that hit material will lose energy and/or undergo multiple scattering, causing the trajectory to deviate from its ideal path. As such, tracks that are likely to have hit material are flagged as low-quality such that they can be ignored in the eventual analysis.

7.2 Track extrapolation procedure

A track extrapolation algorithm, `RKExtrapolation`, was implemented into the $g-2$ software framework. The procedure consists of the following stages:

- The track parameters (position and momentum components) and covariance matrix are propagated along a step.
- At the end of the step, the geometry is queried to determine whether or not the track has hit material. If so, the track parameters at the location of the material that was hit are returned.
- The radial momentum component, p_r, of each step is evaluated. The extrapolation stops when $p_r = 0$, or in other words, when the track direction is tangential to R_0.
- In the case that the extrapolation direction is forwards to the calorimeter, the extrapolation stops when the calorimeter face is reached.

Each of these stages will now be described in detail.

7.2.1 Runge-Kutta Nystrom algorithm for track parameter propagation

The extrapolation algorithm `RKExtrapolation` uses a fourth order Runge-Kutta Nystrom method to propagate the track parameters along the given step length. The algorithm is described fully

in [76] and [77]. The algorithm begins with a state vector, $S_i = \{x, y, z, p_x/p, p_y/p, p_z/p, 1/p\}$. The parameters are propagated along the step length d_0 by evaluating the equation of motion at four intermediate stages. The magnetic field is queried at each intermediate stage, but the second and third stages are evaluated at the same spatial point so have the same field value. The angles of the track at each stage are weighted to obtain the final state vector S_f at the end of the step. The determination of the angles at each stage is illustrated in figure 57.

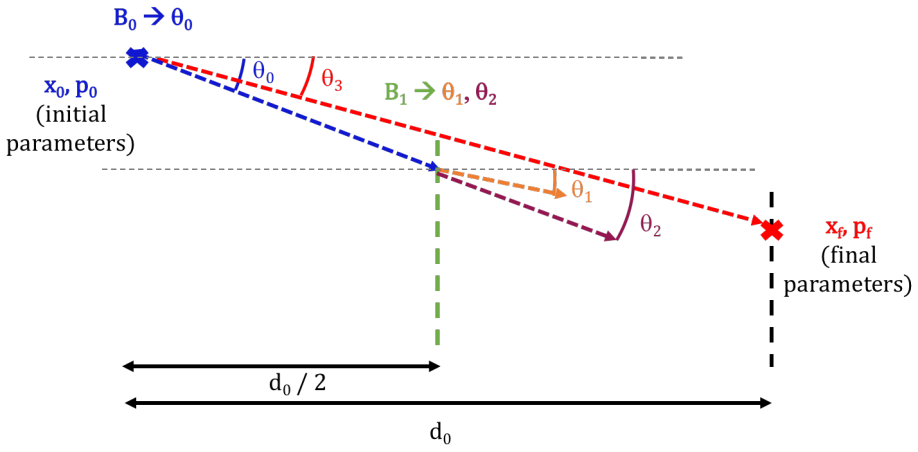

Figure 57: Diagram illustrating the intermediate 'stages' of the track extrapolation across a single step using the Runge-Kutta Nystrom method. The initial momentum p_0 and the magnetic field value B_0, defined at x_0, are used to calculate the angle θ_0. The second and third intermediate stages evaluate the angles θ_1 and θ_2 using the magnetic field defined at an intermediate position $d_0/2$ (halfway along the step length d_0. Each angle θ is calculated based on the previous angles (apart from the first). At the end of the step the angles θ_0, θ_1 and θ_2 are weighted to obtain θ_3, which is used to obtain the final position and momentum components at $x_f = x_i + d_0$.

7.2.2 Propagation of the covariance matrix

As well as propagating the track parameters S, the covariance matrix of the track must also be propagated to the final point in order to obtain the corresponding uncertainties on the final parameters. The algorithm for the propagation of the covariance matrix is the *Bugge-Myrheim* method, described in [78, 79]. The propagation of the covariance matrix has three parts. Firstly, the covariance matrix in the local detector coordinates must be rotated into the global frame in which the extrapolation is performed. Secondly, the transport Jacobian for each step is obtained according to the *Bugge-Myrheim* method. The product of the Jacobians for each step gives the total Jacobian describing the transport of the covariance matrix from the start point to the end point, in global coordinates. This is a 7x7 matrix that contains the derivatives for each of the

parameters in the state vector S. The final stage is to rotate this 7x7 Jacobian into the coordinates of the end point and obtain a 5x5 matrix that can be multiplied with the covariance matrix to obtain the covariance matrix in the target coordinates. The covariance matrix from the track fit is a 5x5 matrix with elements $u, v, u', v', 1/p$ where u' and $v' = \frac{d(p_u)}{d(p_z)}$ respectively. The algebra for the transport of the Jacobian in the global frame, and for transforming between the 5x5 initial and final covariance matrices to/from the 7x7 global Jacobian is performed using code from the `GENFIT` package [80].

7.2.3 Step size studies

In the uniform field region, the accuracy of the extrapolation is independent of step length since the path follows a perfectly circular trajectory and the field does not vary along the step length. Large step sizes can be used in this region to save computation time. In the fringe field region, the magnetic field gradient over a single step can be significant, and so the accuracy in this region is heavily dependent on step length. Additionally, the accuracy of the step propagation in the fringe region depends on the curvature (momentum) of the track. The relationship between step size and track accuracy for tracks of different momenta was studied using Monte-Carlo tracks.

To test the algorithm, a given set of initial parameters (position and momentum) were extrapolated forwards for some number of steps of fixed length n, the direction reversed and then the same number of steps extrapolated back to the initial starting point. In a perfectly uniform field, this is expected to return the initial parameters exactly. In a varying field region, the track will not perfectly recover its initial conditions, since the field used to extrapolate one step in the forwards direction will be slightly different to the field used to extrapolate the same step backwards. For an individual step, the 'relative propagation error', ε, is defined as:

$$\varepsilon = \frac{\delta_0}{d_0} \tag{7.68}$$

where δ_0 is the error between the initial and final positions at the start point, and d_0 is the step size. The relative propagation error over a number of steps n is cumulative; ε can also be defined using the error Δ over n steps of length d_0:

$$\varepsilon = \frac{\delta_0}{d_0} = \frac{\Delta}{d}\,, \tag{7.69}$$

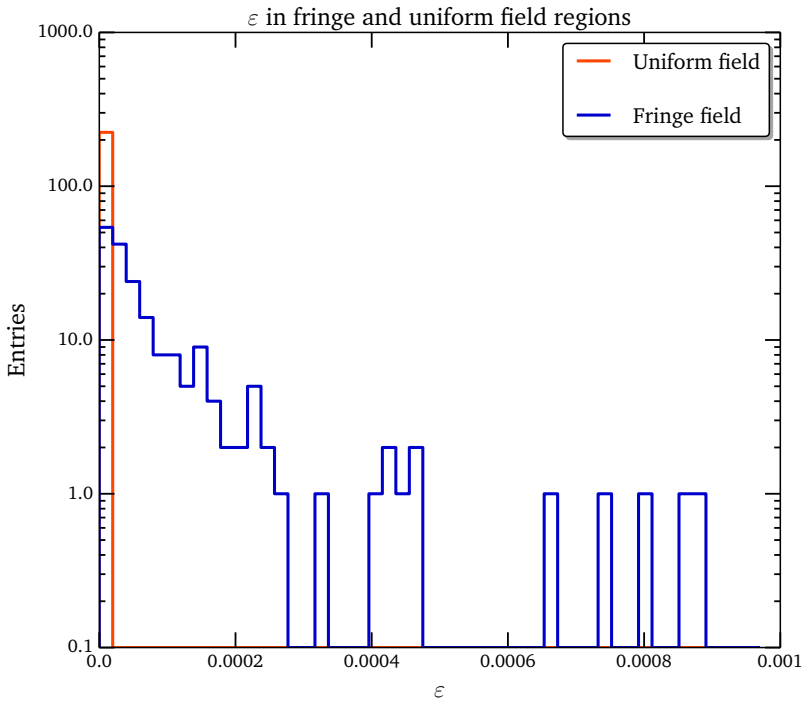

(a)

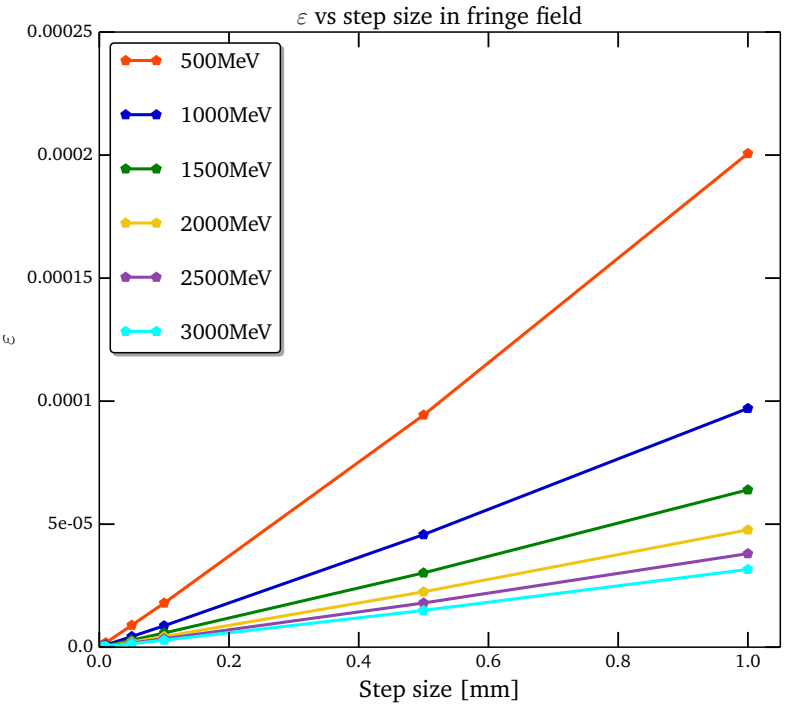

(b) Vertical position

Figure 58: Plots illustrating the dependence of the step size parameter ε on step size and momentum. Plot (a) shows ε in the fringe field (blue) and uniform field (orange) regions. Plot (b) shows ε as a function of step size for different momentum tracks, in the fringe field region.

where $d = nd_0$. The relative propagation error is a useful quantity since it gives a measure of the performance of the extrapolation that is independent of track length.

The relative propagation error for a number of tracks that have been extrapolated forwards and backwards for $d = 20$ cm in the uniform and fringe field regions is illustrated in figure 58a. $\varepsilon = 0$ in the uniform field as expected, illustrating that the algorithm is working correctly. There is, however, a range of values for ε in the varying field region. Figure 58b shows ε as a function of step size for different momentum tracks. There is a linear relationship between ε and step size, and the rate of increase of ε with step size increases with decreasing momentum. This is expected, since lower momentum tracks bend more than high momentum tracks. This relationship can be used to choose the optimal step size for a track of given momentum, based on the likely distance that the track will travel.

7.2.4 Volume cut

Due to the geometry of the $g - 2$ SR, a significant number of tracks will pass through some material on their way to the tracking detectors, causing them to undergo multiple scattering and/or energy loss. This causes the e^+ to deviate from their trajectories in ways that cannot be easily accounted for using the extrapolation algorithm. These events must be ignored as their reconstructed positions will be inaccurate, and large tails will result in the eventual distributions. The distribution of the different volumes hit by the tracks is shown in figure 59, and the effect of the cut on the radial and vertical position and momentum resolutions is shown in figures 60 and 61. The azimuthal acceptance of different types of events are shown in figure 62a and the radial and vertical position resolutions for different event types are shown as a function of distance in figure 62b.

7.3 Determination of radial tangency point

A unique challenge in the development of an extrapolation algorithm for the $g - 2$ tracks is that there is no fixed interaction point; muons can decay anywhere around the ring, and the e^+ measured by the tracking detectors travel a range of distances. A suitable 'stopping point' for the extrapolation must be found. The situation is simplified if the μ^+ always emitted its e^+ tangentially – in the direction of its motion – and so this is assumed for all tracks. The extrapolation stops when the momentum of the e^+ is parallel to R_0, or equivalently, when the radial component of

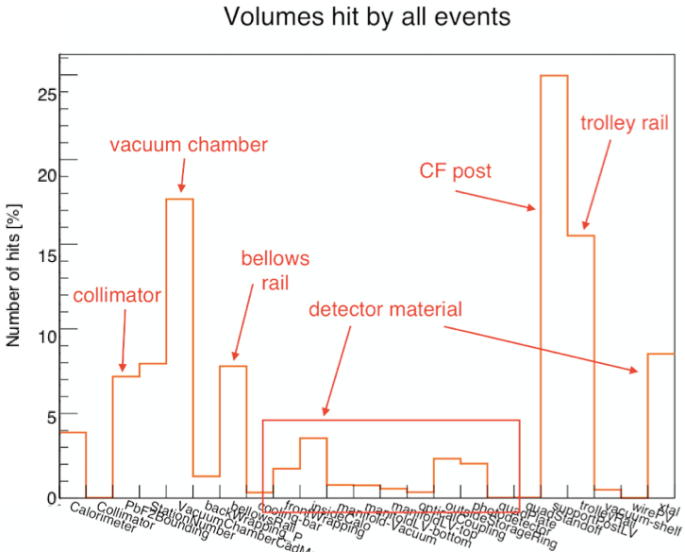

(a)

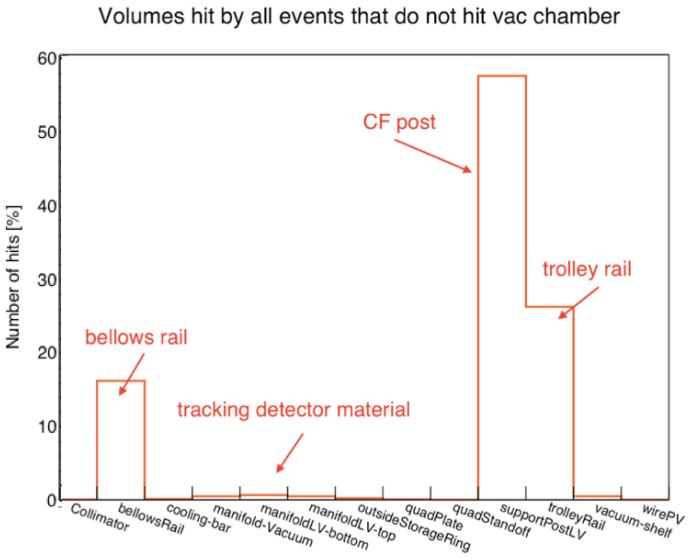

(b)

Figure 59: The frequency with which tracks hit different volumes. Tracks (events) that hit any of the calorimeter physical volumes will have had to hit a vacuum chamber also, so plot (b) shows the frequency with which tracks that did not hit a vacuum chamber hit some other volume. The data is normalised to the number of events in the plot, which for the second plot represents approximately 35% of the total number of tracks.

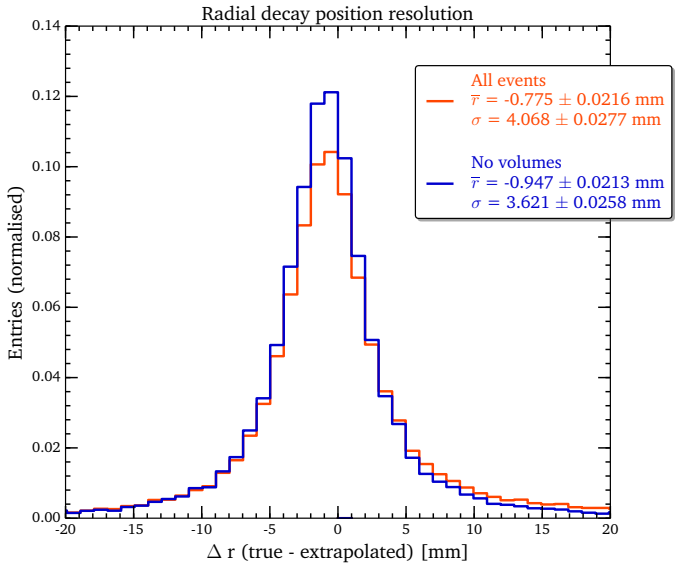

(a) Radial position

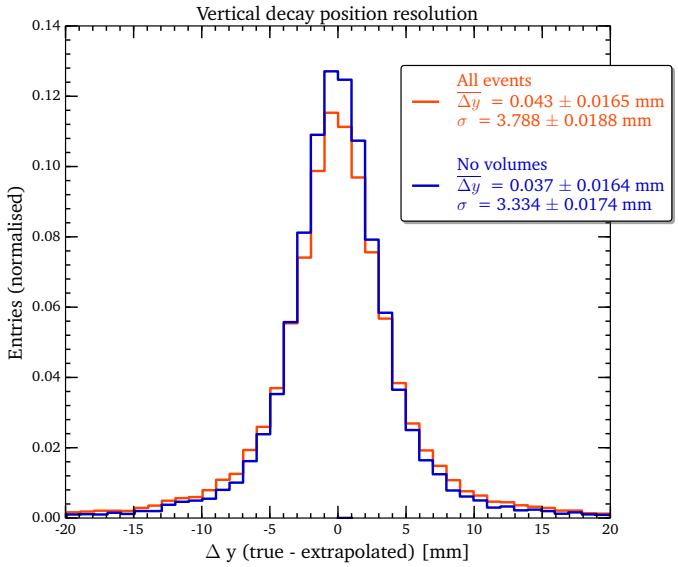

(b) Vertical position

Figure 60: Position resolution plots for all tracks (red) and with the material cut applied (blue).

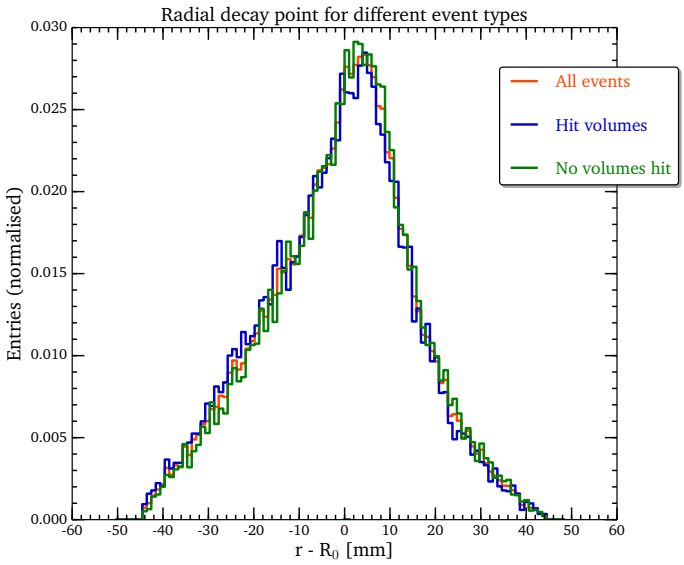

(a)

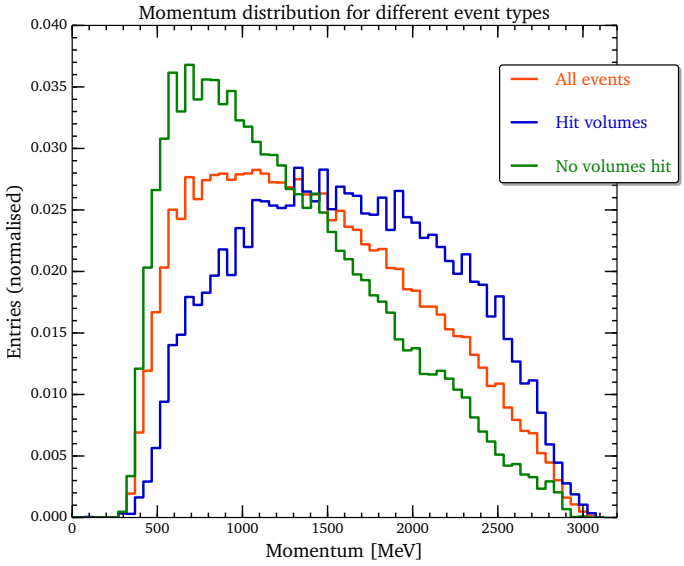

(b)

Figure 61: The plots show the distributions of (a) the simulated (true) radial decay position and (b) the track momentum. The distributions for tracks that will go on to hit solid material are shown in green, and those that will not interact with material on their way to the tracking detectors are in red. Both plots are normalised; the percentage of tracks that are removed with the volume cut is $\sim$ 30%, from figure 59. Plot (b) shows the effect of the volume cut on the momentum acceptance of the trackers. A comparatively higher fraction of tracks that will hit material have higher momentum. Removing these tracks thus shifts the momentum acceptance towards the lower momentum range. However, it is evident from figure (a) that this has no significant effect on the radial acceptance.

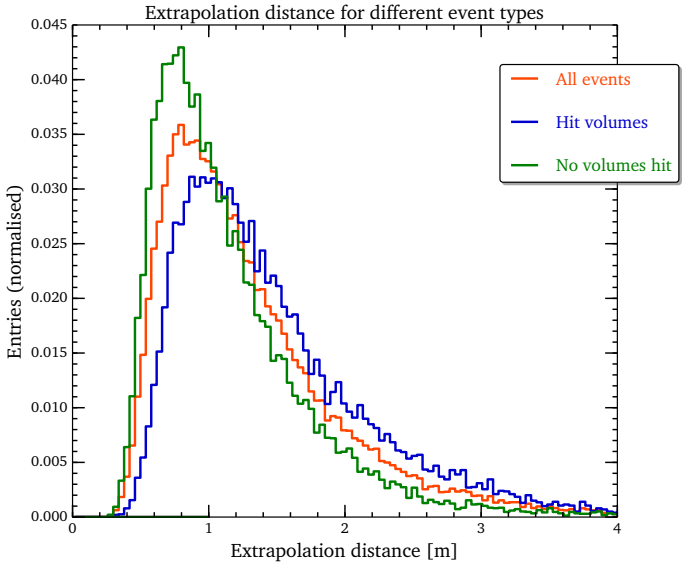

(a)

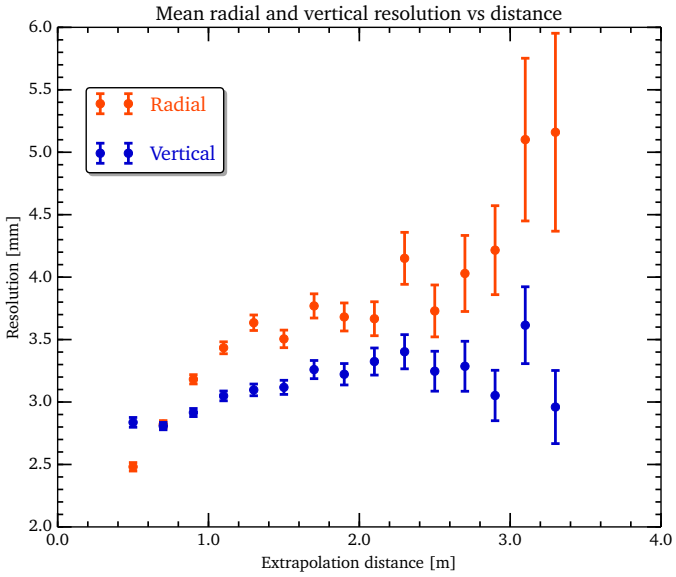

(b)

Figure 62: Plot (a) is from Monte-Carlo truth information and shows the track length (distance from decay to first detector plane) for tracks with and without the volume cut applied. Plot (b) shows the RMS of the true - extrapolated radial (orange) and vertical (blue) decay positions, with the volume cut applied. The peak of the distance distribution occurs at approximately the same distance as the point at which the radial and vertical resolutions are equal, which was one of the design criteria for the detectors. The vertical RMS does not change significantly with distance since the tracks only bend radially in the vertical magnetic field.

the e^+ momentum $p_r = 0$. The radial momentum of the e^+ is calculated for each extrapolation step and the algorithm exits when this condition is satisfied.

It is important to understand how good an approximation this is, and if the radial distribution obtained using the radial tangency assumption is significantly different from the distribution of the actual muon decay radii to make correcting for the assumption unfeasable. Extensive studies were performed using simulation to evaluate the usefulness of the radial tangency assumption.

Not all muons decay tangentially; some will emit their e^+ outwards (away from the detectors), and others inwards. In the outwards case, the e^+ will initially travel to high radius, but due to the magnetic field will then reach some maximum radius and then change direction to curve inwards towards the detectors. The radial component of the e^+ momentum will be 0 at the turning point of this trajectory and this will be the 'tangent point' returned by the extrapolation algorithm. The radius at the tangent point is hence higher than the true radius of the muon at the point of decay. The extrapolation algorithm will hence over-estimate the decay radius for these types of tracks, but underestimate the azimuthal decay position (equivalently distance travelled by the e^+) since the tangent point is consistently closer to the detectors than the true decay position for outwards tracks. Inwards e^+ are already directed towards the detectors when they are emitted. This means that the algorithm will go beyond the true decay position before reaching the radial tangency point. The azimuthal decay position will hence overestimate the azimuthal decay position for inwards tracks, since the curvature in the magnetic field means that e^+ emitted inwards will never be tangential to the muon orbit radius. However, the radial position will still be an overestimate for these tracks. So, the extrapolation algorithm will overestimate the decay radius consistently for both inwards- and outwards-going positrons. This is referred to as the radial tangency offset.

The size of the radial tangency offset is studied by comparing the distributions of the extrapolated radial decay positions to the true values using simulation. The dependence of the radial tangency offset on track momentum was also studied. It might naively be assumed that low-momentum tracks, which are emitted at larger angles and follow more tightly-curving trajectories in the magnetic field, would reach a higher radial tangency offset than high-momentum tracks, which follow stiff, straighter trajectories and are emitted at smaller angles to the muon momentum direction. However, figure 63 illustrates that this is not the case, and that the radial tangency offset

is in fact independent of momentum. Despite being emitted at low radial angles, high-momentum e^+ travel a greater distance before reaching the radial tangency point than the low-momentum tracks with large angles, and the two effects combine to result in the same radial tangency offset for tracks of all momenta. The difference between true and extrapolated radial positions as a function of track momentum is shown in figure 64, confirming that the size of the radial tangency offset is approximately 1.1 mm, independent of momentum.

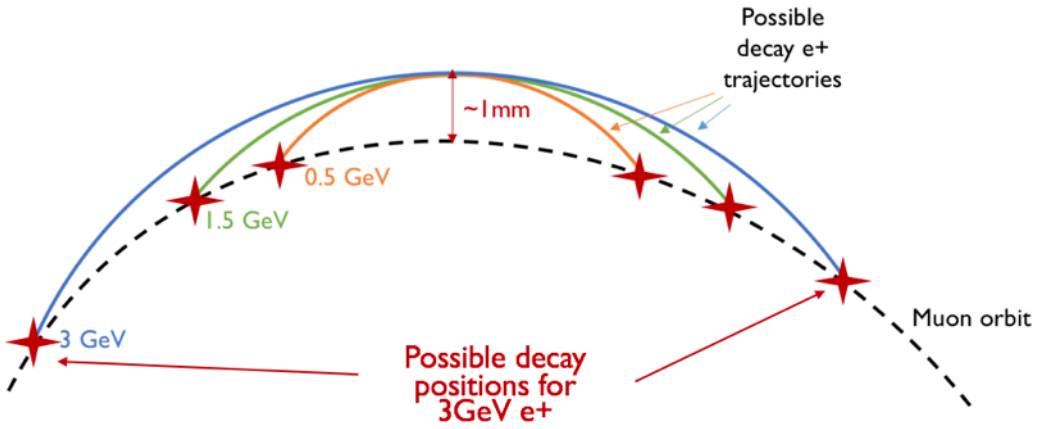

Figure 63: Schematic diagram illustrating the degeneracy between inwards and outwards decays that arises when the point of radial tangency is used as a proxy for the muon decay position, and also the momentum-independence of the radial tangency offset. High momentum tracks, such as the 3 GeV/c track (blue) are emitted at smaller angles and follow stiffer trajectories; however, they travel a greater distance before reaching the radial tangency point than low momentum tracks. Tracks such as the 0.5 GeV track (orange) are emitted at higher angles and follow more tightly-curving trajectories, but since they do not travel as far to the point of radial tangency as high-momentum tracks, tracks of all momenta reach the same radial tangency offset on average.

7.3.1 Momentum independence of radial tangency offset

The relationship between the radial tangency offset and track momenutm was studied extensively in simulation, in order to derive a correction that could be applied to the reconstructed data. Figure 64 shows the radial tangency offset as a function of track momentum for tracks with and without the volume cut applied. When then volume cut has been applied, the radial tangency offset is consistently 1.1 mm for tracks of all momenta. This means that in the real data, a simple 1.1 mm correction can be applied to the reconstructed radial distributions, and no momentum-dependent corrections are required.

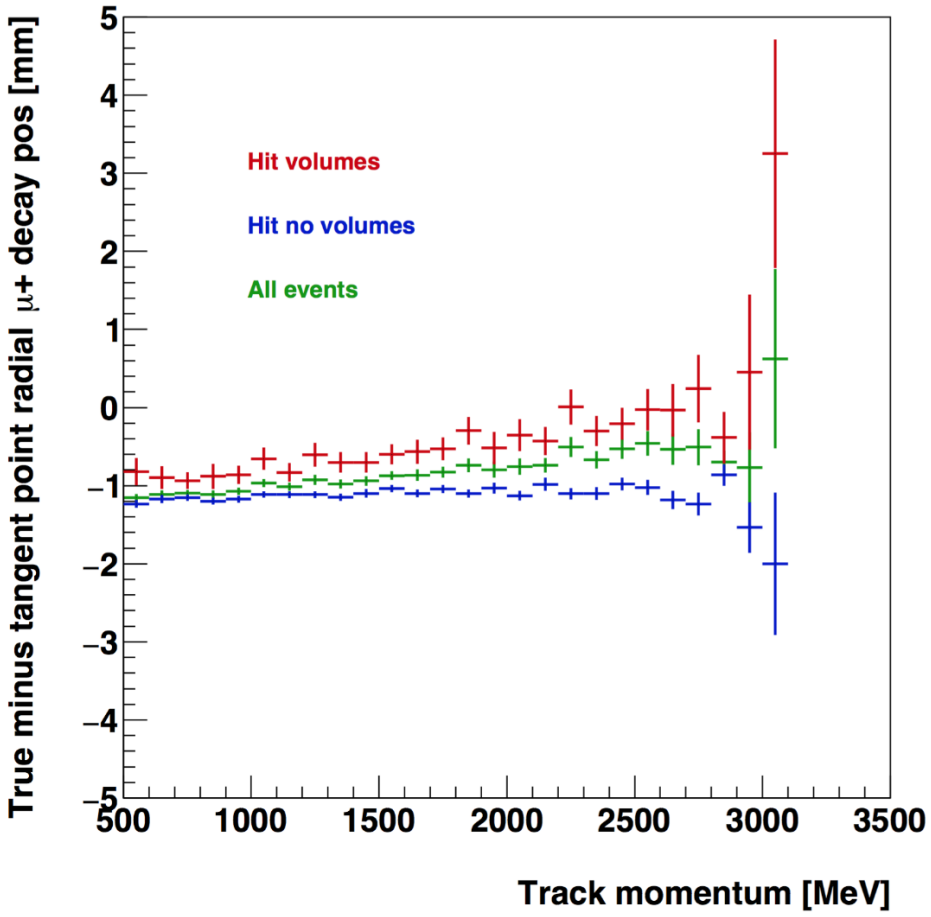

Figure 64: The difference between the true (simulated) radial decay position and the extrapolated radial position at the tangent point, as a function of track momentum for different categories of track. The blue line is from tracks that do not hit any volumes; the radial tangency offset of 1.1 mm is consistent for all momentum tracks after this cut has been applied.

7.4 Summary

The track extrapolation algorithm was extensively tested using Monte-Carlo tracks in order to understand its performance before applying it to real data. By comparing with simulation, the radial tangency offset was found to be momentum-independent and can hence be easily applied to the measured tangent point radial distribution. A procedure for checking the interaction of tracks with material was developed that can be applied to tracks in both simulation and data, in order to only select the highest-quality tracks without imposing cuts that could bias the distributions.

In the next section, the results of distributions obtained during the commissioning stages of the first experimental run will be presented.

Chapter 8

Beam profile measurements using the tracking detectors

The $g-2$ experiment took its first data with all systems installed during a six-week long commissioning run in June and July 2017. During this time, only one station of tracking detectors was installed. This was the first time that all the experimental subsystems had been exercised together, and the first time that any beam had been delivered to the SR.

During the commissioning run, the full chain of upstream beam delivery devices was not yet operational. The delivery ring (DR) was not in use, so the beam was heavily dominated by protons; the kicker magnet to remove them is located in the DR. As such no Physics-quality data was taken, but the run was an excellent test that the experimental hardware was performing as required, while understanding the data recorded by the detector systems was an invaluable opportunity to train reconstruction and analysis software. The measurements of the straw tracking detectors presented in this chapter proved very useful during this run.

The first official experimental run began in November 2017. The first few months of this run were spent optimising the beam injection and storage. The quality of the beam delivered to the SR, and the fraction of injected muons that were stored, steadily increased and the experiment is now detecting approximately 500 e^+/fill (the target rate is 1000 e^+/fill). Two full tracker stations were installed prior to this data-taking period. The straw tracker beam profile measurements during these early months are presented in this chapter.

8.1 The 2017 commissioning run

Only the tracking station at 270° (station 18) was installed during the 2017 commissioning run. Figure 65 shows the 'top-down' view of the SR. The tracker location is indicated. The effect of applying the volume cut is clearly illustrated by comparing the two plots with and without the cut. Due to the quality of the beam, nearly all data taken in the commissioning run was from

'lost' protons that did not have the required momentum to remain in the storage region, and so gradually and slowly spiralled in towards the detectors. All tracks were extrapolated to the tangent point unless they followed trajectories that took them through the vacuum chamber wall; this is the reason for the two thin 'bands' of decay points at the inner and outer radii. To avoid spending unnecessary time extrapolating lost particles around the ring several times, a distance cut of 10m was imposed. After the volume cut has been applied, the tracks that remain all originate from close to the magic radius.

The radial and vertical beam distributions measured during the commissioning run are shown in figure 66. Different cuts have been applied to the distributions, which are all area-normalised to 1. The radial distribution without any cuts applied (orange) is heavily dominated by lost particles at low radii. When the volume cut is applied, a peak in the storage region becomes apparent (yellow). The loosest volume cut has been applied here, and tracks that pass close to volumes have not been removed, so this distribution still contains some events from lost particles. Applying a momentum cut of $p_{e^+} < 2.5$ GeV/c removes more lost particles and the combination of these two cuts provides the sharpest resolution of the radial beam profile in the storage region, with only a small peak at the low radius remaining.

8.2 Measurements of the beam profile in data from January - March 2018

The first Physics run of the $g-2$ experiment began in November 2017. The first few months of this time were spent optimising the beam storage. The beam quality delievered to the SR from the upstream beamlines increased throughout this time, both in purity of muons and also in momentum spread. This provided increasingly useful conditions in which to tune the kicker strength, kicker timing and ESQ voltage for optimal muon storage.

In the early stages of this optimisation period, the tracking detectors proved an invaluable tool for diagnosing the effect of the storage devices and injection conditions on the distribution of the stored beam. Clear differences in the beam position and CBO parameters were observed with different running conditions. The measurements of the beam profile agreed with those made by the fiber harps and fast rotation analyses. Furthermore, stable operation of the tracking detectors throughout the entire data-taking period allowed uniquely detailed measurements of the CBO frequency, amplitude and lifetime.

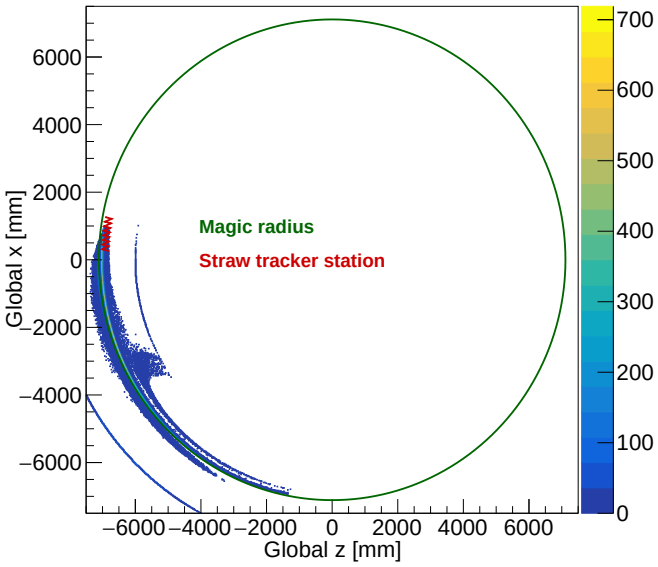

(a)

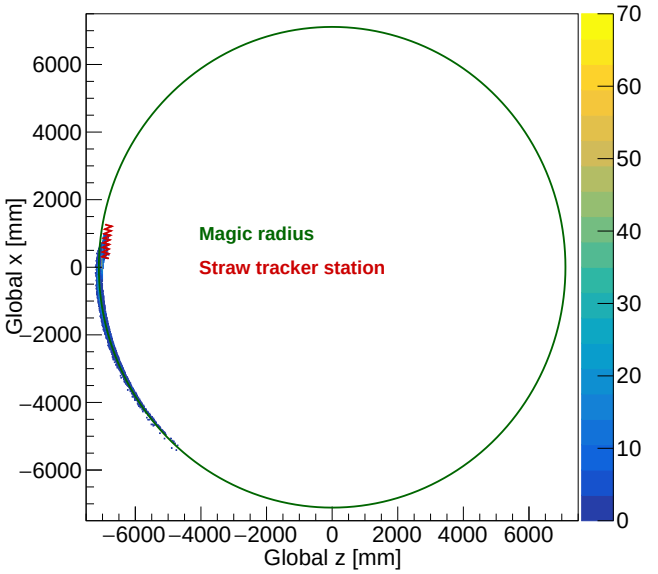

(b)

Figure 65: 'Top-down' view of the SR showing the extrapolated decay positions. The tracker location is indicated in red. Plot (a) shows all data and plot (b) with the volume cut applied.

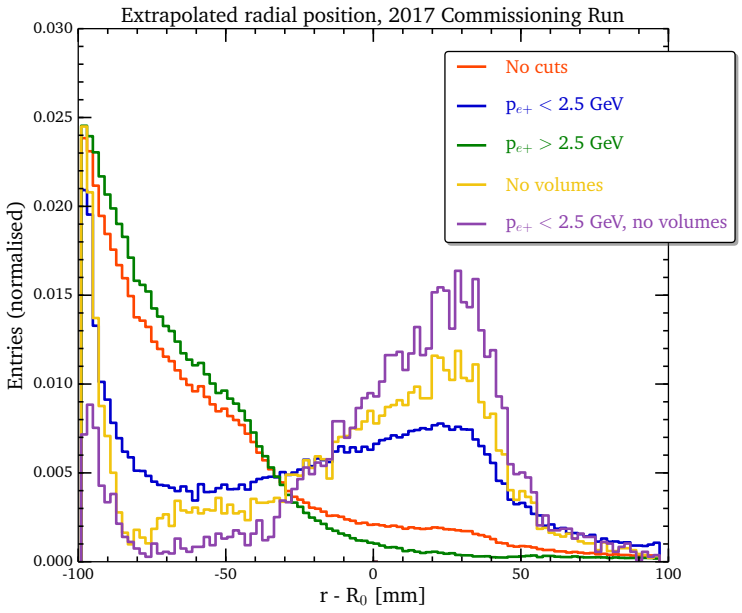

(a)

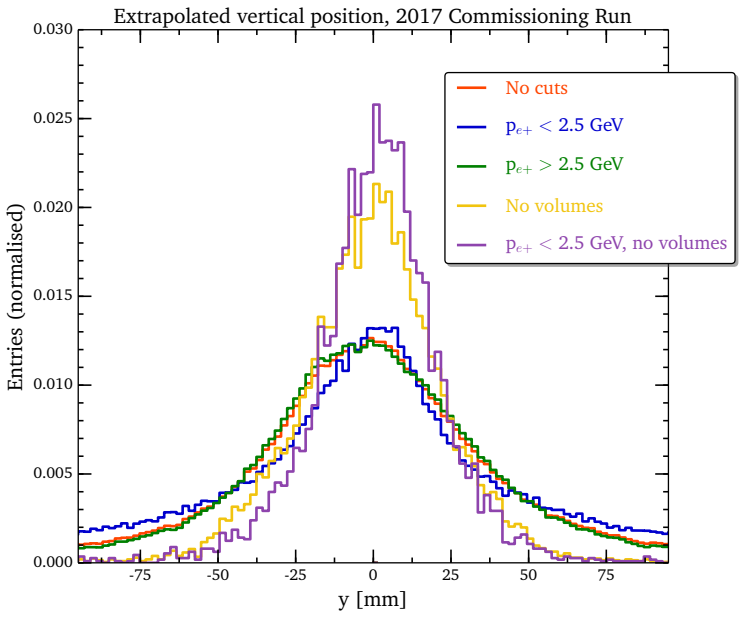

(b)

Figure 66: The plot illustrates the (a) radial and (b) vertical distribution of extrapolated tracks at the tangent point measured during the 2017 commissioning run. Different cut types have been applied and their effect on the quality of the distribution is evident. A momentum cut of $p_{e^+} < 2.5$ GeV was applied to minimise contamination from 'lost' muons and protons, which dominated the data at this early stage of the experiment. Removing events that pass through material, using the procedure described in section , improves the resolution of the e^+ from stored muons significantly.

In this section, results from three different datasets are presented. Each dataset is from a period of uninterrupted stable running, but the run conditions for each dataset were different. The most important differences were the kicker strength and the magnetic field surface coil settings.

- **Dataset A:** kicker voltage = 55 kV[6], simple surface coil settings (no multipole correction)
- **Dataset B:** kicker voltage = 60 kV[7], optimised surface coil settings with multipole correction
- **Dataset C:** kicker voltage = 55 kV[8], optimised surface coil settings with multipole correction

8.2.1 Beam position for different run conditions

The radial and vertical beam distributions for all three datasets are shown in figure 68. The vertical distribution is centered about y=0 mm and changes little between the datasets. There are several features of the radial distribution to discuss. Firstly, the distributions of datasets A and C (both with kicker voltage = 55 kV) are almost identical, while the distribution for dataset B (kicker voltage = 65 kV) has a slightly different shape and is peaked at a slightly lower radius. The measurement of the beam's high radial position agreed with the radial position distribution obtained from the fast rotation analysis. The two-dimensional distributions, with and without the volume cut, are shown in figure 70.

The small peak at r - R_0 = -100 mm is an artefact of the tracker acceptance. The momentum distribution for all three runs, shown in figure 69 illustrates the amount of lost muon contamination in each dataset. The image of the trackers inside the ring, figure 67, shows a number of support materials in the SR that can obstruct the path of tracks from the storage region to the detector. Lost muons have typically high momenta and follow stiff trajectories with a small radius of curvature. They have a high probability of hitting a volume, and so most lost muon events are removed by the volume cut. However, a small vertical slice is free for lost muons to pass through - these are the events that make up the low radius peak. The lower momentum positrons have a higher probability of avoiding these structures since they follow highly curved trajectories and so many of them can bend around the bellows rails and still hit the tracker.

[6]The kicker strengths quoted here are those recorded at the time of data taking. Since then, the kicker strength was recalibrated, and the actual kicker strength here is closer to 40 kV. The strengths recorded at the time of data collection are quoted for ease of reference, but should not be quoted as official values of kicker strength. The relative, rather than absolute, strength is important for the tracker studies presented here.

[7]See 6

[8]See 6

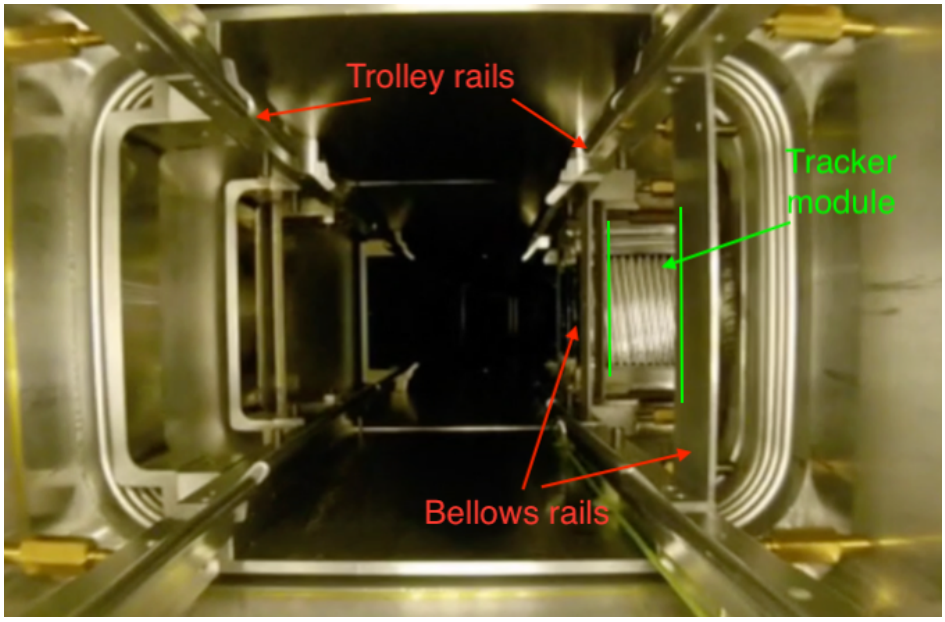

Figure 67: A picture taken from inside the SR illustrating the gap between bellows rails through which lost muons can pass.

8.2.2 Coherent Betatron Oscillations

It was explained in chapter 3 that the betatron motion of the beam can result in an apparent oscillation in the radial beam position measured by a stationary detector at a similar frequency to ω_a. This is referred to as a Coherent Betatron Oscillation (CBO). Since the tracking detectors monitor the radial position of the beam continuously throughout the muon fill, they can measure the frequency, amplitude and lifetime - often referred to as decoherence time - of the CBO for every run. The ability to compare CBO parameters between runs proved extremely useful during the commissioning part of the data-taking, since the ESQ voltage, kicker strength and alignment, and injected beam parameters can all have a significant effect on the CBO. The parameters must be known in order for the CBO to be accurately accounted for in the five-parameter fit for the final ω_a analysis.

Figure 71 introduces the tracker-based CBO analysis. Part (a) of the figure shows the raw 2D histogram of radial beam position as a function of time in the fill, for the range 50 – 100 µs. The oscillation in radial position is immediately clear, but further analysis is required to characterise it. Part (b) of this figure shows the *average* radial position as a function of time, for the longer range 50 – 220 µs. The reduction in oscillation amplitude over time is evident from this plot; an

'envelope' function is apparent as the oscillation dies away. The early and late times of this plot have been fitted with a cosine to obtain the frequency and amplitude at different times in the fill. Examples of such fits for datasets B and C are shown in figure 72 and 73 respectively.

By fitting the mean radial position for different time periods and plotting the amplitude of the oscillation as a function of time, the speed at which the oscillation dies away can be approximately measured. This is called the 'decoherence time' and is an important quantity to know; in the ideal case, the CBO would die away quickly and hence affect a smaller fraction of the ω_a data. The amplitude as a function of time for each dataset are presented in figure 74. The amplitudes were obtained by fitting different cosines to consecutive 10 μs slices of the full oscillation - the same time window used in figures 72 and 73. There are clear differences between the three runs. Dataset B – with the highest kicker voltage – has the lowest initial amplitude, but the longest lifetime of $\tau_{CBO} = 414.89$ μs in station 18. Dataset C has a significantly higher initial amplitude, but a much shorter lifetime of $\tau_{CBO} = 180.93$ μs in station 18. Station 18 is situated 90° further around the ring than station 12 and so the observed phase offset of 90° is expected.

All of the information presented so far can be used to select optimal running conditions. The radial beam distribution of dataset B is peaked at a slightly lower radius than in dataset C; this is important since the beam should be as central as possible in order to simplify the convolution with the magnetic field map, which is most uniform in the central region and has almost symmetric multipoles about R_0. Also, the lost muon peak in the momentum distribution in figure 69 is smaller for dataset B than dataset C; reduction in the lost muon contamination is favourable to reduce their systematic effect on ω_a. On the basis of this information it might seem that the conditions in dataset B are preferable to those in dataset C. However, the short CBO lifetime in dataset C means that accounting for the CBO systematic will be much more straightforward in these running conditions. All of these effects must be considered when optimising the running conditions; as such the tracking detectors are invaluable for successful commissioning of the beam.

Another important oscillation to consider is that of the width of the radial distribution as a function of time. As well as the oscillation of the beam centroid about the equilibrium orbit, betatron oscillations cause the beam width to vary during the fill in a process known as 'breathing'.

Part (b) of 75 illustrates this feature. The first part of the plot shows the radial distribution of the beam at the 'trough' of a CBO period, and the second part shows the radial distribution at half a CBO period later; the mean has shifted to a higher radius, and the width has reduced significantly. The width of the distribution is plotted as a function of time for the range 50 - 220 μs in figure 76, and in figure 75a (a) the first 50 - 60 μs have been fit with a cosine to obtain the frequency and initial amplitude. The width oscillates at the same frequency as the mean radial position.

Figure 76 illustrates an important feature of the beam in the running condition in dataset B. While the oscillation in the width of the beam becomes difficult to observe at later times, the average width of the beam appears to increase throughout the fill. This effect can introduce a serious systematic effect on the ω_a analysis, since the width of the beam can lead to differences in the frequency measured in different vertical or horizontal slices of the calorimeters. The increasing width throughout the fill could therefore result in a different measured frequency at different times in the fill - a so-called 'early-to-late' effect. If the increase in width cannot be mitigated by careful choice of run conditions, the measurements made by the tracking detectors will be crucial in order to properly account for this systematic uncertainty, since the rate of increase in the beam width can be measured for all times in every run. This information can be included in the ω_a analysis to minimise the uncertainty due to this effect.

8.2.3 Summary

The results presented in this section illustrate the wide range of beam parameters that can be measured using the tracking detectors. The trackers can measure the position of the beam as a function of time throughout the fill in order to measure the CBO parameters that must be included in the ω_a fit. Comparing the measurements of the trackers with those made by the fiber harps is a good cross-check of the detector performance, and the radial position and CBO frequency measured by both detectors agree. The usefulness of the ability to measure the CBO parameters, the beam position and beam width as a function of time throughout the fill for every run has been demonstrated. The behaviour of the muon beam is difficult to control, and any variations in these parameters on a run-by-run basis can be accurately accounted for, enabling mitigation of any systematic effects caused by changes in the beam distribution.

In the next chapter, a different use for the tracking detectors is presented - a search for os-

cillations in the average vertical decay angle of the positrons indicative of a muon electric dipole moment (EDM).

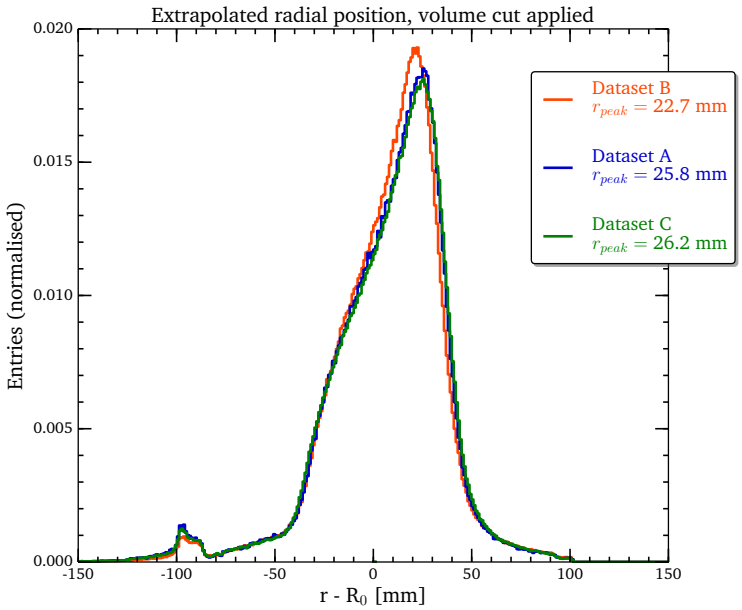

(a) Radial distribution for different runs.

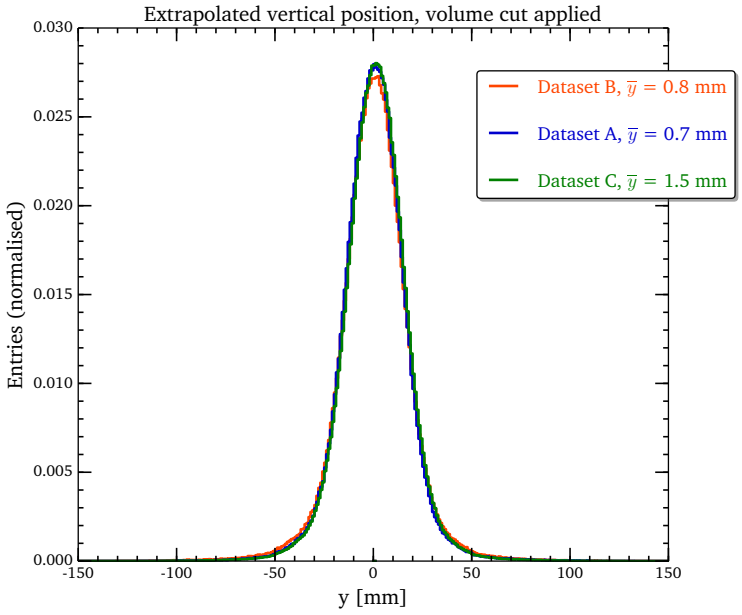

(b) Vertical distribution for different runs.

Figure 68: The plots show the radial and vertical distributions at the extrapolated point of radial tangency for different run conditions.

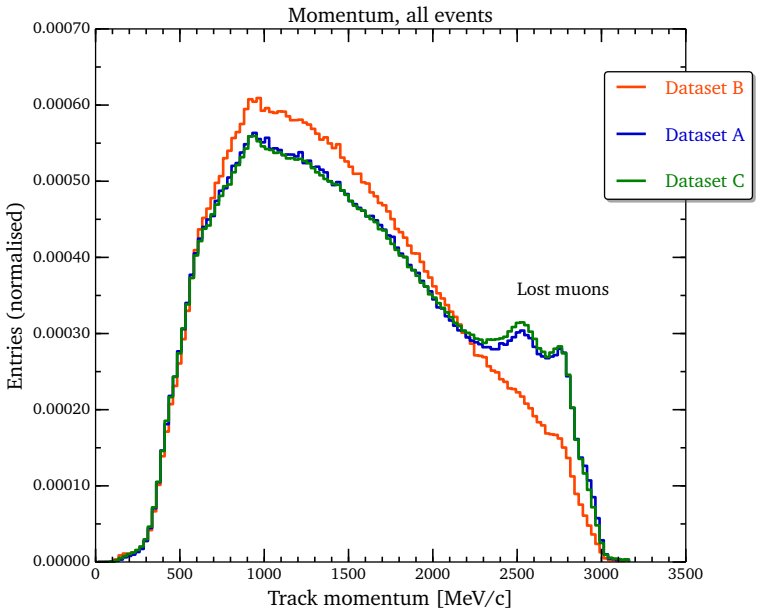

(a)

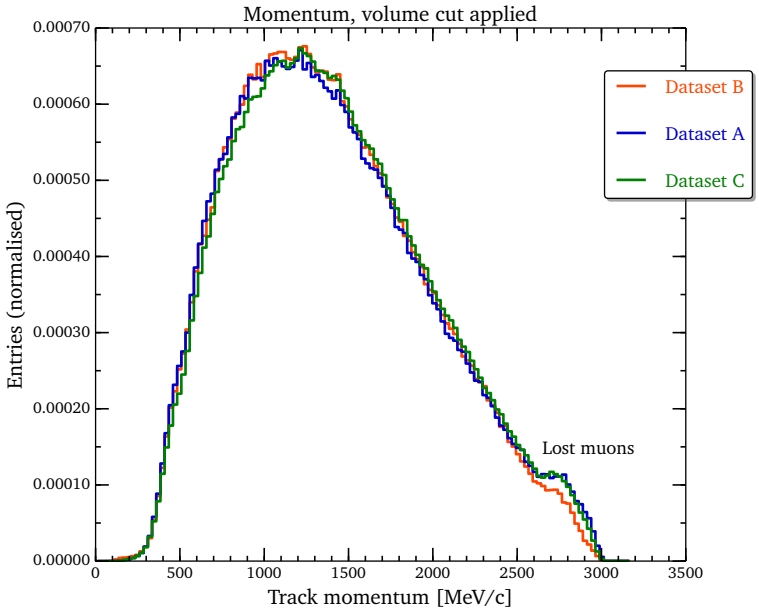

(b)

Figure 69: The plots show the momentum distribution for the different datasets, for all events (a) and for only those events that pass the volume cut (b).

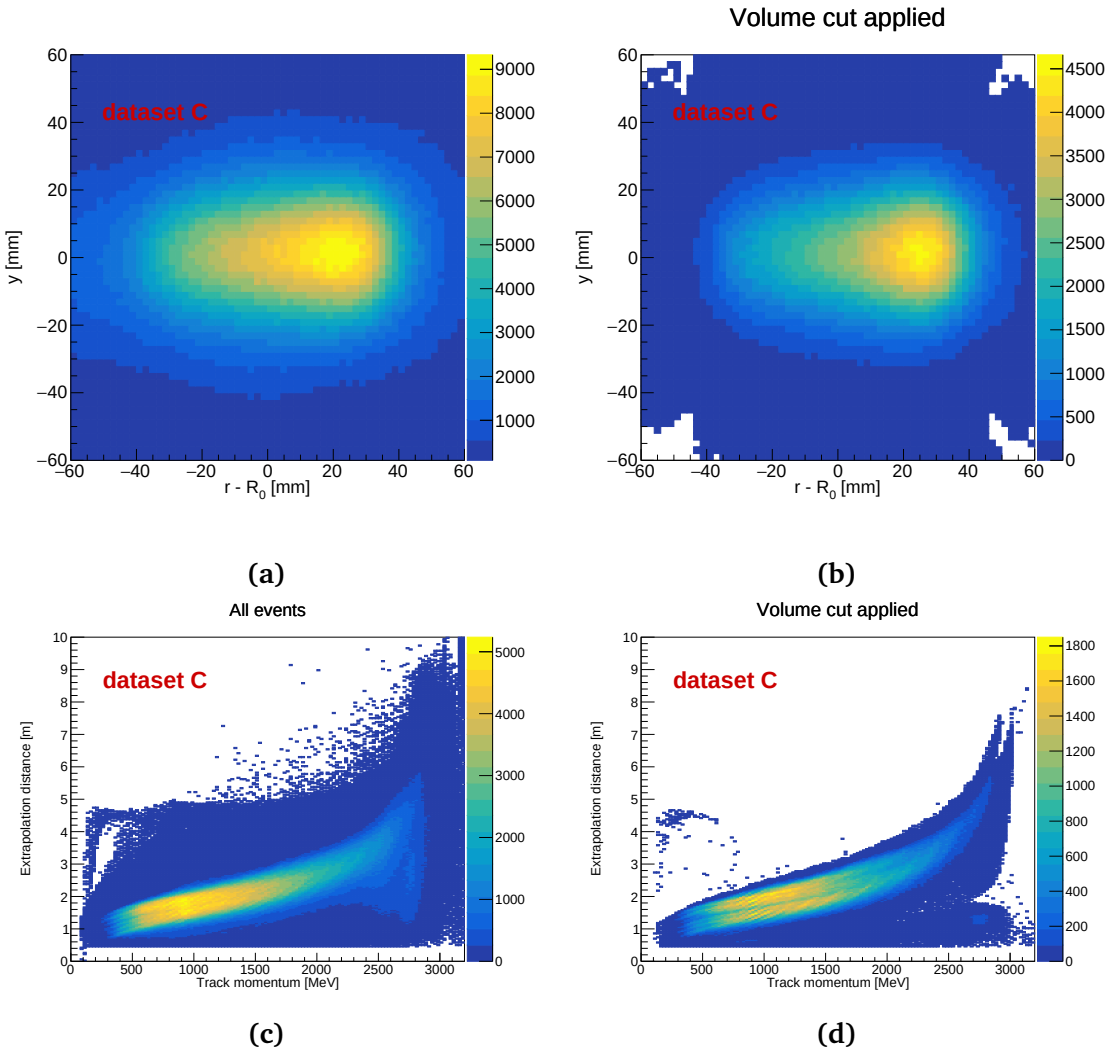

Figure 70: The figures illustrate different aspects of the beam distribution with and without the volume cut applied. Plots (a) and (b) show the beam profile with (a) no cut applied and (b) the volume cut applied. When the cut is applied, the resolution of the beam spot is improved and many of the poorly reconstructed tracks at low radius are removed. The empty regions in the corners of plot (b) show where tracks that hit the trolley rails have been removed. The tails in the distributions are likely from tracks that passed close to volumes in the reconstruction but in reality should have hit that volume. The tails are expected to reduce significantly when the stricter volume cut has been applied. In plots (c) and (d), the extrapolation distance is plotted as a function of track momentum. The expected shape of this distribution in simulation was shown in figure 28a. Applying the volume cut removes the majority of events that do not obey the expected relationship between distance and momentum, but some high-momentum tracks that travel a small distance remain - these are likely to be lost muons.

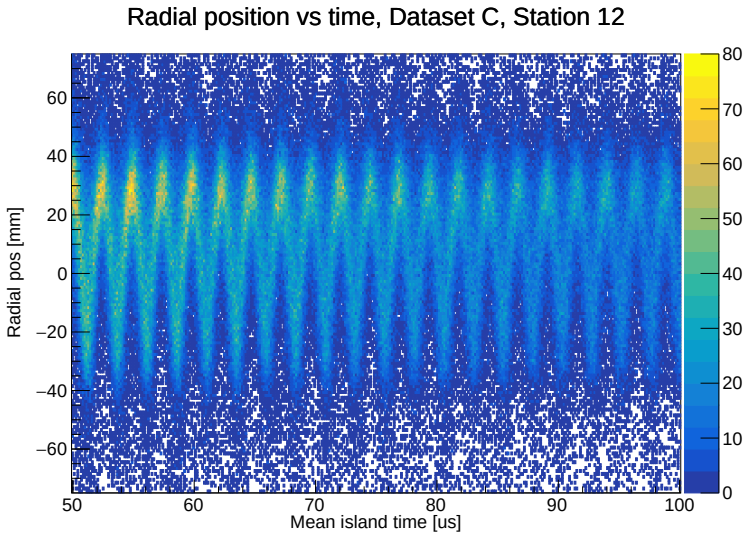

(a)

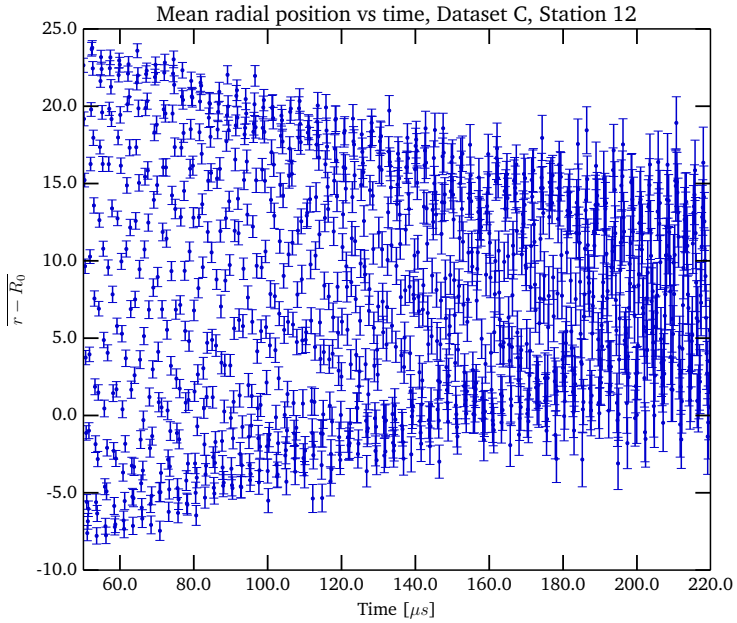

(b)

Figure 71: Plot (a) shows the radial position as a function of time for the station 12 tracker. Plot (b) shows the mean of this distribution for the range $55 < t < 220$ µs. The reduction in the amplitude of the oscillation during the fill is evident from plot (b) where an envelope function is emergent. Both plots are from dataset C.

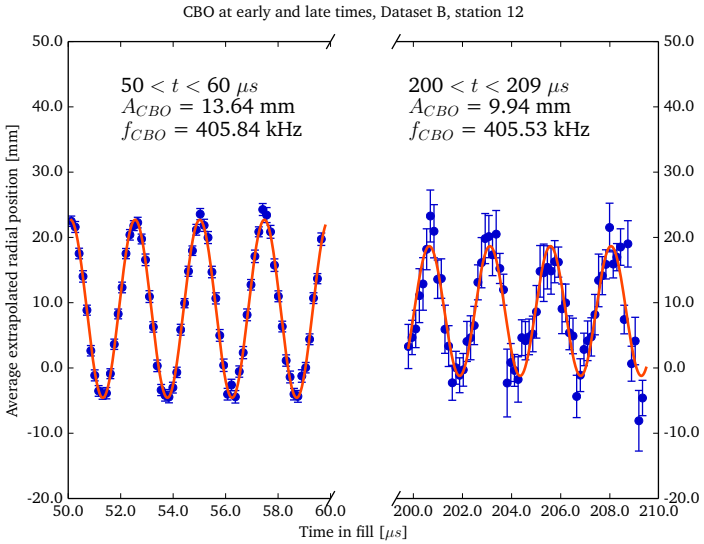

(a) Dataset B, Station 12

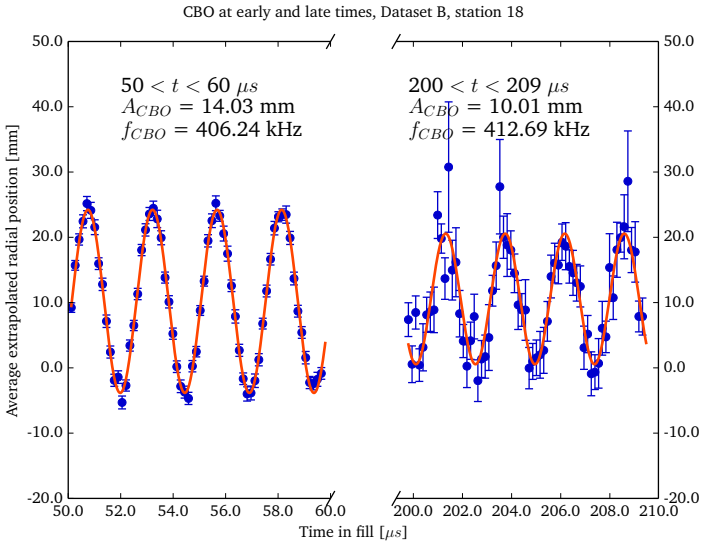

(b) Dataset B, Station 18

Figure 72: The CBO oscillation measured by the tracking detectors for early times (50 - 60 µs) and late times (200 - 210 µs) for dataset B.

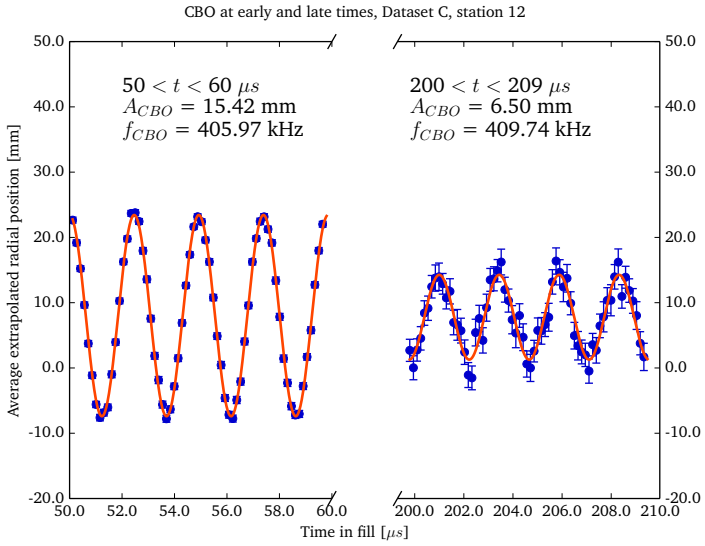

(a) Dataset C, Station 12

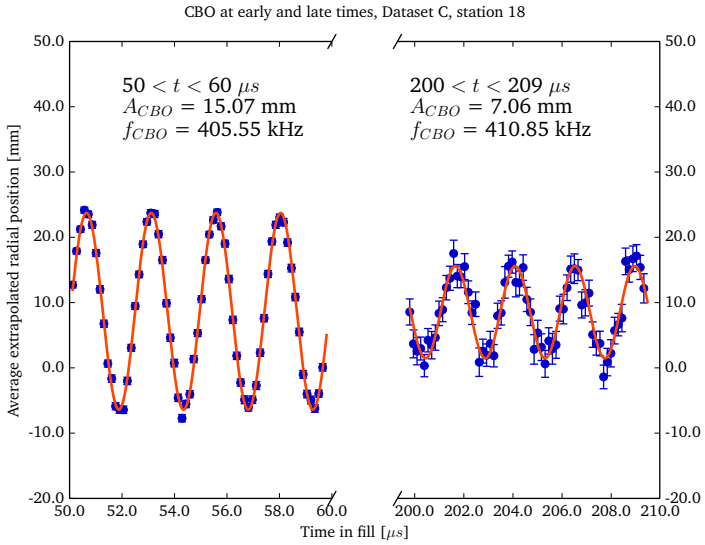

(b) Dataset C, Station 18

Figure 73: The CBO oscillation measured by the tracking detectors for early times (50 - 60 µs) and late times (200 - 210 µs) for dataset C.

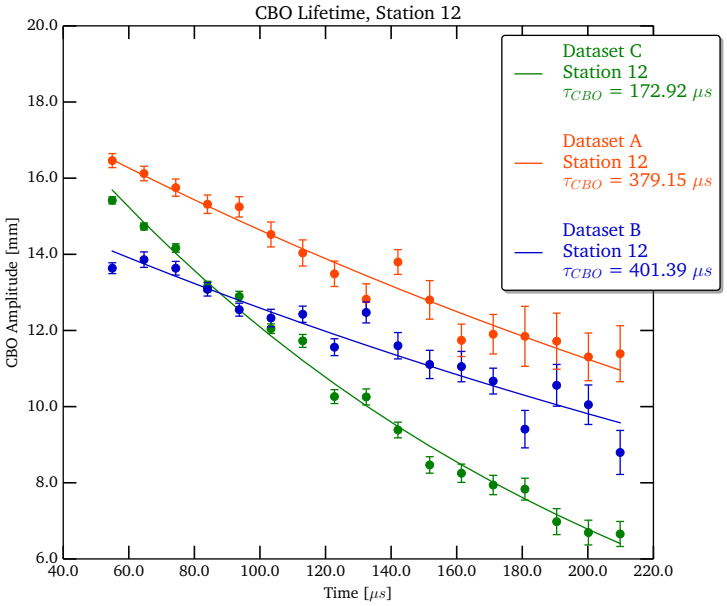

(a) Station 12

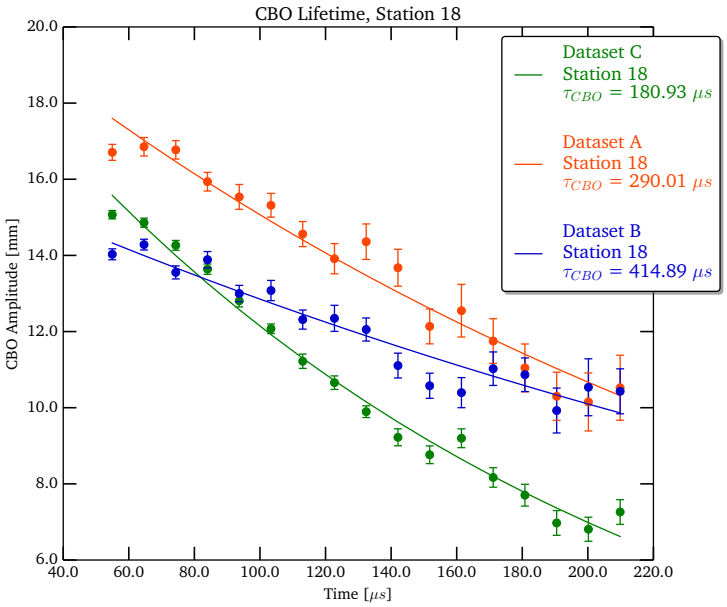

(b) Station 18

Figure 74: The plots show the amplitude of the CBO as a function of time in the fill for the different datasets. Each amplitude was obtained by fitting a cosine to a 10 µs slice of the data, as in figures 72 and 73.

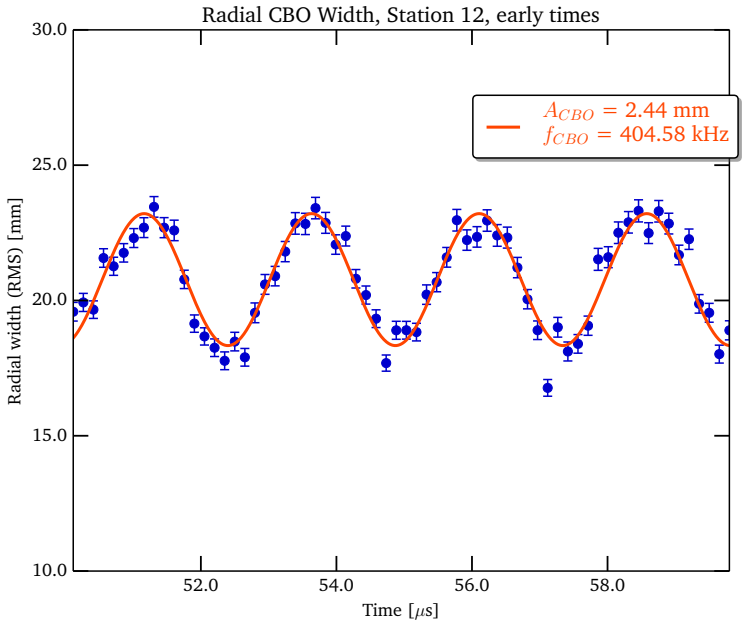

(a)

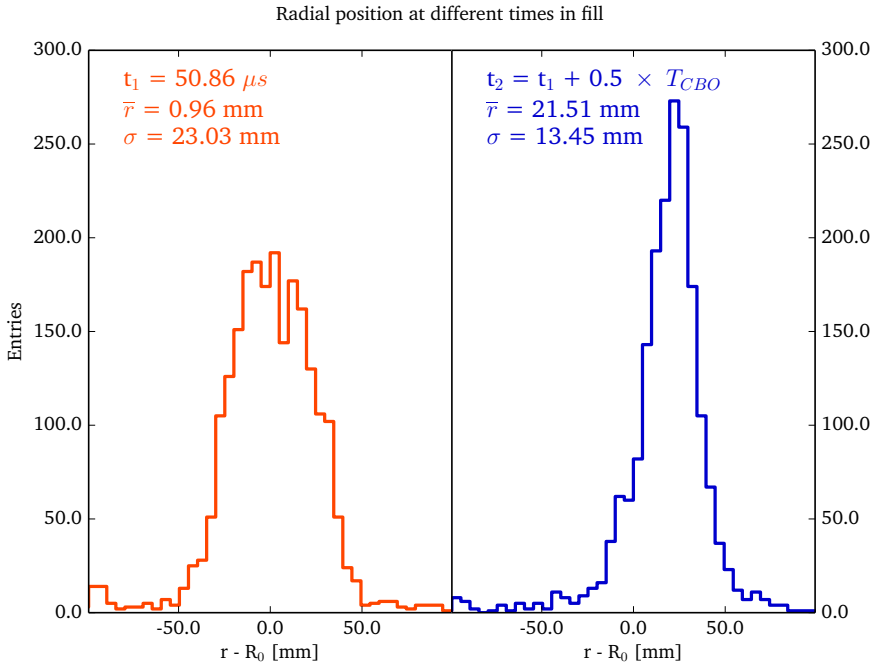

(b)

Figure 75: The width of the radial position distribution changes significantly during a single CBO period. In plot (b), the blue distribution represents the radial beam profile at approximately half a CBO period later than the orange distribution; the width and mean of these two distributions differ clearly. By fitting these distributions for all times, the mean and width of the CBO can be obtained. While the oscillation in the mean is clear up to ~ 220 µs, the oscillation in the width dies away more quickly. It is shown for early times in plot (a).

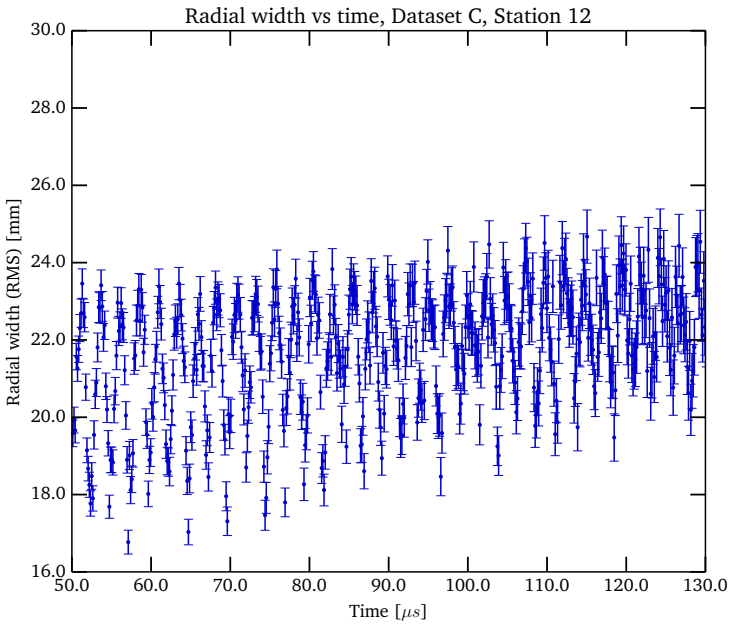

Figure 76: The plot shows the width of the radial distribution as a function of time using Dataset C. The oscillation at the CBO frequency is evident at early times but becomes difficult to distinguish later in the fill. However, an increase in the average beam width during the fill is evident. The width of the beam directly affects the calorimeter measurements, and any changes in the beam width throughout the fill must be included in the ω_a fit in order to account for this 'early-to-late' systematic effect. This measurement by the straw trackers was a crucial observation during the tuning phase of the experimental run.

Chapter 9

Muon EDM Simulation

The final section of this thesis will focus on studies performed using simulated data of the sensitivity of the Fermilab $g-2$ experiment to observing a non-zero muon EDM. As discussed in chapter 3, the world limit on the size of the muon EDM was placed by the Brookhaven experiment. The measurement techniques used to place the BNL limit were also presented in chapter 3, with a discussion of the relative sensitivities of the different analysis techniques. Since the tracker-based method is the only technique to search for the EDM oscillation directly, and this technique was highly statistically limited in the BNL experiment, this is the most likely area for improvement in the new experiment, since both the resolution and the statistical capabilities of the new tracking detectors vastly outweigh those of the traceback system in BNL. However, since the segmentation of the calorimeters means they have improved spatial resolution compared to the detectors used in the BNL experiment, the systematics are expected to reduce slightly for this technique also.

The first part of this chapter will explain the development of the EDM simulation, and some comparison of MC truth information with calculated values to verify the simulation was performing correctly. Early studies using this simulation were performed before the track reconstruction algorithms had been developed, and so an early study using calorimeter truth information only was performed. This used unphysically large EDM values to avoid the need to generate large amounts of MC data to check if the simulation was working.

After this initial study, the track extrapolation algorithm was developed, and recently a new study has been performed using a simulated dataset with a large EDM value of $d_\mu \approx 30 \times d_\mu^{\mathrm{BNL}}$. With this size of EDM, a clear signal using reconstructed tracks was present in the MC data with moderate statistics. Further analysis is required, but the early results from this short study show that the track extrapolation is working well enough that the detectors are sensitive to an EDM comparable to the current limit with a very small dataset, indicating that with the expected number of tracks recorded by the tracking detectors, a significant reduction in the limit can be expected.

9.1 Simulating a muon EDM

The facility to generate datasets with a muon EDM of any size was added into the main $g-2$ simulation, `gm2ringsim`. `gm2ringsim` has two types of particle 'gun' to generate data using `GEANT4`; a 'beam gun' which propagates muons around the ring from the inflector, and a 'gas gun', which immediately creates and decays muons at random locations around the ring based on an initial distribution. The gas gun is much faster at generating a large sample of positrons that enter the detectors, and so the EDM was implemented into this version of the simulation.

The gas gun works by sampling from a distribution of muon phase space at the inflector exit. The position, momentum components and polarization direction of the muon is calculated at a random time t, and the muon is born, and instantly decays, with the parameters calculated at that time. The decay positron is born immediately and its path tracked until the death of the particle, usually when it enters the calorimeter. The EDM is added as a time-dependent addition to the vertical polarization component.

The tilt angle and frequency ω_η for a given EDM magnitude are calculated using the expressions in equation 3.48. The direction of $\boldsymbol{\omega}_\eta$ is rotated, so that it always points perpendicular to $\boldsymbol{\omega}_a$, and always points either inwards (towards the centre of the ring) or outwards, depending on the sign of the input $\boldsymbol{d}_\mu$. The increased precession frequency $\boldsymbol{\omega}_{a\eta}$ is calculated via vector addition (see equation 3.46), and this is the frequency that is used to calculate the position, momentum and polarization vectors of the muon at the time it will decay.

To test that the simulation is working as intended, the polarization vector of the muon in its rest frame can be studied as a function of time. In the absence of an EDM, the radial polarization vector should oscillate with the frequency ω_a, but there should be no polarization at all in the vertical direction, since $\boldsymbol{\omega}_a$ always points perpendicular to $\boldsymbol{B}$, which is vertical in the storage region. With a large EDM, however, there should be a clear oscillation in the vertical polarization component, at the frequency $\omega_{a\eta}$ and with amplitude equal to the size of the tilt angle in the MRF, according to equation 3.46.

The radial (x) and vertical (y) components of the polarisation vector $\boldsymbol{s}$ in the MRF as a function of time, with $d_\mu = 0$ and $d_\mu = 30 \times d_\mu^{BNL}$, are shown in figure 77. The amplitude of the oscillation in

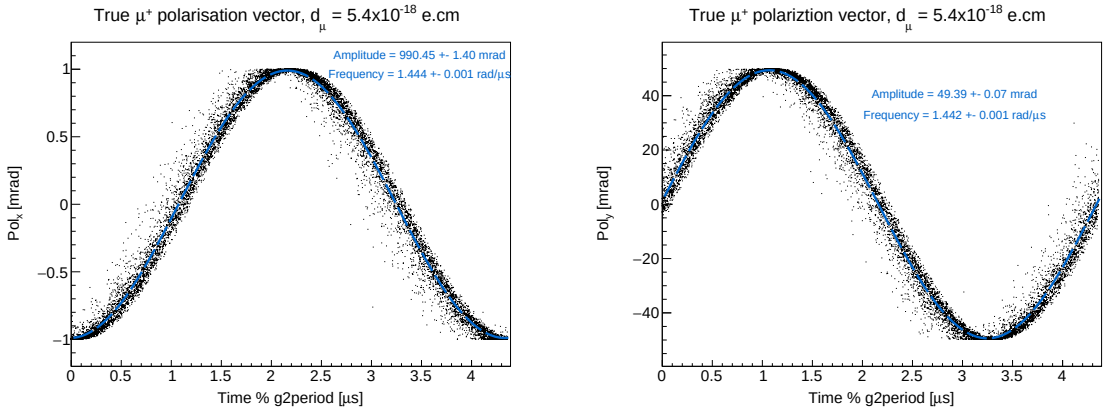

(a) **(b)**

Figure 77: The x (radial) and y (vertical) components of the muon polarisation vector for a simulated dataset with $d_\mu = 5.4 \times 10^{-18}\ e \cdot \text{cm}$.

the large EDM dataset is $A = 49.39 \pm 0.07$ mrad, which is in good agreement with the analytically calculated tilt angle for this EDM value, $\delta = 49.75$ mrad. A summary of the simulated amplitudes in the oscillations of $\boldsymbol{s}_y$ in the MRF for different values of d_μ, compared to the analytically calculated tilt angles, is shown in figure 78, and demonstrates that the simulation is generating muons with the expected behaviour.

9.2 Verifying the simulation with the calorimeter method

Before the tracking algorithms were developed, the only way to verify that the simulation was generating e^+ with the correct vertical angle components was to analyse MC data using the calorimeter method. Three datasets were generated:

- $d_\mu = 1.0 \times 10^{-16}\ e \cdot \text{cm}$; N events = 988170
- $d_\mu = 1.8 \times 10^{-17}\ e \cdot \text{cm}$; N events = 915208
- $d_\mu = 2.0 \times 10^{-18}\ e \cdot \text{cm}$; N events = 1052765

The purpose of generating datasets with such unphysically large values of d_μ was purely to see that the expected amplitude and frequency of oscillation were obtained when analysing the decay positrons. The precession frequency is altered significantly by these values, and the severity of the tilt is likely to affect other properties of the beam and potentially the acceptance of the detectors. As such these were purely used for verification purposes rather than detailed studies.

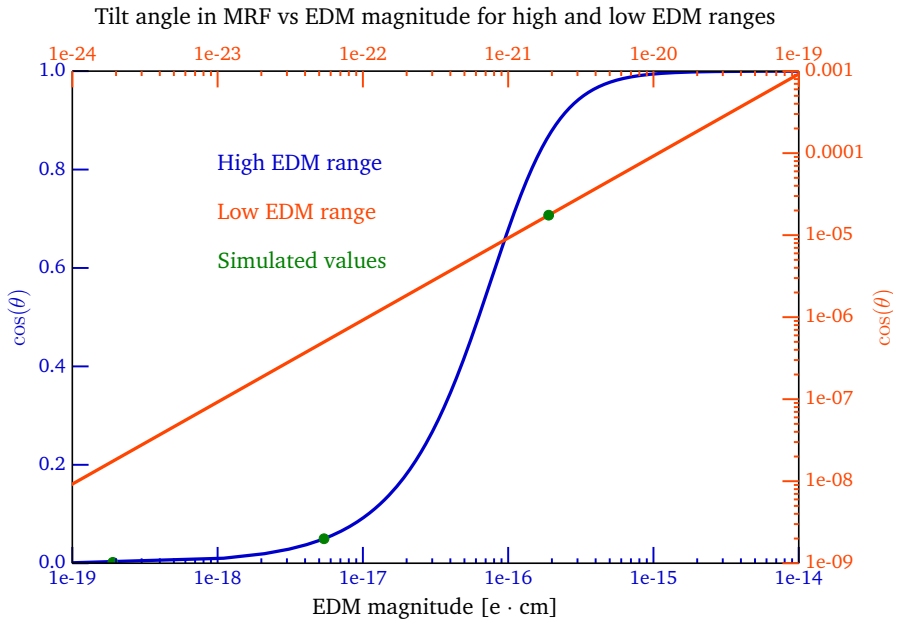

Figure 78: Simulated tilt angles for different EDM values compared to the analytically calculated angles.

The data was divided into e^+ hitting the top and bottom halves of the calorimeters, and the fraction $N_\pm$ was obtained according to equation 3.52. $N_\pm$ for each dataset was plotted against the modulo of the analytically calculated precession frequency for the corresponding d_μ value. The plots are shown in figure 79, and the measured values of amplitude and frequency are displayed in table 3, alongside the analytical values.

The first three plots in figure 79 are out of phase with the wiggle plot in part (d), illustrating that the oscillation observed is due to the EDM; no oscillation is apparent in the plot of the $N_\pm$ oscillation for a dataset with $d_\mu = 0$, which was generated with the same conditions as the large EDM datasets. The frequencies obtained from a 5-parameter fit to the wiggle plots for these datasets are in good agreement with the analytical values shown in table 3. The increase in precession frequency observed in the simulation agrees with the analytically calculated increase. However, there is a discrepancy of $\sim 10\%$ between the calculated and measured tilt angles. This factor arises from the fact that e^+ of different energies have different probabilities of carrying the EDM signal (as explained in chapter 3). In the BNL analysis [2, 81], the asymmetry factor was accounted for by simulating different EDM datasets and deriving the relationship between

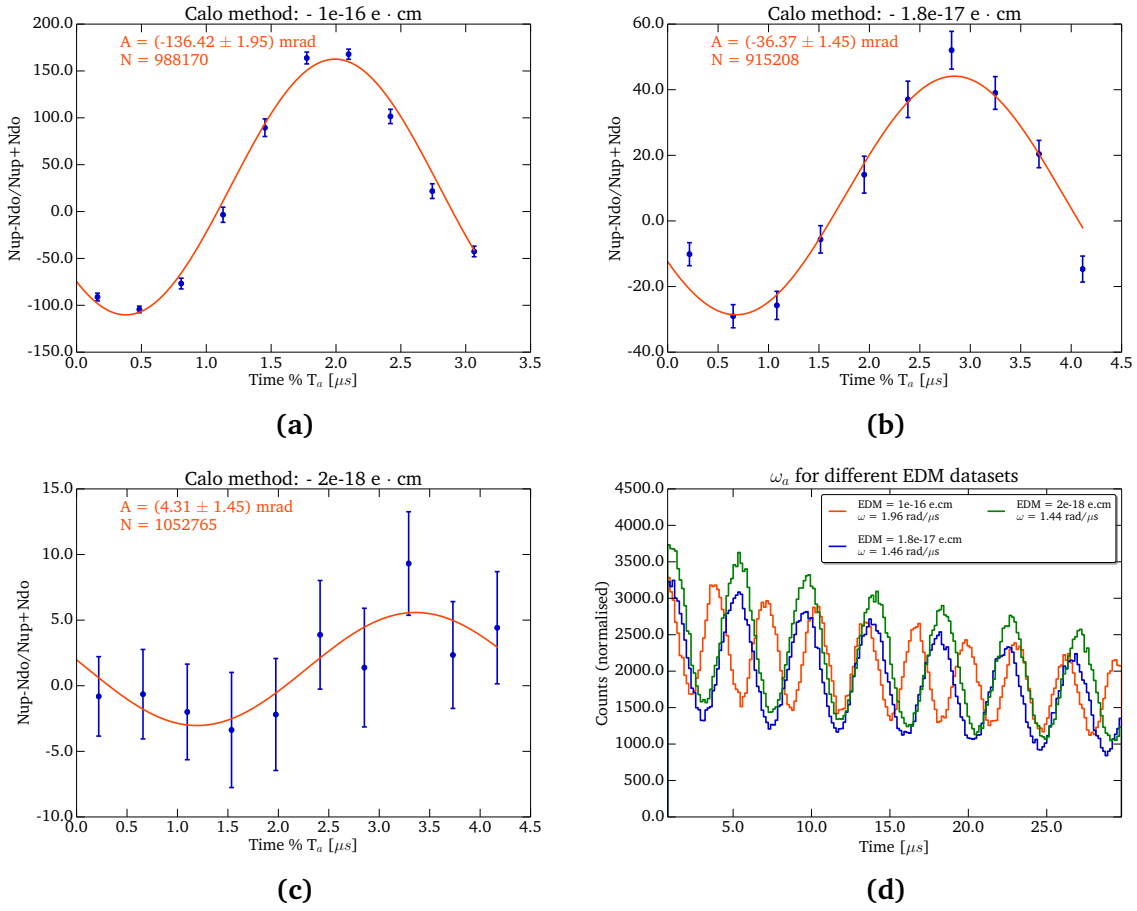

Figure 79: Plots of the EDM signal in the calorimeters for (a) $d_\mu = 1.0 \times 10^{-16}\ e \cdot \text{cm}$, (b) $d_\mu = 1.8 \times 10^{-17}\ e \cdot \text{cm}$ and (c) $d_\mu = 2.0 \times 10^{-18}\ e \cdot \text{cm}$. Plot (d) shows the wiggle plot for each dataset, which was fit to obtain the frequency $\omega_{a\eta}$. The frequency from the fit to (d) was used to fix the period for the modulo plots (a) (b) and (c).

d_μ ($e \cdot$ cm)	$A_{meas.}$ (mrad)	$\omega_{meas.}$ (rad/ns)	δ_{true} (mrad)	ω_{true} (rad/ns)
1.0×10^{-16}	136.42	0.00196	31.5	0.00195
1.8×10^{-17}	36.37	0.00146	5.66	0.00145
2.0×10^{-18}	4.31	0.00144	0.629	0.00143

Table 3: The measured oscillation parameters and their corresponding analytical values. d_{true} is the Lorentz boosted angle in the detector frame.

δ_{meas} and δ_{true} from the observed results. It was found that every 1 mrad of precession plane tilt corresponded to a 3 µrad vertical oscillation in the tracking detectors, and an EDM magnitude of $d_\mu = 1.092 \times 10^{-19}\ e \cdot$ cm. However, an attempt to analytically derive the value of the asymmetry factor can be made by considering the effect of different momentum cuts on a particular dataset.

9.3 Vertical angle oscillations in the tracking detectors

A dataset with $d_\mu = 5.4 \times 10^{-18}\ e \cdot$ cm was generated in order to study the sensitivity of the tracker-based analysis technique. This is just over 30 times larger than the BNL limit. The was the first ever study of the ability of the tracking detectors to search for an EDM signal. In addition, a range of different momentum cuts were applied to the dataset in order to consider the asymmetry effects that can affect the measured value of δ. Events with very high or very low momentum carry less of the EDM signal. Events with high momentum are usually emitted in the forwards direction; forwards events are less likely to have any of the vertical polarisation component since the tilt is perpendicular to the momentum direction. The spin-momentum correlation decreases with decreasing momentum and so the low momentum events are emitted in almost random directions. A momentum cut must be chosen that maximizes the likelihood of the e^+ in the dataset carrying a large vertical momentum component.

The tracks generated in the simulation were reconstructed and fitted according the the same procedure that is applied to the real data; the following studies were performed using reconstructed information only (i.e. no MC truth information was used). The fitted tracks were extrapolated to the tangent point and their vertical angles analysed. Plots of the average vertical angle of the e^+ tracks as a function of time modulo the muon precession frequency are shown in figure 80. A range of symmetric momentum cuts were applied, where increasing number of e^+ at the extremes of the momentum range are removed. The amplitudes of the fits to these oscillations are plotted in figure

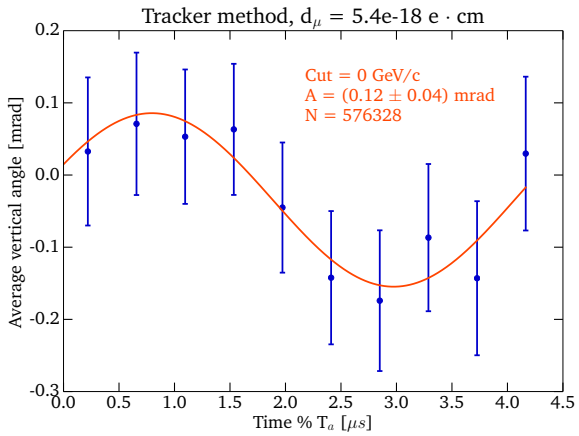

(a) No momentum cut

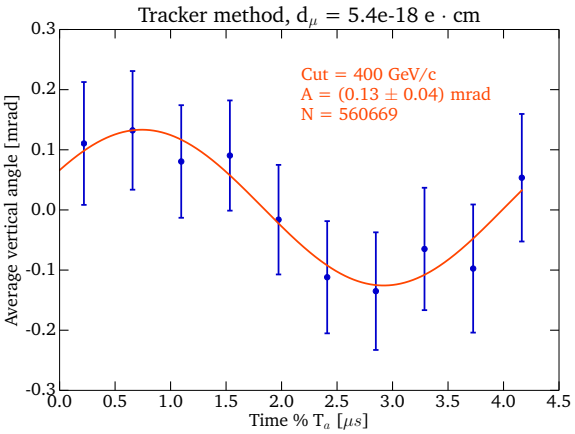

(b) 0.4 GeV/c < $|p_{e^+}|$ < 2.7 GeV/c

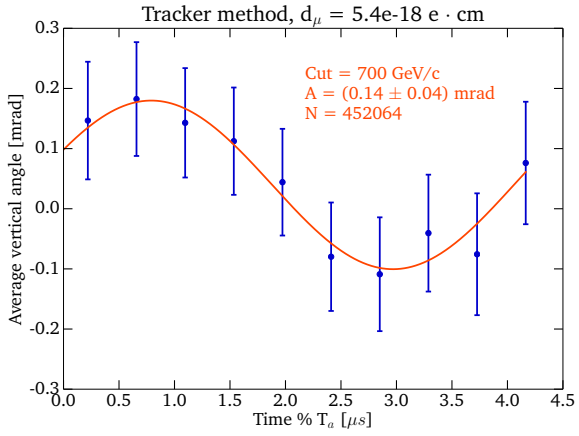

(c) 0.7 GeV/c < $|p_{e^+}|$ < 2.4 GeV/c

Figure 80: Plots of the average vertical angle as a function of time, modulo the $g-2$ period, as measured by the tracking detectors in an MC dataset with input $d_\mu = 30 \times d_\mu^{BNL}$. Different momentum cuts have been applied to the dataset in each plot.

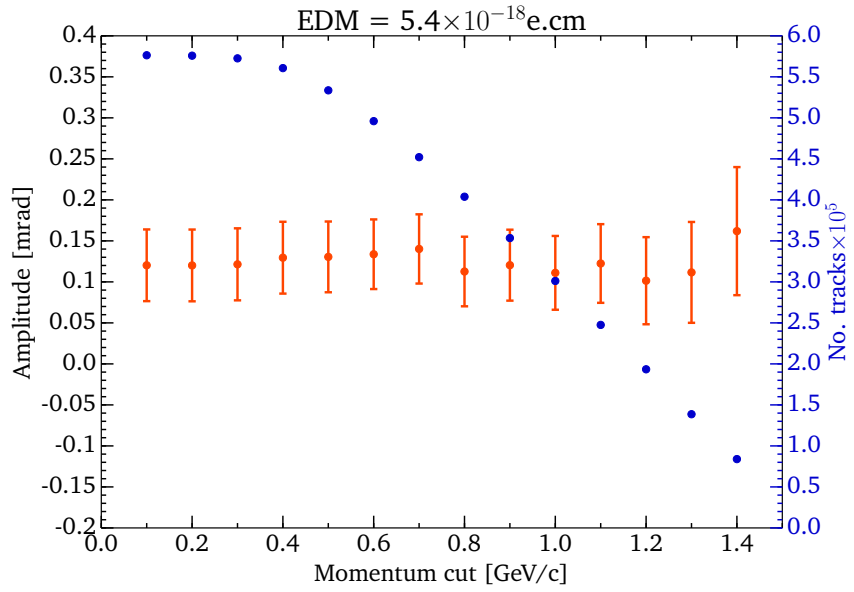

(a)

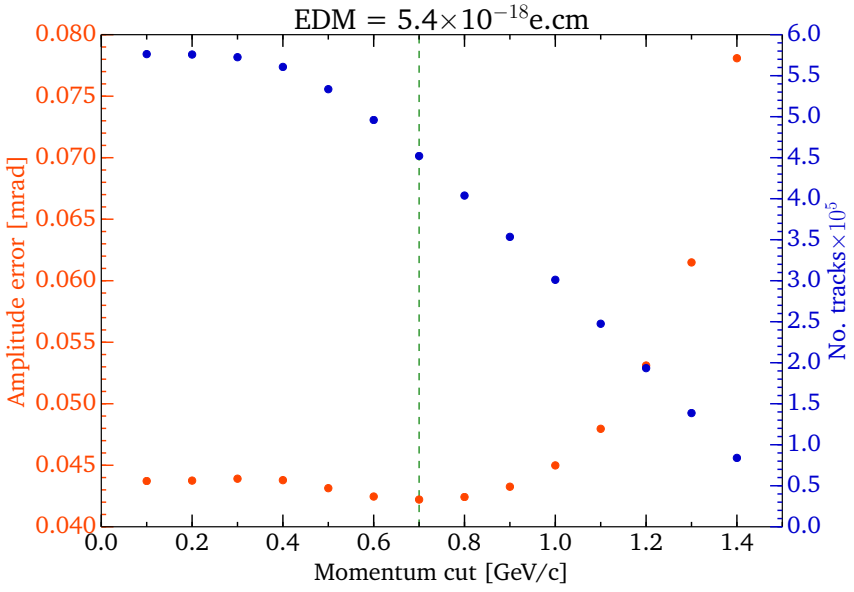

(b)

Figure 81: Plots summarising the measured amplitudes from fits to the plots shown in figure 80. Plot (a) shows the measured amplitude of the average vertical oscillation as a function of the size of symmetric momentum cut imposed on the data. Plot (b) shows the error on the measured amplitude as a function of the momentum cut. The number of tracks in each subset of the data is shown in blue.

81a, and the errors on the amplitudes are plotted in figure 81b. While there is little change in the measured amplitudes – and hence little change in δ – the accuracy of the amplitude obtained from the fit only starts to decrease significantly when only e^+ in the range $0.8 < p_{e+} < 2.3$ GeV/c are considered, where the comparatively low number of events starts to affect the fit quality. The fact that the accuracy of the fit is minimal for the cut $0.7 < p_{e+} < 2.4$ GeV/c, despite having lower events than some of the looser cuts, is consistent with the expectation that mid-range e^+ carry the EDM signal the most strongly, and suggests that this could be the optimal cut to impose. However, a larger dataset is required to conclude anything about the dependence of δ_{meas} on the momentum cut.

9.4 Summary

The muon EDM was added into the official $g-2$ simulation framework, `gm2ringsim`, by adding a time-dependent vertical component to the muon polarization vector. The amplitude of the oscillation in s_y in the MRF agreed with the analytical values for a range of different input EDM magnitudes. Simulated datasets with large EDM values were generated and the calorimeter method was used to see if the EDM simulation generated e^+ with the expected oscillation in their vertical decay angles. The expected increase in precession frequency was observed, as was the expected amplitude of oscillation in the asymmetry in the number of positrons arriving in the top and bottom halves of the calorimeters. The tracker-based method was studied using a dataset with an input value of $d_\mu = 30 \times d_\mu^{\mathrm{BNL}}$. The relationship between the measured amplitude in the oscillation of the average vertical angle of the decay e^+ and the momentum cut imposed on the dataset was studied for the first time, and a trend for the mid-range momentum e^+ carrying the signal most strongly is apparent. The study requires a higher-statistics dataset to be conclusive, and should also be performed using datasets with different EDM values to verify that the EDM signal is maximised for the same momentum range for any EDM value. This will be an important study, since if this were to vary with different EDM values, this would complicate the extraction of the measured EDM value from the observed oscillation amplitude.

The development of the EDM simulation was a crucial first step to understanding the sensitivity of the $g-2$ experiment to a muon EDM. Although much further study is required to understand the impact of systematic errors such as a radial B field or detector misalignment, the simulations presented in this chapter illustrate that the track extrapolation algorithm can be used

to reconstruct the vertical decay angle with sufficient accuracy to observe an oscillation with only moderate statistics for an input EDM of $d_\mu = 30 \times d_\mu^{\mathrm{BNL}}$.

Chapter 10

Outlook

At the time of writing this thesis, the $g-2$ experiment has just completed its first experimental run. The experiment officially began collecting physics-quality data in early February 2018, and a dataset approximately twice the size of the total BNL dataset has been recorded (before quality cuts). A plot of the fraction of BNL statistics recorded over time during the run is shown in figure 82.

The tracking detectors have been crucial to achieving this milestone; the ability to provide real-time feedback to the beam storage systems has enabled sub-optimal beam conditions to be quickly noticed and rectified. In addition to the online beam monitoring, the more in-depth offline analysis of the tracker data has been used to measure time-dependent properties of the stored beam such as the CBO amplitude. Comparison of the CBO amplitude between run conditions enabled the optimal running conditions to be determined for the physics-quality data-taking period. Furthermore, even during the stable running period there were several significant problems with the performance of the ESQ and kicker systems that resulted in a larger than expected CBO amplitude and average beam radial position. Precise knowledge of these parameters will be crucial to performing an accurate analysis of this dataset, since the conditions varied throughout the run. Such measurements are only possible with the tracking detectors.

Crucial to achieving the target dataset size of 21 times the Brookhaven dataset will be increasing the rate of detected decay e^+ per fill. During the 2018 run, the highest rate achieved was substantially short of the target positron rate. The reasons for this are suspected to be the same as the reason for the off-centre beam radius; the strength of the pulse delivered by the kicker magnets to move the injected e^+ onto the correct orbit radius has been measured to be significantly short of its design voltage. The Fermilab accelerator has a shutdown period during the summer of 2018 which will allow for several major improvements to be made to the kicker system that will rectify this, and should have a significant effect on increasing the number of stored μ^+ as well as correcting the radial distribution of the beam. Other upgrades to the experiment that will also help increase the storage fraction include upgrades to the ESQ system and the addition of insulation to the SR magnet to reduce temperature-dependent instabilities.

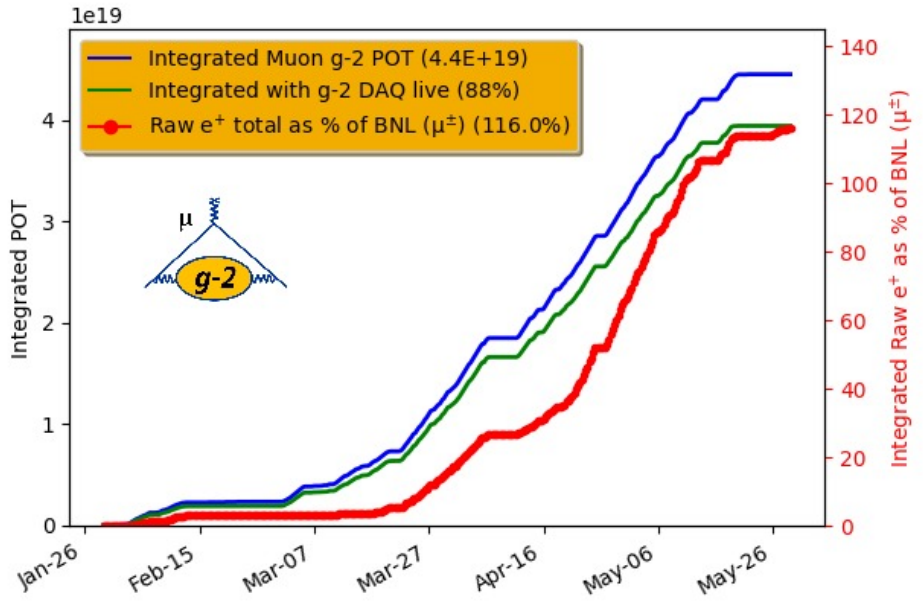

Figure 82: The number of e^+ recorded by the calorimeters as a percentage of the BNL total dataset, as of May 2018.

Chapter 9 of this thesis introduced the analysis techniques for the muon EDM search, and illustrated that only moderate statistics are required to observe a large EDM in the tracking detectors. The current number of tracks recorded is approximately 5×10^8, which is over 10 times the number of tracks recorded in the BNL traceback chambers. Chapter 9 illustrated that the tracker-based analysis technique is more sensitive to the muon EDM signal than the up-down asymmetry calorimeter-based method (although optimizations to the calorimeter method including the segmentation of the detectors have not been considered here). An EDM of $30 \times d_\mu^{\text{BNL}}$ can be seen in the detector with just 50,000 tracks, and as such a significant reduction in the current limit is confidently anticipated with the first dataset alone. This preliminary MC study needs to be further developed, however, to include effects such as tracker module misalignment and the radial magnetic field. Furthermore, given the long radial CBO lifetime and comparatively large CBO amplitude that have been observed in the running conditions so far, and the potential for the radial CBO to contribute a false EDM signal, this effect should also be studied. The ability to simulate a muon EDM accurately is hence a significant contribution to the experiment. The track extrapolation algorithm, developed as part of the work presented in this thesis, will be crucial to the experiment succeeding in placing a new limit on d_μ.

References

[1] Muon $g-2$ Collaboration, G. W. Bennett et al., *Final report of the E821 muon anomalous magnetic moment measurement at BNL*, Phys. Rev. D **73** (2006) 072003.

[2] Muon $g-2$ Collaboration, G. W. Bennett et al., *Improved limit on the muon electric dipole moment*, Phys. Rev. D **80** (2009) 052008.

[3] P. Kusch and H. M. Foley, *The Magnetic Moment of the Electron*, Phys. Rev. **74** (1948) 250–263.

[4] C. D. Anderson and S. H. Neddermeyer, *Cloud Chamber Observations of Cosmic Rays at 4300 Meters Elevation and Near Sea-Level*, Phys. Rev. **50** (1936) 263–271.

[5] S. H. Neddermeyer and C. D. Anderson, *Note on the Nature of Cosmic-Ray Particles*, Phys. Rev. **51** (1937) 884–886.

[6] D. Hanneke, S. Fogwell, and G. Gabrielse, *New Measurement of the Electron Magnetic Moment and the Fine Structure Constant*, Phys. Rev. Lett. **100** (2008) 120801.

[7] J. Schwinger, *A theory of the fundamental interactions*, Annals of Physics **2** no. 5, (1957) 407 – 434.

[8] T. D. Lee and C. N. Yang, *Question of Parity Conservation in Weak Interactions*, Phys. Rev. **104** (1956) 254–258.

[9] C. S. Wu, E. Ambler, R. W. Hayward, D. D. Hoppes, and R. P. Hudson, *Experimental Test of Parity Conservation in Beta Decay*, Phys. Rev. **105** (1957) 1413–1415.

[10] F. Combley, F. Farley, and E. Picasso, *The CERN muon ($g-2$) experiments*, Physics Reports **68** no. 2, (1981) 93 – 119.

[11] G. Charpak, P. J. M. Farley, E. L. Garwin, T. Muller, J. C. Sens, and A. Zichichi, *The anomalous magnetic moment of the muon*, Il Nuovo Cimento (1955-1965) **37** no. 4, (1965) 1241–1363.

[12] E. M. Purcell and N. F. Ramsey, *On the Possibility of Electric Dipole Moments for Elementary Particles and Nuclei*, Phys. Rev. **78** (1950) 807–807.

[13] Muon $g-2$ Collaboration, J. Grange et al., *Muon ($g-2$) Technical Design Report*, `arXiv:1501.06858 [physics.ins-det]`.

[14] F. Farley and Y. Semertzidis, *The 47 years of muon $g-2$*, Progress in Particle and Nuclear Physics **52** no. 1, (2004) 1 – 83.

[15] J. P. Miller, E. de Rafael, and B. L. Roberts, *Muon $g-2$: experiment and theory*, Reports on Progress in Physics **70** no. 5, (2007) 795.

[16] J. H. Christenson, J. W. Cronin, V. L. Fitch, and R. Turlay, *Evidence for the 2π Decay of the K_2^0 Meson*, Phys. Rev. Lett. **13** (1964) 138–140.

[17] J. Libby, *Direct CP violation in hadronic B decays*, `arXiv:1412.4269 [hep-ex]`.

[18] V. Barger, C. Kao, and A. Das, *The Muon Electric Dipole Moment*, `arXiv:9707544 [hep-ph]`.

[19] V. Barger, C. Kao, and A. Das, *The Electric Dipole Moment of the Muon in a Two Higgs Doublet Model*, `arXiv:9611344v2 [hep-ph]`.

[20] E. Iltan, *The effects of lepton KK modes on the electric dipole moments of the leptons in the Randall–Sundrum scenario*, The European Physical Journal C **54** no. 4, (2008) 583–590.

[21] A. Compton, *The magnetic electron*, Journal of the Franklin Institute **192** (1921) 145.

[22] S. G. G. Uhlenbeck, *Ersetzung der Hypothese vom unmechanischen Zwang durch eine Forderung bezüglich des inneren Verhaltens jedes einzelnen Elektrons*, Naturwissenschaften **13** (1925) 953.

[23] P. A. M. Dirac, *The quantum theory of the electron*, Proceedings of the Royal Society of London A: Mathematical, Physical and Engineering Sciences **117** no. 778, (1928) 610–624.

[24] W. Gerlach and O. Stern, *Der experimentelle Nachweis der Richtungsquantelung im Magnetfeld*, Zeitschrift für Physik **9** no. 1, (1922) 349–352.

[25] T. E. Phipps and J. B. Taylor, *The Magnetic Moment of the Hydrogen Atom*, Phys. Rev. **29** (1927) 309–320.

[26] R. Frisch and O. Stern, *Über die magnetische Ablenkung von Wasserstoffmolekülen und das magnetische Moment des Protons. I*, Zeitschrift für Physik **85** no. 1, (1933) 4–16.

[27] I. Estermann and O. Stern, *Über die magnetische Ablenkung von Wasserstoffmolekülen und das magnetische Moment des Protons. II*, Zeitschrift für Physik **85** no. 1, (1933) 17–24.

[28] I. Estermann and O. Stern, *Magnetic moment of the deuton*, Physical Review **45** no. 761, (1934).

[29] I. I. Rabi, J. M. B. Kellogg, and J. R. Zacharias, *The Magnetic Moment of the Proton*, Phys. Rev. **46** (1934) 157–163.

[30] J. E. Nafe, E. B. Nelson, and I. I. Rabi, *The Hyperfine Structure of Atomic Hydrogen and Deuterium*, Phys. Rev. **71** (1947) 914–915.

[31] D. E. Nagle, R. S. Julian, and J. R. Zacharias, *The Hyperfine Structure of Atomic Hydrogen and Deuterium*, Phys. Rev. **72** (1947) 971–971.

[32] P. Kusch and H. M. Foley, *Precision Measurement of the Ratio of the Atomic 'g Values' in the* $^2P_{\frac{3}{2}}$ *and* $^2P_{\frac{1}{2}}$ *States of Gallium*, Phys. Rev. **72** (1947) 1256–1257.

[33] J. Schwinger, *On Quantum-Electrodynamics and the Magnetic Moment of the Electron*, Phys. Rev. **73** (1948) 416–417.

[34] Y. Ueno et al., *New precise measurement of muonium hyperfine structure interval at J-PARC*, Hyperfine Interactions **238** no. 1, (2017) 14.

[35] T. Aoyama, M. Hayakawa, T. Kinoshita, and M. Nio, *Complete Tenth-Order QED Contribution to the Muon* $g-2$, Phys. Rev. Lett. **109** (2012) 111808.

[36] T. Aoyama, T. Kinoshita, and M. Nio, *Revised and improved value of the QED tenth-order electron anomalous magnetic moment*, Phys. Rev. D **97** (2018) 036001.

[37] P. Baikov, A. Maier, and P. Marquard, *The QED vacuum polarization function at four loops and the anomalous magnetic moment at five loops*, Nuclear Physics B **877** no. 3, (2013) 647 – 661.

[38] A. Kurz, T. Liu, P. Marquard, and M. Steinhauser, *Anomalous magnetic moment with heavy virtual leptons*, Nuclear Physics B **879** (2014) 1 – 18.

[39] A. Kurz, T. Liu, P. Marquard, A. V. Smirnov, V. A. Smirnov, and M. Steinhauser, *Light-by-light-type corrections to the muon anomalous magnetic moment at four-loop order*, Phys. Rev. D **92** (2015) 073019.

[40] A. Kurz, T. Liu, P. Marquard, A. V. Smirnov, V. A. Smirnov, and M. Steinhauser, *Electron contribution to the muon anomalous magnetic moment at four loops*, Phys. Rev. D **93** (2016) 053017.

[41] S. Laporta, *High-precision calculation of the 4-loop contribution to the electron $g-2$ in QED*, Physics Letters B **772** (2017) 232 – 238.

[42] S. Volkov, *New method of computing the contributions of graphs without lepton loops to the electron anomalous magnetic moment in QED*, Phys. Rev. D **96** (2017) 096018.

[43] C. Gnendiger, D. Stöckinger, and H. Stöckinger-Kim, *The electroweak contributions to $(g-2)_\mu$ after the Higgs-boson mass measurement*, Phys. Rev. D **88** (2013) 053005.

[44] A. Keshavarzi, D. Nomura, and T. Teubner, *The muon $g-2$ and $\alpha(M_Z^2)$: a new data-based analysis*, `arXiv:1802.02995 [hep-ph]`.

[45] A. Kurz, T. Liu, P. Marquard, and M. Steinhauser, *Hadronic contribution to the muon anomalous magnetic moment to next-to-next-to-leading order*, Physics Letters B **734** (2014) 144 – 147.

[46] KLOE Collaboration, D. Babusci et al., *Precision measurement of $e^+e^- \to \pi^+\pi^-\gamma/\sigma(e^+e^- \to \mu^+\mu^-\gamma)$ and determination of the $\pi^+\pi^-$ contribution to the muon anomaly with the KLOE detector*, Physics Letters B **720** no. 4, (2013) 336 – 343.

[47] BESIII Collaboration, M. Ablikim et al., *Measurement of the $e^+e^- \to \pi^+\pi^-$ cross section between 600 and 900 MeV using initial state radiation*, Physics Letters B **753** (2016) 629 – 638.

[48] M. Davier, A. Hoecker, B. Malaescu, and Z. Zhang, *Reevaluation of the hadronic vacuum polarisation contributions to the Standard Model predictions of the muon $g-2$ and $\alpha(m_Z^2)$ using newest hadronic cross-section data*, The European Physical Journal C **77** no. 12, (2017) 827.

[49] F. Jegerlehner, *Muon $g-2$ Theory: the Hadronic Part*, `arXiv:1705.00263v1 [hep-ph]`.

[50] RBC and UKQCD Collaborations, T. Blum et al., *Calculation of the Hadronic Vacuum Polarization Disconnected Contribution to the Muon Anomalous Magnetic Moment*, Phys. Rev. Lett. **116** (2016) 232002.

[51] G. Abbiendi, C. M. C. Calame, U. Marconi, C. Matteuzzi, G. Montagna, O. Nicrosini, M. Passera, F. Piccinini, R. Tenchini, L. Trentadue, and G. Venanzoni, *Measuring the leading hadronic contribution to the muon $g-2$ via μe scattering*, The European Physical Journal C **77** no. 3, (2017) 139.

[52] J. Prades, E. de Rafael, and A. Vainshtein, *The Hadronic Light-by-Light Scattering Contribution to the Muon and Electron Anomalous Magnetic Moments*, Lepton Dipole Moments (2011) 303–317.

[53] F. Jegerlehner, *Leading-order hadronic contribution to the electron and muon g - 2*, EPJ Web of Conferences **118** (2016) 01016.

[54] A. Nyffeler, *Precision of a data-driven estimate of hadronic light-by-light scattering in the muon $g-2$: Pseudoscalar-pole contribution*, Phys. Rev. D **94** (2016) 053006.

[55] M. Hoferichter, B.-L. Hoid, B. Kubis, S. Leupold, and S. P. Schneider, *Pion-pole contribution to hadronic light-by-light scattering in the anomalous magnetic moment of the muon*, `arXiv:1805.01471 [hep-ph]`.

[56] A. Czarnecki and W. J. Marciano, *Muon anomalous magnetic moment: A harbinger for "new physics"*, Phys. Rev. D **64** (2001) 013014.

[57] D. Stöckinger, *Muon $g-2$ and Physics Beyond the Standard Model*. WORLD SCIENTIFIC, 2011.

[58] M. Krawczyk, *The new $(g-2)$ for muon measurement and limits on the light Higgs bosons in 2HDM (II)*, `arXiv:0103223 [hep-ph]`.

[59] A. Cherchiglia, D. Stöckinger, and H. Stöckinger-Kim, *Muon $g-2$ in the 2HDM: maximum results and detailed phenomenology*, `arXiv:1711.11567 [hep-ph]`.

[60] M. Pospelov, *Secluded U(1) below the weak scale*, Phys. Rev. D **80** (2009) 095002.

[61] S. N. Gninenko, N. V. Krasnikov, and V. A. Matveev, *Muon $g-2$ and searches for a new leptophobic sub-GeV dark boson in a missing-energy experiment at CERN*, Phys. Rev. D **91** (2015) 095015.

[62] H. Davoudiasl, H.-S. Lee, and W. J. Marciano, *Muon $g-2$, rare kaon decays, and parity violation from dark bosons*, Phys. Rev. D **89** (2014) 095006.

[63] BaBar Collaboration, *Search for Invisible Decays of a Dark Photon Produced in e^+e^- Collisions at BaBar*, Phys. Rev. Lett. **119** (2017) 131804.

[64] R. L. Garwin, L. M. Lederman, and M. Weinrich, *Observations of the Failure of Conservation of Parity and Charge Conjugation in Meson Decays: the Magnetic Moment of the Free Muon*, Phys. Rev. **105** (1957) 1415–1417.

[65] P. J. Mohr, B. N. Taylor, and D. B. Newell, *CODATA recommended values of the fundamental physical constants: 2010*, Rev. Mod. Phys. **84** (2012) 1527–1605.

[66] W. Liu et al., *High Precision Measurements of the Ground State Hyperfine Structure Interval of Muonium and of the Muon Magnetic Moment*, Phys. Rev. Lett. **82** (1999) 711–714.

[67] M. Smith, *Developing the Precision Magnetic Field for the E989 Muon $g-2$ Experiment*. PhD thesis, University of Washington, 2017.

[68] D. Flay, *The muon $g-2$ experiment at Fermilab*, Proc. The 22nd International Spin Symposium (2016).

[69] W. Blum, W. Riegler, and L. Rolandi, *Particle detection with drift chambers*. Springer-Verlag Berlin Heidelberg, 2008.

[70] R. Veenhof, *Garfield - simulation of gaseous detectors*. `http://garfield.web.cern.ch/garfield/`.

[71] F. Sauli, *Principles of operation of multiwire proportional and drift chambers*, CERN (1977) .

[72] T. Stuttard, *The development, testing and characterisation of a straw tracking detector and readout system for the Fermilab muon $g-2$ experiment*. PhD thesis, University College London, 2018.

[73] M. Mapes, H. Hseuh, and W. Jiang, *Permeation of argon, carbon dioxide, helium, nitrogen and oxygen through Mylar windows*, Brookhaven National Lab (1993) .

[74] E. Electronik, *EE891 Series CO^2 Sensor Module for OEM / HVAC Applications*. `https://www.airtesttechnologies.com/support/datasheet/EE891.pdf`.

[75] D. Ambrose, J. Bono, and A. Mukherjee. Private communication.

[76] E. Nyström, *Über die numerische integration von differentialgleichungen*. HELSINGFORS, 1925.

[77] E. Lund, L. Bugge, I. Gavrilenko, and A. Strandlie, *Track parameter propagation through the application of a new adaptive Runge-Kutta-Nyström method in the ATLAS experiment*, Journal of Instrumentation **4** no. 04, (2009) P04001.

[78] L. Bugge and J. Myrheim, *Tracking and track fitting*, Nuclear Instruments and Methods **179** no. 2, (1981) 365 – 381.

[79] E. Lund, L. Bugge, I. Gavrilenko, and A. Strandlie, *Transport of covariance matrices in the inhomogeneous magnetic field of the ATLAS experiment by the application of a semi-analytical method*, Journal of Instrumentation **4** no. 04, (2009) P04016.

[80] C. Höppner, S. Neubert, B. Ketzer, and S. Paul, *A novel generic framework for track fitting in complex detector systems*, Nuclear Instruments and Methods in Physics Research Section A: Accelerators, Spectrometers, Detectors and Associated Equipment **620** no. 2, (2010) 518 – 525.

[81] R. McNabb, *An Improved Limit on the Electric Dipole Moment of the Muon*. PhD thesis, University of Minnesota, 2003.